Rochester Institute of Technology
RIT Digital Institutional Repository

Theses

8-2015

Controlling the Transient Interface Shape and Deposition Profile Left by Desiccation of Colloidal Droplets on Multiple Polymer Surfaces

Peter David Dunning

Follow this and additional works at: https://repository.rit.edu/theses

Recommended Citation
Dunning, Peter David, "Controlling the Transient Interface Shape and Deposition Profile Left by Desiccation of Colloidal Droplets on Multiple Polymer Surfaces" (2015). Thesis. Rochester Institute of Technology. Accessed from

This Thesis is brought to you for free and open access by the RIT Libraries. For more information, please contact repository@rit.edu.

Controlling the Transient Interface Shape and Deposition Profile Left by Desiccation of Colloidal Droplets on Multiple Polymer Surfaces

by

Peter David Dunning

A Thesis Submitted in Partial Fulfillment of the
Requirements for the Degree of Master of Science in
Mechanical Engineering

Supervised by

Dr. Michael Schertzer
Department of Mechanical Engineering
Kate Gleason College of Engineering
Rochester Institute of Technology
Rochester, New York
August 2015

Approved by:

_____

Dr. Michael Schertzer, Assistant Professor Date
Thesis Advisor, Department of Mechanical Engineering

_____

Dr. Michael Schrlau, Assistant Professor Date
Committee Member, Department of Mechanical Engineering

_____

Dr. Blanca Lapizco-Encinas, Associate Professor Date
Committee Member, Department of Biomedical Engineering

_____

Dr. Jiandi Wan, Assistant Professor Date
Committee Member, Microsystems Engineering

_____

Dr. Agamemnon Crassidis, Graduate Director/Associate Professor Date
Department Representative, Mechanical Engineering

Controlling the Transient Interface Shape and Deposition Profile Left by Desiccation of Colloidal Droplets on Multiple Polymer Surfaces

Peter David Dunning
Master of Science

Department of Mechanical Engineering
Kate Gleason College of Engineering
Rochester Institute of Technology
Rochester, New York
August 2015

ABSTRACT

A colloidal suspension is a small constituent of insoluble solid particles suspended in a liquid medium. Control over the wetting, evaporation, and deposition patterns left by colloidal suspensions is valuable in many biological, medical, industrial, and agricultural applications. Understanding the governing principles of wetting and evaporative phenomena of these colloidal suspensions may lead to greater control over resultant deposition patterns. Perhaps the most familiar pattern forms when an initially heterogeneous colloidal suspension leaves a dark ring pattern at the edge of a drop. This pattern is referred to as a coffee-stain and it can be seen from dried droplets of spilled coffee. This coffee-stain effect was first investigated by Deegan et. al. who discovered that these patterns occur when outward radial flows driven by evaporation at the triple contact line dominate over other effects.

While the presence of coffee-stain patterns is undesirable in many printing and medical diagnostic processes, it can also be advantageous in the production of low cost transparent conductive films, the deposition of metal vapor, and the manipulation of biological structures. Controlling the interactions between the substrate, liquid, vapor, and particles can lead to control over the size and morphology of evaporative deposition patterns left by aqueous colloidal

suspensions. Several methods have been developed to control the evaporation of colloidal suspensions to either suppress or enhance the coffee stain effect. Electrowetting on Dielectric (EWOD) is one promising method that has been used to control colloidal depositions by applying either an AC or DC electric field. EWOD actuation has the potential to dynamically control colloidal deposition left by desiccated droplets to either suppress or enhance the coffee stain effect. It may also allow for independent control of the fluidic interface and deposition of particles via electrowetting and electrokinetic forces. Implementation of this technique requires that the colloidal droplet be separated from the active electrode by a dielectric layer to prevent electrolysis. A variety of polymer layers have been used in EWOD devices for a variety of applications. In applications that involve desiccation of colloidal suspensions, the material for this layer should be chosen carefully as it can play an important role in the resulting deposition pattern.

An experimental method to monitor the transient evolution of the shape of an evaporating colloidal droplet and optically quantify the resultant deposition pattern is presented. Unactuated colloidal suspensions will be desiccated on a variety of substrates commonly used in EWOD applications. Transient image profiles and particle deposition patterns are examined for droplets containing fluorescent micro-particles. Qualitative and quantitative comparisons of these results will be used to compare multiple different cases in an effort to provide insight into the effects of polymer selection on the drying dynamics and resultant deposition patterns of desiccated colloidal materials.

It was found that the equilibrium and receding contact angles between the surface and the droplet play a key role in the evaporation dynamics and the resulting deposition patterns left by a desiccated colloidal suspension. The equilibrium contact angle controls the initial contact diameter for a droplet of a given volume. As a droplet on a surface evaporates, the evolution of the interface shape and the contact diameter can generally be described by three different regimes. The Constant Contact Radius (CCR) regime occurs when the contact line is pinned while the contact angle decreases. The Constant Contact Angle (CCA) regime occurs when the contact line recedes while the contact angle remains constant. The Mixed regime occurs when the contact radius and angle both reduce over time. The presence of the CCA regime allows the contact line to recede creating a more uniform deposition. However, not all droplets move into the CCA regime. Some remain in the CCR regime creating a coffee-stain pattern. In order to

transition into the CCA regime, the dynamic contact angle of the droplet must be reduced to an angle close to the receding contact angle.

Transient interface shapes and deposition patterns were examined on four surfaces: (i) Glass, (ii) Kapton HN polyimide tape, (iii) SU-8 3005, and (iv) Teflon AF. Glass has a low equilibrium contact angle and a very low receding contact angle resulting in a large uniform coffee-stain deposition. Kapton HN and SU-8 3005 have similar equilibrium contact angles that result in similar initial contact diameters. However, Kapton HN pins at that initial diameter due to a low receding contact angle producing a smaller more intense coffee-stain. SU-8 3005 has a large receding contact angle that allows for the transition into the CCA regime which results in a smaller, more uniform, and more intense spot. Teflon AF has the largest equilibrium and receding contact angle producing the smallest, most uniform, and most intense spot. Results presented here suggest that a lower receding contact angle is beneficial in areas where the coffee-stain effect needs to be enhanced while a larger receding contact angle is beneficial in areas where the coffee-stain needs to be suppressed.

Preliminary results are also presented examining droplets actuated via AC electrowetting to examine the effect of electrode geometry and applied voltage on electrowetting behavior and colloidal depositions in these cases. It was found that the Young-Lippmann equation needs to be modified to satisfy the modified capacitance per unit area of a system with different electrode geometries.

ACKNOWLEDGMENTS

I would like to thank my advisor, Dr. Michael Schertzer, for his guidance and support throughout my research. He contributed to a very rewarding graduate school experience by allowing flexibility in my research and supporting my travels to conferences and workshops. He has always demanded high quality work in all my endeavors and provided a comfortable work environment during my time here.

Additionally, I would like to thank my committee members: Dr. Michael Schrlau, Dr. Blanca Lapizco-Encinas, Dr. Jiandi Wan, and Dr. Agamemnon Crassidis for their interest, support, and insight into my work.

I would like to acknowledge the support of many facilities and labs throughout the Rochester Institute of Technology (RIT) that I have had the privilege of working with during my research. Every result presented in this thesis was accomplished with the support and help of professors, students, and collaborators throughout RIT.

The support of the Discrete MicroFluidics Laboratory (DMFL) under the direction of Dr. Michael Schertzer has been essential during my time here. My colleague in the lab and current graduate student, Mr. Collin Burkhart has been an incredible resource in the completion of this research. Additionally, the support of the Nano-Bio Interface Laboratory (NBIL) under the guidance of Dr. Michael Schrlau has been critical during my time here. The students under his tutelage, especially Masoud Golshadi, Yashar Seyed Vahedein, and Ayomipo Arowosola, have been such a caring and supportive group throughout this process.

The support of the Semiconductor & Microsystems Fabrication Laboratory (SMFL) under the guidance of Operations Manager Mr. Thomas Grimsley has been invaluable. I would like to thank Sean O'Brien, Patricia Meller, John Nash, and Bruce Tolleson for their crucial guidance in and out of the SMFL. This research would not have been possible without the support of the Director of the SMFL, Dr. Karl Hirschman, and his research group. He has been able to contribute knowledge, resources, time, and mentorship that have been monumental to completion of this work. Two of his graduate students, Wilkie Olin-Ammentorp and Nathaniel Walsh, passed down great amounts of knowledge and advice in the clean room during the time that I was with them.

The use of our initial Ramé-Hart Goniometer was provided by Dr. Scott Williams in the School of Chemistry and Materials Science. His advice and training resulted in subsequent purchasing of our own system. I would like to thank Dr. Hyla Sweet for the ability to work with the Confocal Microscopy Lab (CML) for all of the imaging provided in this work. Working with the Microscopy Assistants, Evan Darling and Abdul Karim Embong, has been a great learning experience. I would like to thank Dr. Kara Maki in the School of Mathematical Sciences for providing microparticles to test with and her continued support and collaboration with the DMFL. I have had the privilege to work in the Machine Shop in the Kate Gleason College of Engineering with such a great support group including David Hathaway, Robert Kraynik, and Jan Maneti.

I would like to thank all of my professors I have had over the years here at RIT who have had such a tremendous impact on my life, especially Dr. Surendra (Vinnie) Gupta, Dr. Mark Kempski, and Mr. Timothy Landschoot, for their guidance, mentorship, and resources provided throughout my thesis.

Throughout my time at RIT I have had the opportunity to work with amazing people in the Mechanical Engineering Department, especially Diane Selleck, Diedra Livingston, Venessa Mitchell, Jill Ehmann and William Finch.

Last but not the least important, I would like to thank my family, friends, and loved ones who have supported me during my time here. My family has always pushed me to achieve anything I ever hoped for and I could never repay them for their dedication, love, and support they have provided for me throughout my life.

TABLE OF CONTENTS

LIST OF FIGURES

LIST OF TABLES

LIST OF APPENDICES

NOMENCLATURE

Symbol	*Meaning*
T	Temperature
P	Pressure
V	Volume
A	Surface area
n	Composition
G	Gibbs free energy
γ	$= \left[\frac{\delta G}{\delta A}\right]_{T,P,n}$, Surface tension (i.e. Interfacial tension)
θ	Contact angle
θ_{eq}	Equilibrium contact angle between the solid-liquid and liquid-vapor interface
$cos\theta_{eq}$	$= \frac{\gamma_{SL}-\gamma_{SV}}{\gamma_{LV}}$, Young's equation
E	Surface energy (i.e. interface energy) per unit area
S_{eq}	$= [E_{substrate}]_{dry} - [E_{substrate}]_{wet}$, Equilibrium spreading parameter
S_{eq}	$= \gamma_{SV} - (\gamma_{SL} + \gamma_{LV})$, Equilibrium spreading parameter
θ_a	Advancing contact angle
θ_r	Receding contact angle
H	$= \theta_a - \theta_r$, Hysteresis
g	Gravity
ρ	Density
L	Characteristic length
Bo	$= \frac{\Delta\rho g L^2}{\gamma}$, Bond number (i.e. Eövötos number Eo)
c	Vapor concentration
R	Radial distance from the center of the droplet
D	Diffusion coefficient
m	Mass
t	Time
$-\frac{dm}{dt}$	$= -4\pi R^2 D \frac{dc}{dR}$, Rate of evaporative mass loss of a spherical droplet
c_S	Vapor concentration at the sphere surface
c_∞	Vapor concentration infinite distance away

R_S	Radial distance from the center of the drop to the surface
$-\frac{dm}{dt}$	$= 4\pi R_s D(c_s - c_\infty)$, Rate of evaporation of a spherical droplet
$-\rho\left(\frac{dV}{dt}\right)$	$= 4\pi R_S D c_S$, Rate of evaporation of a spherical droplet when $c_\infty = 0$
$f(\theta)$	Evaporative factor for a droplet on a surface
$-\left(\frac{dV}{dt}\right)$	$= \frac{4\pi R_S D}{\rho}(c_S - c_\infty) f(\theta)$, Volume decrease rate for a spherical drop on a surface
β	$= (1 - cos\theta)^2(2 + cos\theta)$, Radial distance factor for spherical cap
R_s	$= \left(\frac{3V}{\pi\beta}\right)^{1/3}$, Radius of spherical cap
r_b	$= R_s sin\theta$, Contact radius of spherical cap
h_{sph}	$= R_s(1 - cos\theta) = r_b \tan\left(\frac{\theta}{2}\right)$, Droplet height of a spherical cap
h	Height of liquid-vapor interface
r	Radial distance
J	Evaporative flux
$v(r,t)$	$= -\frac{1}{\rho r h}\int_0^r dr\, r\left(J(r,t)\sqrt{1 + \left(\frac{\delta h}{\delta r}\right)^2} + \rho\frac{\delta h}{\delta t}\right)$, Vertically averaged radial flow
U	Applied voltage
θ_0	Apparent contact angle of the system at zero applied voltage
θ_U	Voltage-dependent contact angle in the system
ε_r	Dielectric constant of the insulator
ε_0	Vacuum permitivity
d	Thickness of insulating layer
c	$\equiv \frac{\varepsilon_r \varepsilon_0}{d}$, Capacitance per unit area between the fluid droplet and the electrode
η	$\equiv \frac{cU^2}{2\gamma_{LV}} \equiv \frac{\varepsilon_r \varepsilon_0}{2d\gamma_{LV}} U^2$, Dimensionless electrowetting number
$cos\theta_U$	$= cos\theta_0 + \eta$, Young-Lippmann (Y – L) equation
A_d	Area of driving electrode
A_r	Area of reference electrode
A_t	Total area of electrode
$cos\theta_U$	$= \frac{\varepsilon_r \varepsilon_0}{2\gamma_{LV} d}\left(\frac{A_d}{A_t}\left(\frac{A_r}{A_d + A_r}\right)^2 + \frac{A_r}{A_t}\left(\frac{A_d}{A_d + A_r}\right)^2\right)U^2 + cos\theta_0$, Modified Y – L equation
y	Vertical distance of electric field
h	Droplet height
E	$= -\delta U/\delta y \approx U/h$, Approximate DC electric field
q	Charge on a particle

$F\downarrow$	$= qE$, Vertical force induced by a DC voltage induced electric field
μ	Liquid viscosity
a	Particle radius
v_{ep}	$\approx \frac{qU}{6\pi h\eta a}$, Electrophoretic velocity
$F\uparrow$	$= 6\pi\mu a v_{ep}$, Stokes-type viscous force
$1/k$	Debye length
ζ	$= \frac{q}{4\pi\varepsilon_r\varepsilon_0 a} - \frac{q}{4\pi\varepsilon_r\varepsilon_0\left(a+\frac{1}{k}\right)} = \frac{q}{4\pi\varepsilon_r\varepsilon_0 a(ka+1)}$, Zeta-potential of a spherical particle
q	$= 4\pi a\varepsilon_r\varepsilon_0\zeta$, Effective charge of a particle when ka is smaller than unity
v_{ep}	$= \frac{2}{3}\frac{\varepsilon_r\varepsilon_0}{\mu}\zeta\frac{U}{h}$, Electrophoretic velocity for particles on the order of nanometers
$\frac{\delta h}{\delta t}$	$\approx -K$, Approximate linear constant $K$of the droplet height decrease over time
J_0	Evaporative flux of a flat meniscus
$v_{adv}(r)$	$\approx \frac{r}{2h}\left(K - \frac{J_0}{\rho}\right)$, Advective velocity of a particle
t_{adv}	Advective timescale
t_{ep}	Electrophoretic timescale
d_{adv}	Advective distance
d_{ep}	Electrophoretic distance
$\bar{R}$	$= \frac{t_{adv}}{t_{ep}} \approx \frac{v_{ep}}{v_{adv}}\frac{d_{adv}}{d_{ep}} \approx \frac{\varepsilon_r\varepsilon_0}{\eta r\dot{h}}\zeta U$, Advective and electrophoretic timescale ratio
I	Intensity
I_B	Average background Intensity
$\bar{I}$	Average spot intensity
$I/\bar{I}$	Normalized intensity
D_I	Initial contact diameter
D_F	Final spot diameter of deposition
D_I/D_F	Diameter ratio
T_T	Total evaporation time
τ	$= t/T_T$, Normalized time
D	Measured diameter
θ	Measured contact angle
D/D_0	Normalized diameter
A_{e1}	Electrode area of a simple coplanar electrode configuration
A_{g1}	Ground wire area of a simple coplanar electrode configuration

A_D	Total droplet area
C_1	$= \frac{\varepsilon_r \varepsilon_0 A_{e1} A_{g1}}{d(A_{e1} A_{g1}) A_D}$, Capacitance per unit area of a simple coplanar electrode
$cos\theta_U$	$= \frac{C_1 U^2}{2\gamma_{LV}} + cos\theta_0$, Modified Y – L equation for a simple coplanar electrode
A_{e2+}	Electrode area when a droplet is centered between two electrodes
A_{g2+}	Ground wire area when a droplet is centered between two electrodes
A_{e2-}	Electrode area when a droplet is centered on an electrode
A_{g2-}	Ground wire area when a droplet is centered on an electrode
C_2	$= \frac{\left(\frac{\varepsilon_r \varepsilon_0 A_{e2+} A_{g2+}}{d(A_{e2+} A_{g2+}) A_D} + \frac{\varepsilon_r \varepsilon_0 A_{e2-} A_{g2-}}{d(A_{e2-} A_{g2-}) A_D}\right)}{2}$, Capacitance per unit area of a coplanar IDE
C_{2+}	Capacitance per unit area when a droplet is centered between two electrodes
C_{2-}	Capacitance per unit area when a droplet is centered on an electrode
C_2	$= \frac{C_{2+} + C_{2-}}{2}$, Capacitance per unit area of a coplanar IDE
$cos\theta_U$	$= \frac{C_2 U^2}{2\gamma_{LV}} + cos\theta_0$, Modified Y – L equation for a coplanar IDE

1.0 INTRODUCTION

1.1 Colloids

Colloids are defined as heterogeneous systems where a small constituent of one insoluble substance (dispersed phase) is dispersed throughout another medium (continuous phase). Colloids are ubiquitous in everyday life; such as the milk that we put in our coffee or tea, the marmalade we spread on our toast, and the shaving cream we use in the morning. Even our blood is classified as a colloidal suspension. The nineteenth century Scottish chemist, Thomas Graham (1805 – 1869), first introduced the word colloid while making fundamental discoveries using technology that was a rudimentary predecessor to modern-day dialysis machines [1].

The field of colloid science is vast including gels, emulsions, foams, sols, and aerosols (Fig. 1.1). Both the dispersed phase and continuous phase can be composed of solids, liquids, or gases. The scope of this thesis will be colloidal mixtures where solid particles (dispersed phase) are suspended in a liquid medium (continuous phase). The focus of this work will be to better understand the motion of the dispersed phase of the colloid as small droplets of fluid evaporate on a surface.

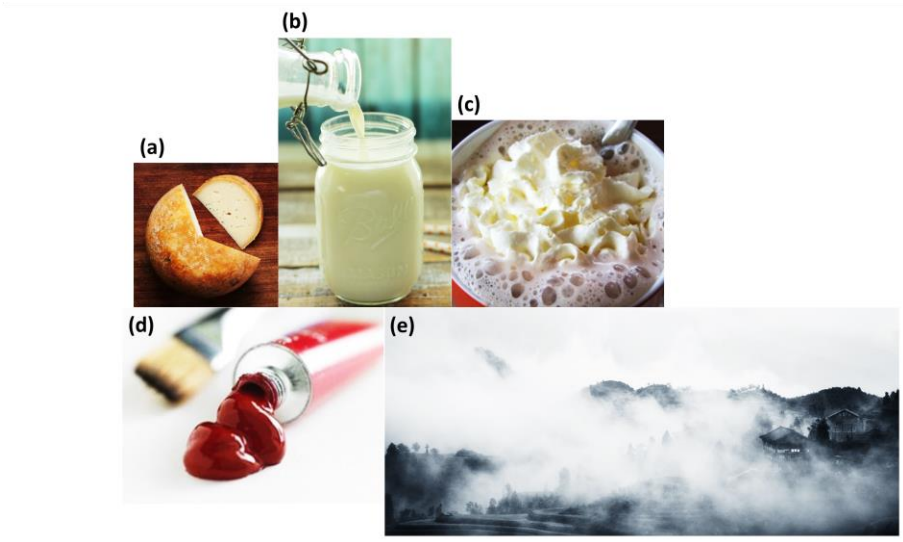

Figure 1.1: Various colloid examples including: (a) gel – cheese, (b) emulsion – milk, (c) foam – whipped cream, (d) sol - paint, and (e) aerosol – fog.

The interfacial surface area-to-volume ratio becomes important when looking at a colloidal system consisting of two or more phases. A colloidal particle has a large surface area-to-volume ratio compared to the bulk medium it is suspended in [2,3]. A cube shaped "particle" with characteristic length $1\ cm$ has a total surface area of $1\ cm^2$. If this cube is broken up into smaller cubes of characteristic length $1\ \mu m$ it would have a total surface area of $600\ m^2$. As the size of a particle is reduced, the surface area increases. This is accompanied by a large surface area-to-volume ratio when comparing two particles of the same mass. When surface area-to-volume ratios are large, forces that scale with surface area (e.g. diffusion) dominate over forces scaling with volume (e.g. gravity) [4]. The scope of this work will be on spherical colloidal particles with a micrometer characteristic length. Colloidal dispersions and particle behavior can be better understood by considering specific parameters of the particle: (i) size, (ii) shape, (iii) surface area, and (iv) surface charge [2,3]. Attractive and repulsive forces between particles must also be considered (e.g. Van der Waals, Electrostatic).

Even when a colloid is at equilibrium, the dispersed phase in the suspension exhibits random motion due to collisions with the continuous phase [5,6]. This motion is named Brownian Motion after the Scottish botanist Robert Brown (1773-1858) who observed the random motion of particles when studying grains of pollen of the plant Clarkia Puchella suspended in water under a microscope [7]. When a small droplet of fluid rests on a surface, the motion of the suspended material can then be influenced by interactions with a surface. This motion is further complicated as the droplet begins to evaporate and the motion in the dispersed phase is affected by evaporative and surface tension driven flows in the continuous phase.

A fundamental understanding of the motion of the dispersed phase in a colloidal suspension and the deposition pattern it leaves after the droplet dries is critical for a variety of practical applications [8] including: medical diagnostics [9–12], fabrication of flexible electronic devices [13], inkjet printing [14–16], and wastewater treatment [17] (Fig. 1.2).

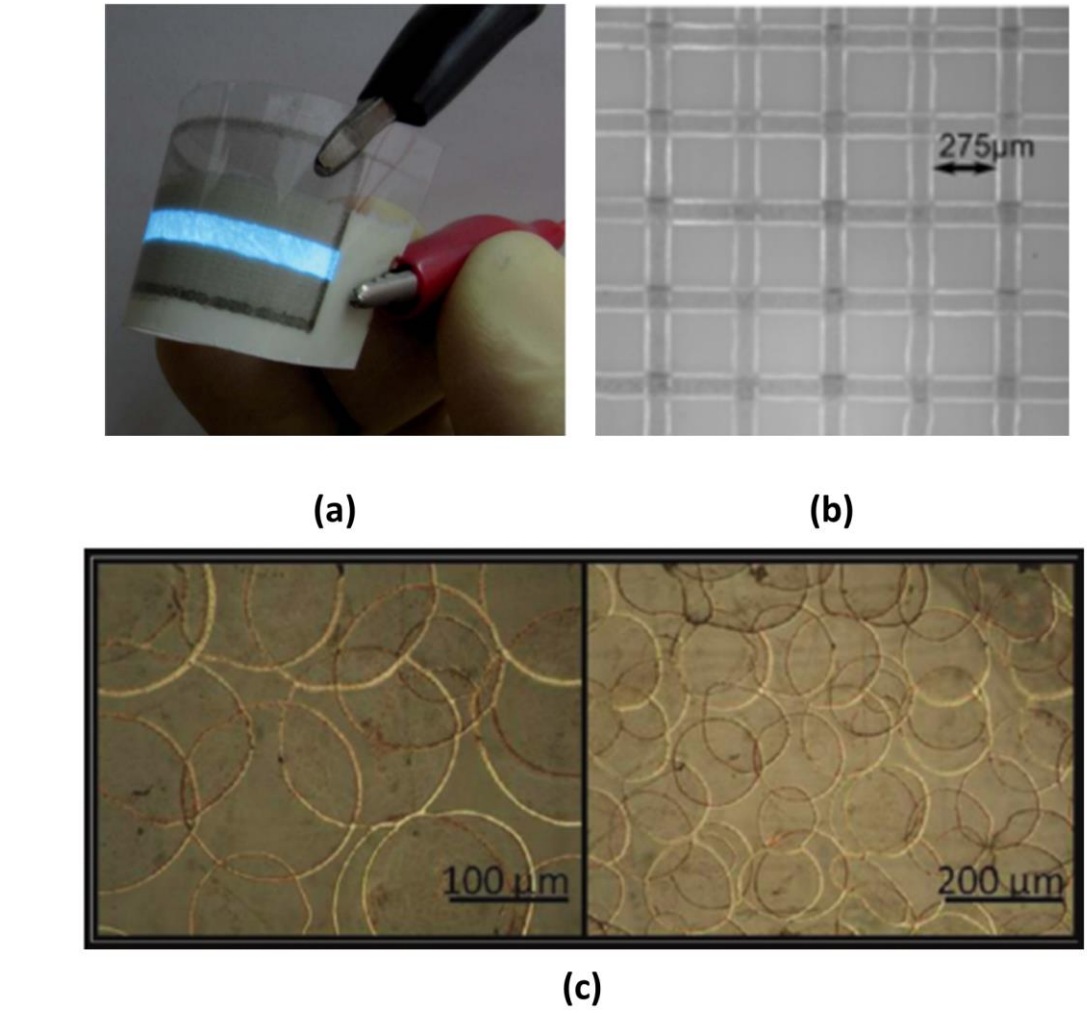

Figure 1.2: Various colloidal suspension and deposition pattern uses in practical applications including: (a) flexible electroluminescent device using carbon nanotubes [13], (b) rectilinear twin-line depositions of conductive silver nanoparticles [15], and (c) array of transparent conductive rings using silver nanoparticles [16].

1.2 Wetting Phenomenon

Wetting is understood as the relative ability of a liquid to maintain contact, i.e. wet, the surface of another solid or immiscible fluid. This wetting phenomenon is a common occurrence we can observe in nature and everyday life. Wetting behavior governs how rain drops roll off a leaf, how dew forms in the early morning, and how paint drips down the side of a freshly coated wall. An understanding of the behavior has led to advances in biological [9–12,18,19], and industrial applications [13–17,20–28].

When a small volume of fluid is placed on a surface, the area of contact is a function of at least the droplet volume, and the composition of the droplet, the surface, and the surrounding medium. If the droplet is not moving, it is referred to as a sessile droplet (Fig. 1.3). The wettability of a liquid on a surface and wettability studies generally involve measuring contact angle θ between the solid-liquid and liquid-vapor boundaries. When the contact angle is large, a surface is described as being hydrophobic, or water repellent. A droplet will bead up on a hydrophobic surface (Fig. 1.3a). When the contact angle is small a surface is described as being hydrophilic. A droplet will tend to spread out, or even form a film on a hydrophilic surface (Fig. 1.3b) [20].

The following section will describe the fundamental forces that govern wetting and wettability [20,29–36] and applicable research [21–25].

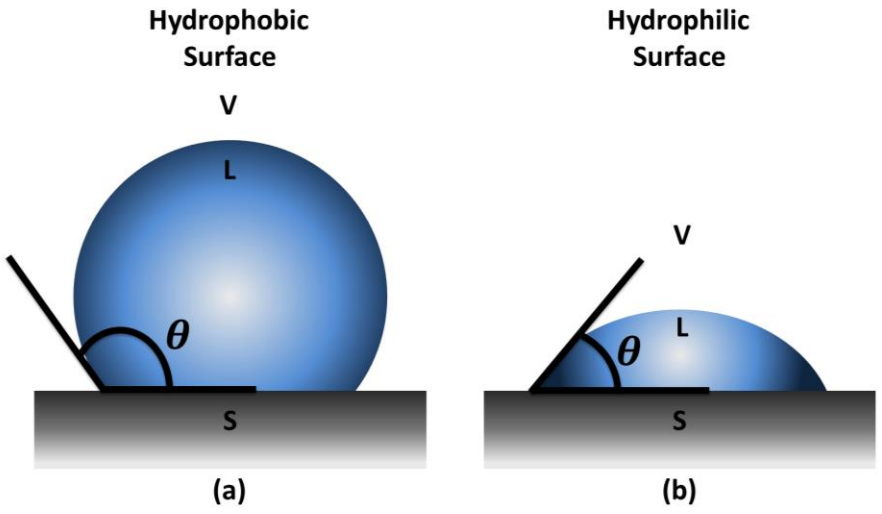

Figure 1.3: (a) Hydrophobic and (b) hydrophilic droplet of fluid placed on a surface with contact angle θ between solid-liquid and liquid-vapor boundary.

1.2.1 Surface Tension, Surface Thermodynamics, & Contact Angle

Surface tension (i.e. interfacial energy) is a contractile force that acts to minimize the surface area of any surface. Surface tension γ can be represented thermodynamically as the change in Gibbs free energy G per surface area A when temperature T, pressure P, and composition n are held constant (Eq. 1.1):

$$\gamma = \left[\frac{\delta G}{\delta A}\right]_{T,P,n} \tag{1.1}$$

At equilibrium, the interfaces between the solid, liquid, and vapor phases deform to minimize the interfacial energies. In a seminal work by Thomas Young [30], "An essay on the cohesion of fluids" the repeatability of the contact angle of a droplet on a surface was observed. Young described these observations as the interfacial tensions between phases. This work remains the foundation of modern wetting and capillary phenomena. The sessile droplet resting on a solid, smooth surface free from contamination in a vapor medium is assumed to be in thermodynamic equilibrium (mechanical, chemical, and thermal equilibrium) [29]. Under these assumptions, a sessile droplet at equilibrium state can be described by Young's equation, Equation 1.2 (Fig. 1.4):

$$cos\theta_{eq} = \frac{\gamma_{SL} - \gamma_{SV}}{\gamma_{LV}}, \tag{1.2}$$

where γ_{SL} , γ_{LV} , and γ_{SV} are the interfacial tensions at the solid-liquid, liquid-vapor, and solid-vapor interface, respectively, the equilibrium contact angle θ_{eq} is between the solid-liquid and the liquid-vapor interface at the Triple Contact Line (TCL). The TCL is the interface between the solid, liquid, and vapor phases of a droplet on a surface producing a contact angle dependent on the relative interfacial tensions of the system.

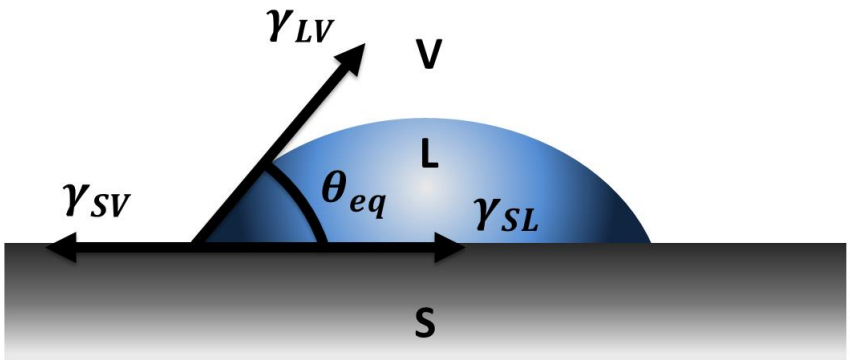

Figure 1.4: Illustration of liquid L resting a solid S in an ambient vapor V with an equilibrium contact angle θ_{eq} between the solid-liquid and liquid-vapor interface and interfacial tensions γ_{SV} , γ_{LV} , and γ_{SL} acting at the Triple Contact Line (TCL).

Young's theory was further developed by Dupre introducing the reversible work of adhesion using thermodynamics and the principle of minimum energy [31]. If the three interfacial tensions are known, the state of wetting may be understood by looking at the spreading parameter. The equilibrium spreading parameter S_{eq} is the measure of the difference between the surface energy (i.e. interface energy) per unit area E of a dry and wet substrate (Eq. 1.3 & Eq. 1.4) [29]:

$$S_{eq} = [E_{substrate}]_{dry} - [E_{substrate}]_{wet} \text{ , or} \tag{1.3}$$

$$S_{eq} = \gamma_{SV} - (\gamma_{SL} + \gamma_{LV}) \text{ .} \tag{1.4}$$

Wetting studies incorporating S_{eq} can help understand the interplay between surface energy of the system at the TCL, and the amount a liquid will spread on a surface. Complete wetting occurs when $S_{eq} = 0$, and partial wetting/non-wetting occurs when $S_{eq} \leq 0$ (Fig. 1.5). The dewetting phase is similar to the wetting phase, however there is a macroscopic vapor layer between the solid and liquid [8,29].

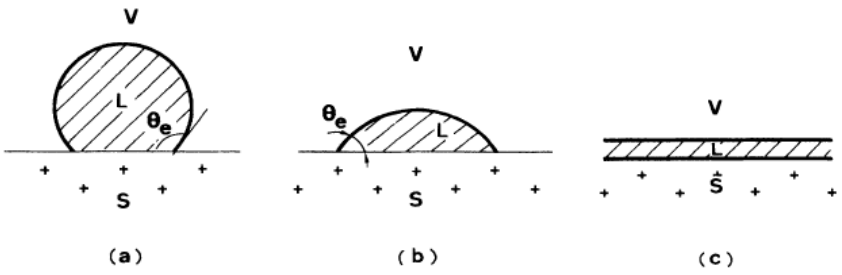

Figure 1.5: Illustration of liquid L wetting a surface S in an ambient vapor V with an equilibrium contact angle θ_{eq} where: (a) non-wetting, (b) partial wetting, and (c) complete wetting occurs [8].

Spreading and substrate wettability are often characterized by the equilibrium contact angle θ_{eq} [32]. For instance, non-wetting (low wettability, hydrophobic) is observed for $90° \leq \theta_{eq} < 180°$ (Fig. 1.5a). Partial wetting (high wettability, hydrophilic) is observed for $0° < \theta_{eq} < 90°$ (Fig. 1.5b). If $\theta_{eq} = 0$, then $\gamma_{SV} = \gamma_{SL} + \gamma_{LV}$ and this equilibrium would correspond to the complete wetting (i.e. spreading) of a liquid on a surface (Fig. 1.5c). The dewetting on a surface is less common and observed at $\theta_{eq} = 180°$ [8,20].

Observed values of equilibrium contact angle often vary from theoretical predictions due to surface defects from chemical and physical heterogeneities [8,29,33]. Dussan proposed the idea of differing microscopic and macroscopic contact angles at the TCL due to surface irregularities [33] (Fig. 1.6). Work by de Gennes brought together a number of concepts on static and dynamic wetting including a reversible change at the TCL, neglecting the long-ranged intermolecular forces acting at the TCL. Young's equation assumes that the sessile droplet is resting on a solid smooth surface free from contamination. However this assumption is generally not the case so θ_{eq} is better understood as the macroscopic equilibrium contact angle that we observe [8,21].

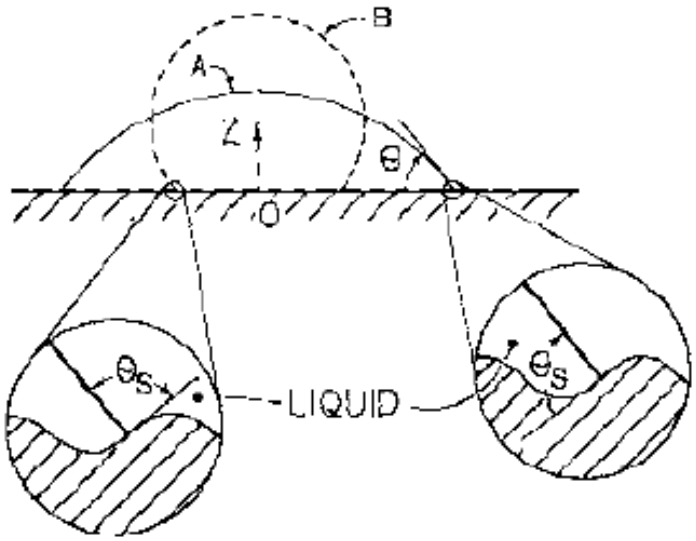

Figure 1.6: Two static sessile droplet configurations, A and B, on a solid surface with a sine wave deformation illustrating the actual (microscopic) contact angle θ_S may differ from the observed (macroscopic) contact angle θ [33].

1.2.2 Contact Angle Hysteresis

Understanding of surface wetting is not limited to the equilibrium case. As a sessile droplet dries, fluid volume, contact angle, and contact area can all change with time. This behavior is not completely characterized by the equilibrium contact angle [20]. When a sessile droplet on a substrate is not at equilibrium, the contact angle produced is called the dynamic contact angle. Characterizing dynamic contact angles provides insight into droplet behavior on specific substrate-ambient environments.

A sessile droplet initially placed on a substrate via a thin syringe needle (Fig. 1.7a) can be manipulated to produce dynamic contact angles. As the volume of the droplet is increased, the TCL is initially pinned while the contact angle increases (Fig. 1.7b). As the angle increases, there is an increase in the outward force at the contact line. Eventually the force is increased enough so the contact line moves forward (i.e. advances) on the substrate while the contact angle is constant (Fig. 1.7c). The contact angle made on the surface as the contact line advances is known as the

advancing contact angle θ_a and is greater than the equilibrium contact angle θ_{eq}. When the volume of the sessile droplet is decreased the TCL is initially pinned while the contact angle decreases (Fig. 1.7d). As the angle decreases there is an increase in the inward force at the contact line. Eventually the force is increased enough so the contact line moves backwards (i.e. recedes) on the substrate while the contact angle is constant (Fig. 1.7e). The contact angle made on the surface as the contact line recedes is known as the receding contact angle θ_r. Receding contact angles are less than the corresponding equilibrium contact angle θ_{eq} [34]. As the drop recedes it becomes so small that it is distorted by the capillary forces acting upon it at the tip of the needle (Fig. 1.7f). The difference between θ_a and θ_r is called the hysteresis H (Eq. 1.5):

$$H = \theta_a - \theta_r \, . \tag{1.5}$$

Contact angle hysteresis is generally attributed to surface roughness and/or heterogeneities [20]. In Young's equation (Eq. 1.2), three interfacial tensions γ_{SL} , γ_{LV} , and γ_{SV} at the TCL result in the equilibrium contact angle θ_{eq} based on an ideal, homogeneous surface. Young's equation can be misleading because it does not account for surface topography. The measured static contact angle is generally not equal to θ_{eq} [8,29,33,35]. Wenzel's equation and Cassie-Baxter's relation angles provides a prediction for the apparent contact angle of a droplet on a rough and heterogeneous surface, respectively [20]. The measured contact angle of a sessile droplet resting on a surface was found to be generally between the advancing contact angle $\theta_a$and the receding contact angle θ_r in [35].

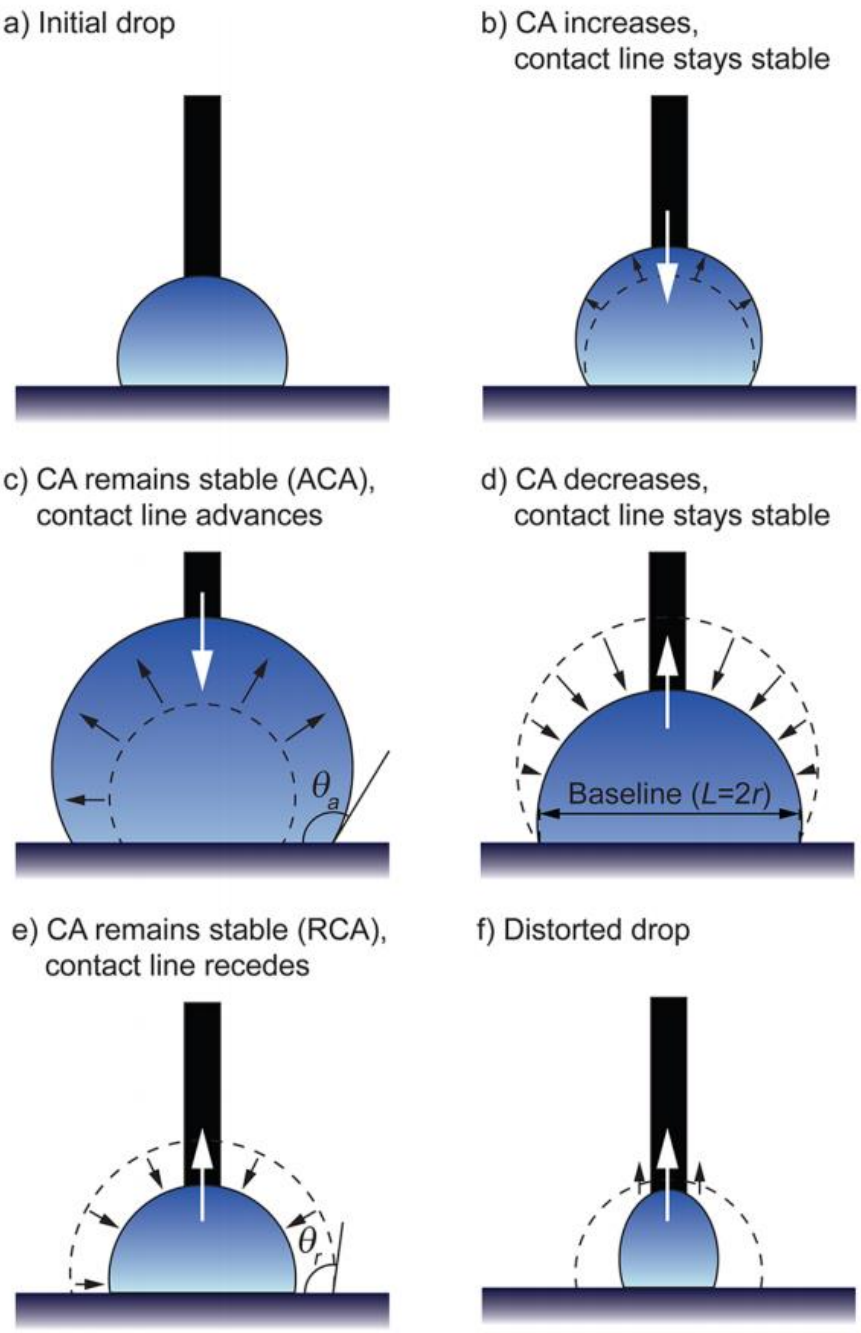

Figure 1.7: Illustration of an advancing contact angle θ_a and a receding contact angle θ_r where (a) an initial sessile droplet is placed on a surface, (b) the volume is increased while the contact line is pinned and θ increases, (c) the contact line advances while θ remains constant giving θ_a, (d) the volume is decreased while the contact line is pinned and θ decreases, (e) the contact line recedes while θ remains constant giving θ_r, and (f) the droplet becomes distorted [34].

Many techniques have been developed for preparation of homogeneous solid surface including vapor deposition, dip coating, surface polishing, solvent casting, heat pressing, and using self-assembled monolayers. However, an overall guideline on how to develop a smooth and homogeneous a surface that does not impact the equilibrium contact angle has not yet been developed [20].

Research encompassing wetting and interfacial phenomenon is a present question in the scientific community [9–36]. The creation of biomimetic artificial surfaces that are superhydrophobic and self-cleaning has been prominent in literature [23]. There has been development of superhydrophobic substrates based off of a lotus leaf structure with $\theta_{eq} > 150°$ [21] (Fig. 1.8a), and the development of polystyrene based microstructures fabricated based off of superhydrophobic rose petals [22] (Fig. 1.8b-c). Figure 1.8d presents a water droplet on a superhydrophobic adhesive fabricated microstructure based off of the rose petal. Advancements into the wetting behavior of different fluids on surfaces can advance many technologies that involve creating new materials that require anti-fogging and self-cleaning [24]. Additionally, Fabrication of superwetting nanowire membranes that could be practical in an oil spill cleanup [25].

The evaporation of colloidal droplets placed on substrates is important for many practical applications. Understanding this phenomena may provide a means to control evaporative forces and the deposition of the dispersed phase within the droplet [26].

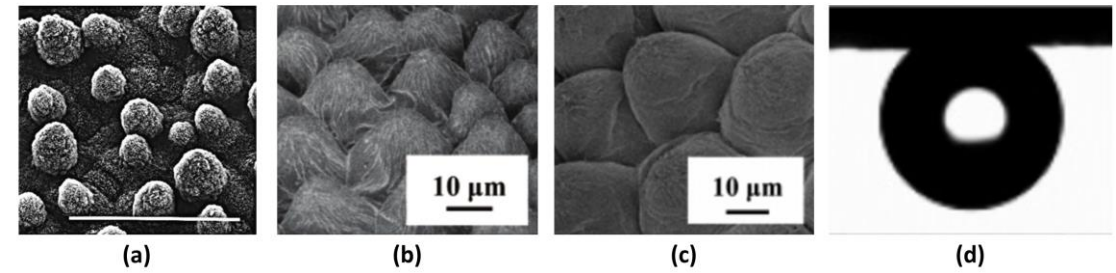

Figure 1.8: Examples of advancements in wetting behavior on different surfaces including SEM images of: (a) water-repellent leaf surfaces (Nelumbo nucifera) [21], (b) periodic array of micropapillae on the surface of a rose petal, (c) similar PS rose petal structure, and (d) superhydrophobic adhesive water drop on PS rose petal structure [22].

1.3 Evaporation of Sessile Droplets, Colloidal Suspensions, & Control over Resultant Deposition Patterns

A liquid drop deposited on a solid substrate limited by the TCL is known as a sessile droplet. The focus of this work is the examination of the evaporation of microliter sized sessile droplets. In these size ranges, surface tension forces generally dominate over gravitational forces due to a small characteristic length L. The Bond number Bo (or Eövötos number Eo) is the dimensionless parameter measuring the ratio of body forces (e.g. gravitational force) over surface tension forces (Eq. 1.6):

$$Bo = \frac{Body\ Forces}{Surface\ Tension\ Forces} = \frac{\Delta\rho g L^2}{\gamma}, \tag{1.6}$$

where $\Delta\rho$ is the difference between densities of two phases, g is the gravitational acceleration, L is the characteristic length of the system, and γ is the surface tension. The surface energy of the solid surface may be calculated by the contact angle of a sessile droplet on a substrate. Over time a sessile drop will evaporate, reducing the initial contact angle based on the atmospheric condition of the medium the sessile droplet is in. Sessile droplet evaporation plays a crucial role in many engineering applications including fuel injection into combustion engines [26], micro/nano fabrication [18,37], ink-jet printing [14–16,27], medical diagnostic processes [9,19], and the manufacturing of novel optoelectronic materials [28].

In many applications particles are dispersed in a liquid medium (i.e. colloidal suspension). When the contact line of the evaporating suspension is pinned the particles deposit at the TCL forming what is known as a "coffee stain". The presence of the coffee stain pattern is undesirable in many printing [14–16,27] and medical diagnostic processes [9,19]. Controlling the interactions between the liquid, particles, and substrate can lead to control over evaporative deposition patterns. Manipulation of the size and morphology of the stain is important in many applications as well. Suppression of the coffee stain effect has been achieved using several methods including addition of surfactants [38], enhancement of surface tension effects [39,40], surface modification [41], alteration of particle shape [42], and application of an electric field [43–45].

While coffee stains are undesirable in many applications, they have recently been used to produce low cost transparent conductive films by controlling colloidal deposition of carbon nanotubes

[13] and conductive inks [14–16]. Feature sizes were reduced by exploiting the coffee stain effect to create parallel lines from printed rivulets [14,15] and overlapping conductive rings from droplets [13,16]. Improving the uniformity of "coffee ring" stains may also be beneficial for controlled deposition of metal vapor [46] and biological structures [47].

The wide variety of applications for the enhancement or suppression of the coffee stain effect requires understanding how sessile droplets and colloidal suspensions evaporate, and the formation of resultant deposition patterns left on a variety of surfaces.

1.3.1 Evaporation of Sessile Droplets

The evaporation of a sessile droplet controlled by diffusion in still air can help us understand the more complicated evaporative process when air is moving and convection is present. When a volume of fluid with a small Bond number is used, surface tension dominate over gravity and the droplet rests on the solid surface in a semispherical shape with a constant radius (i.e. spherical cap). Using a sessile droplet model with a spherical cap assumption can lead to understanding more about the influence of geometry on the system. Additionally, evaporation of sessile droplets in industrial applications tend to have multiple liquid components. This multicomponent system results in preferential vaporization of the more volatile component. Only one liquid component is assumed for the equations presented here.

The basic case of a drop evaporating by diffusion was first derived by Maxwell in 1877. The mathematical model assumed the droplet was a spherical bulb and was floating in still air. The evaporative mass loss rate is given as [26] (Eq. 1.7):

$$-\frac{dm}{dt} = -4\pi R^2 D \frac{dc}{dR}, \tag{1.7}$$

where c is the vapor concentration, R is the radial distance from the center of the droplet, D is the diffusion coefficient of the vapor, m is the mass, and t is the time. Integrating Equation 1.7 based off boundary conditions where $c = c_\infty$ and $c = c_S$ at $R = R_\infty$ and $= R_S$, respectively gives the rate of evaporation (Eq. 1.8):

$$-\frac{dm}{dt} = 4\pi R_s D(c_s - c_\infty)\ , \tag{1.8}$$

where c_s is the concentration of vapor at the sphere surface, $c_\infty = 0$ is the vapor concentration of the drop at an infinite distance from the drop, R_s is the radius from the center to the surface of the spherical droplet.

Equation 1.8 can be rewritten as (Eq. 1.9):

$$-\rho\left(\frac{dV}{dt}\right) = 4\pi R_S D c_S\ , \tag{1.9}$$

where ρ and V are the density and volume of the liquid, respectively.

Maxwell's work assumes a spherical bulb of fluid suspended in a still medium and does not incorporate the presence of a substrate underneath the droplet. Introduction of a substrate prevents vapor from diffusing in the downward direction. Picknett and Bexon added a factor $f(\theta)$ for the decrease in the rate of drop evaporation due to the surface a droplet is placed upon. The rate of volume decrease over time is given by (Eq. 1.10) [26]:

$$-\left(\frac{dV}{dt}\right) = \frac{4\pi R_S D}{\rho}(c_S - c_\infty)f(\theta)\ , \tag{1.10}$$

where $V$is the volume of a spherical cap. The shape of the spherical cap is characterized by the contact angle θ, the radius of the sphere R_S, the contact radius r_b, and the droplet height h_{sph} (Fig. 1.9) [26]. The radial position can be expressed as (Eq. 1.11 – 1.13):

$$R_s = \left(\frac{3V}{\pi\beta}\right)^{1/3} \text{ and} \tag{1.11}$$

$$r_b = R_s sin\theta\ , \text{ where} \tag{1.12}$$

$$\beta = (1 - cos\theta)^2(2 + cos\theta) = 2 - 3cos\theta + \cos^3\theta\ . \tag{1.13}$$

While the height of the spherical cap of fluid on a solid surface can be expressed as two equations based off of the radii and the contact angle (Eq. 1.14 – 1.15):

$$h_{sph} = R_s(1 - cos\theta) \text{ and} \tag{1.14}$$

$$h_{sph} = r_b \tan\left(\frac{\theta}{2}\right). \tag{1.15}$$

Several authors have advanced the numerical models of sessile droplet evaporation based on a wide array of diverse experimental situations. Complete derivations, and references to advanced droplet evaporation models and investigations may be found in [26]. Wetting dynamics and evaporation vary depending on the substrate, liquid, and medium that the system is in. Different evaporative regimes may be observed as a result.

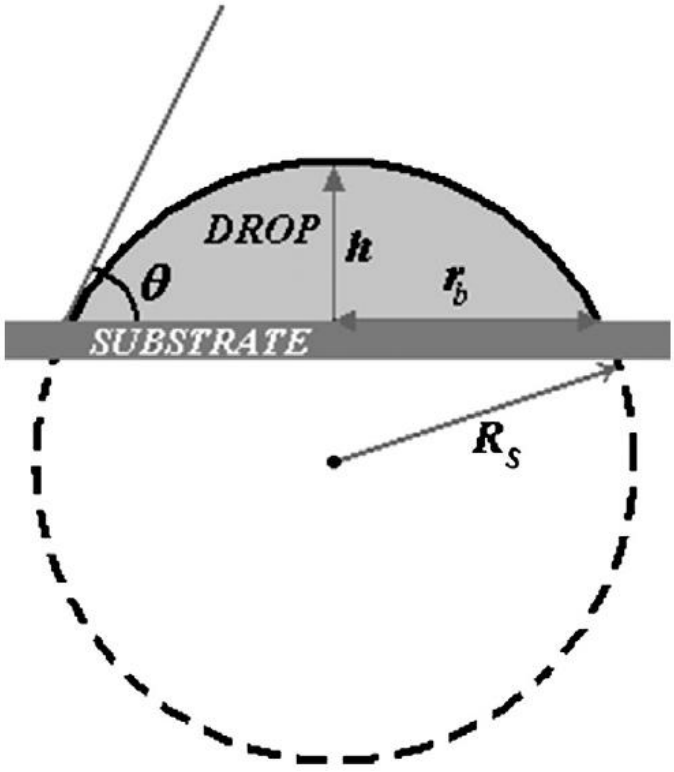

Figure 1.9: Illustration of a spherical cap droplet on a substrate characterized by the contact angle θ, the radius of the sphere R_S, the contact radius r_b, and the droplet height h [26].

1.3.2 Evaporative Regimes

When a droplet is resting on a surface in a surrounding medium it may experience different types of evaporative regimes. That may be based off of many variables involving the solid, liquid, and vapor phases of a colloidal suspension. The particle shape, size, and composition can affect how it interacts with the surface, and liquid medium. The volume and composition of the liquid medium are two of the factors that are attributed to how the liquid evaporates. However, how this liquid interacts with the solid surface, and vapor medium are critical to how the droplet beads up, or spreads on the surface directly affecting evaporation. The interplay between these phases is complex and leads to many different evaporative patterns.

The different evaporative regimes for a simple sessile droplet were first proposed by Picknett and Bexon [26] and are illustrated in Figure 1.10 [48]. When the TCL is pinned the contact angle decreases while the radius is held constant (i.e. CCR regime) (Fig. 1.10a). When the TCL slips, the contact angle is constant while the radius decreases (i.e. CCA regime) (Fig. 1.10b). A mixed mode exists where the radius or contact angle would both change over time (Fig. 1.10c). Understanding the influence of the substrate on the liquid may help predict these regimes. Influencing the timing of these regimes can change where particles deposit when an aqueous colloidal suspension evaporates.

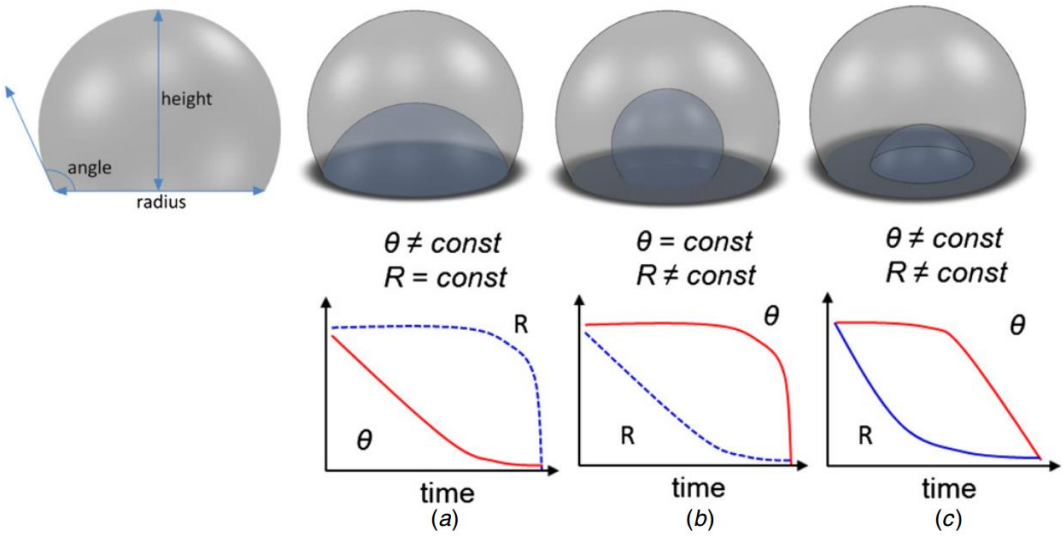

Figure 1.10: Evaporative regimes as proposed by Picknett and Bexon where there is a (a) Constant Contact Radius (CCR), (b) Constant Contact Angle (CCA), or (c) mixed mode [48].

1.3.3 Evaporation of Aqueous Colloidal Suspensions & Coffee Stain Formations

Colloidal materials are microscopic, insoluble particles evenly dispersed throughout a solution. A colloidal particle has a large surface area-to-volume ratio compared to the bulk medium it is suspended in [2,3]. As the size of a particle is reduced, the surface area-to-volume ratio increases. For a given volume fraction (or mass fraction) of particles, the surface area will increase as the particle size decreases. When surface area-to-volume ratios are large, forces that scale with surface area (e.g. diffusion) dominate over forces scaling with volume (e.g. gravity) [4].

As a colloidal suspension evaporates, neutrally buoyant particles will follow the flow of the droplet. However, when the particles become so small, attractive Van der Waals forces can result in aggregation and clustering of particles, so tuning the ionic strength may be necessary for certain applications [49].

As a droplet containing colloidal materials dries, different pattern formations may occur. Evaporation of particles dispersed in a liquid medium (i.e. colloidal suspension) is relevant in a variety of applications [9–37]. The addition of particles to the evaporation of a sessile droplet has a large impact on the dynamics that occur at the contact line and has been studied extensively in the past years. However, the interactions between the particles, fluid, and substrate are not fully understood.

When the majority of the particles are often deposited around the periphery of the droplet a phenomenon known as the “coffee stain” effect occurs [9,50–56]. The formation of this pattern is the result of contact line pinning and the interplay between evaporative and surface tension effects in the droplet (Fig. 1.11). When the contact line is pinned, the evaporative flux J in the droplet is highest at the outer edge. This creates a radially outward flow that deposits particles at the contact line. Evaporation at the contact line also creates a temperature T drop across the droplet. This temperature gradient gives rise to a surface tension gradient driven flow that can resuspend particles in the droplet (i.e. Marangoni Flow). When the evaporative flow dominates, particles are deposited at the contact line in a coffee stain pattern.

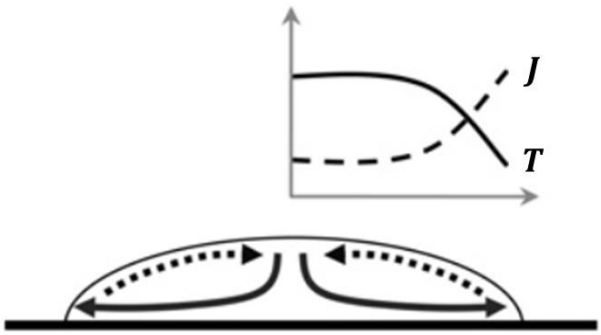

Figure 1.11: Side view schematic of drying sessile drop showing radially outward flow (solid arrow) and temperature T across the droplet (solid line) created by the evaporative flux J on the surface of the droplet (dashed line). Marangoni flow (dashed arrow) is driven by surface tension gradients due to the temperature gradient across the droplet [9].

Deegan et. al. first attributed coffee stain formation to capillary flows and evaporative flows [50–52] (Fig. 1.12a) where vapor leaves the droplet of radius R at a velocity $v(r,t)$ at contracting height $h(r,t)$ based on the evaporative flux $J(r,t)$. A mathematical model was developed to define the quantities responsible for the evaporation of an aqueous colloidal suspension [52]. Assuming an axisymmetric droplet, the vertically averaged radial flow of the fluid v of the droplet can be represented by (Eq. 1.16):

$$v(r,t) = -\frac{1}{\rho r h}\int_0^r dr\, r\left(J(r,t)\sqrt{1+\left(\frac{\delta h}{\delta r}\right)^2}+\rho\frac{\delta h}{\delta t}\right), \tag{1.16}$$

where t is time, ρ is the density of the liquid, r is the radial distance, h is the position of the liquid-vapor interface (i.e. height), and J is the rate of mass loss per unit surface area per unit time (i.e. evaporative flux). Additional derivation of the evaporative flux and height may be found in [52].

Many hydrophilic surfaces pin at the TCL resulting in a decrease in contact angle while the radius is held constant over time (i.e. CCR regime) (Fig. 1.10a). This pinning gives rise to the collection of particles along the periphery (Fig. 1.12b) resulting in a coffee stain formation. However, some hydrophobic surfaces have a TCL that slips during evaporation resulting in a decrease in the radius while the contact angle is held constant (i.e. CCA regime) (Fig. 1.12b). This slipping of the contact radius leads to the sweeping in of particles resulting in distribution patterns similar to Figure 1.12c.

Control over evaporative and surface tension effects leads to the control of the deposited solute which has advantages in many applications including medical diagnostics [9–12], fabrication of flexible electronic devices [13], inkjet printing [14–16], and wastewater treatment [17].

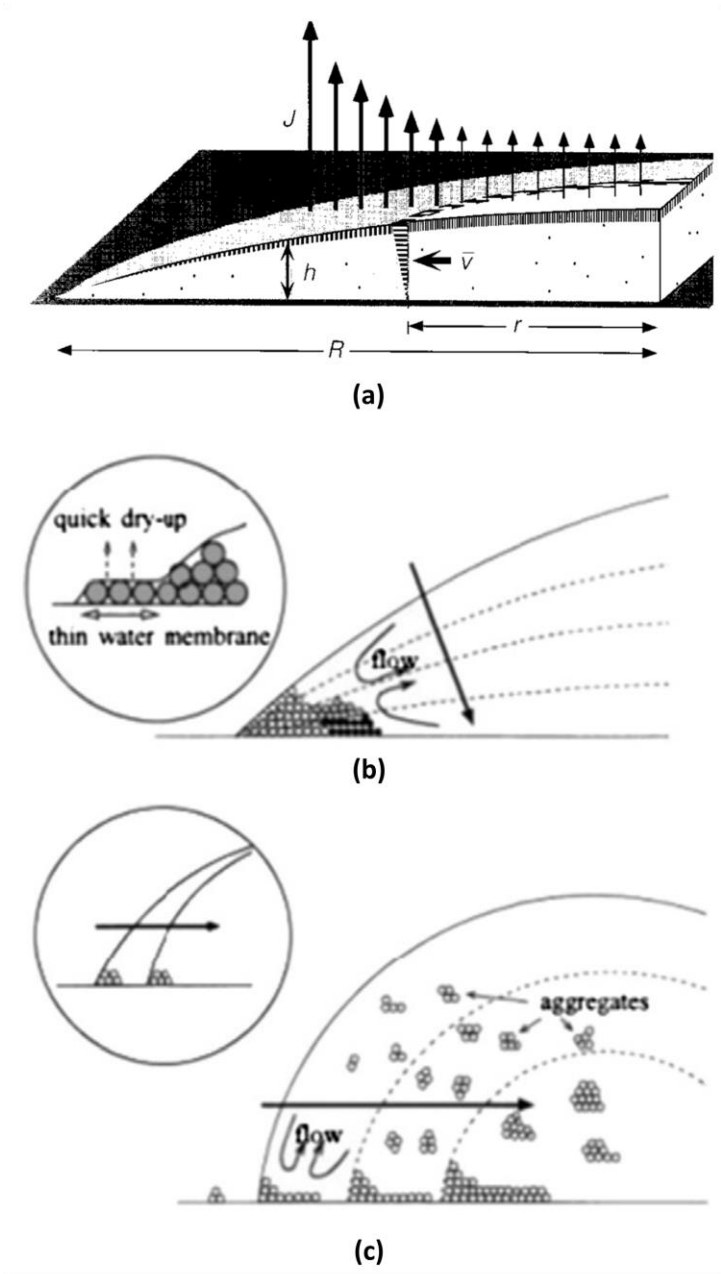

Figure 1.12: Outward flow of colloidal droplet during evaporation illustrating (a) the quantities responsible for evaporation where vapor leaves the droplet of radius R at a velocity $v(r,t)$ at contracting height $h(r,t)$ based on the evaporative flux $J(r,t)$ [50], and a schematic representation of the evaporation of a colloidal droplet on a (b) hydrophilic, and (c) hydrophobic surface [53].

1.5 Methods of Suppressing and Enhancing Coffee Ring Formation

In many applications particles are dispersed in a liquid medium (i.e. colloidal suspension). When the contact line of the evaporating suspension is pinned, the particles deposit at the TCL forming what is known as the coffee stain. The presence of the coffee stain pattern is undesirable in many printing [27] and medical diagnostic processes [9,19]. Controlling the interactions between the liquid, particles, and substrate can lead to control over evaporative deposition patterns. Manipulation of the size and morphology of the stain is important in many applications. Suppression of the coffee stain effect has been achieved using several methods including addition of surfactants [38], enhancement of surface tension flow via temperature gradients [39,40], surface modification [41], alteration of particle shape [42], and application of an electric field [43–45].

In [38], modification of the droplet composition resulted in the manipulation of both the size and morphology of the deposition pattern. Increasing the amount of surfactant added to the droplet resulted in a decreased initial surface tension σ_0, and three distinct drying regimes were produced (Fig. 1.13). The resultant deposition patterns observed were attributed to the change in contact line dynamics during evaporation. Theoretical and empirical results both suggested that the addition of surfactants led to a dense layer of micellar-protrusions on the colloid and substrate surface that acted as a barrier to pinning.

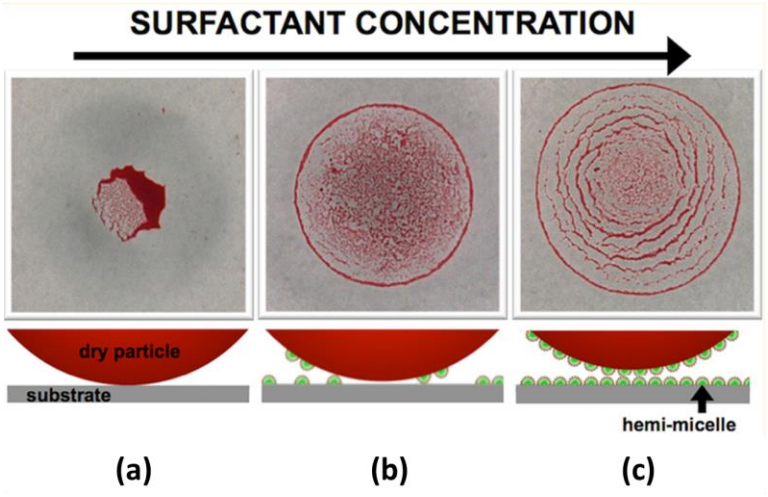

Figure 1.13: Top view images of resultant deposition patterns of colloids (top) and side view (bottom) schematic images of droplets on a substrate with different surfactant concentrations and initial surface tension σ_0 of (a) 72, (b) 48, and (c) 39 mN m^{-1} [38].

Influencing the flow fields within the droplet may lead to control over droplet deposition morphology and size. The surface tension driven flow induced by temperature gradients (i.e. Marangoni flow) can be reversed by controlling the temperature profile across a droplet, and can thus control the deposition of an aqueous colloidal suspension [39] (Fig. 1.14).

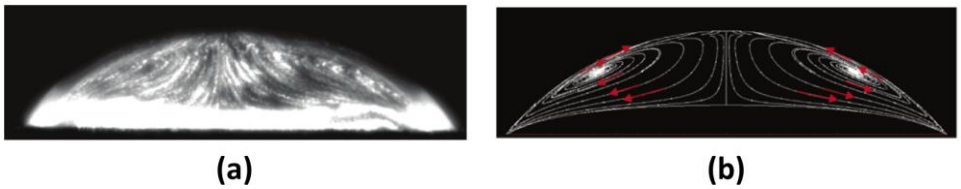

Figure 1.14: Evaporation of an octance droplet with Marangoni flows due to control of temperature profiles, (a) experimental image, and (b) predicted [39].

Modification of the surface that a sessile droplet rests on influences the interactions between particles, liquid, and substrate. A hydrophobic silicon pillar array was used as the substrate during single-drop evaporation of a colloidal suspension of latex spheres [41] (Fig. 1.15). The coffee ring was suppressed by forming a porous gel foot at the contact line due to the Wenzel wetting state induced by the silicon pillar array resulting in an inward mass transport depositing particles in the center of the spot.

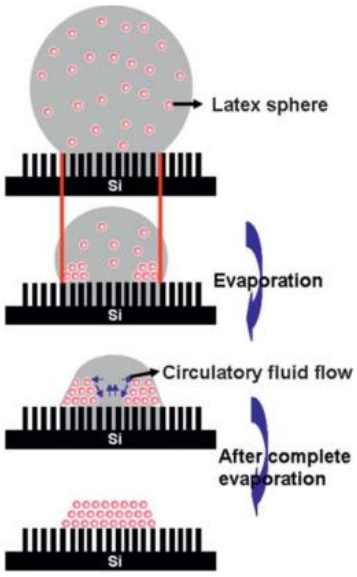

Figure 1.15: Side view schematic of Wenzel evaporative state due to silicon pillar array where the drop diameter remains constant, the contact angle decreases, and a circulatory field distributes the particles to the center of the droplet [41].

In [42], suppression of the coffee stain was influenced by the modification of particle shapes within the aqueous colloidal suspension. Both ellipsoidal (Fig. 1.16a) and spherical (Fig. 1.16b) particles were used with major-minor axis aspect ratios $\propto$ equal to 3.5 and 1.0, respectively. The aqueous colloidal suspension containing spherical particles pinned at the TCL and produced a coffee ring deposition pattern. However, the suspension with ellipsoidal particles produced a uniform deposition. The ellipsoidal particles significantly deformed the pinned contact line and produced a strong interparticle capillary interaction that led to this distribution pattern (Fig. 1.16).

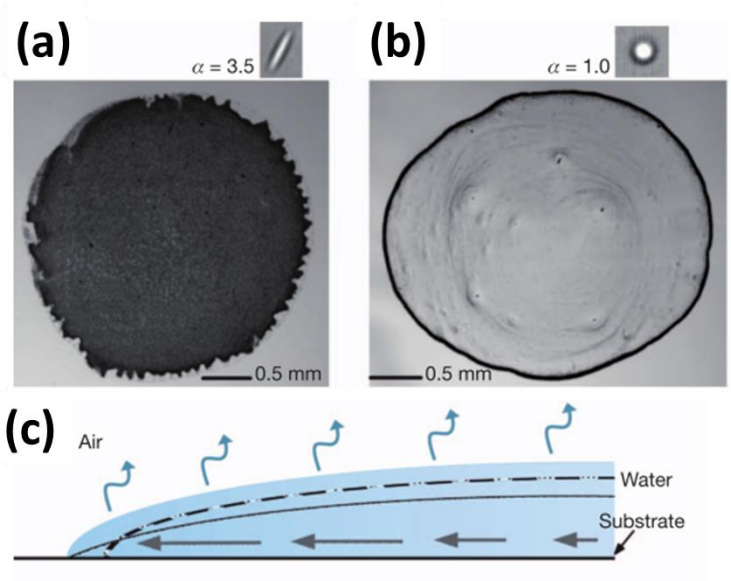

Figure 1.16: (a – b) Top view images of final deposition pattern of an aqueous colloidal suspension with (a) ellipsoids ($\alpha = 3.5$) and (b) spheres ($\alpha = 1.0$). (c) Diagram of the evaporative flux on the droplet (blue arrows), the shape of the droplet if allowed to recede (dashed line), the capillary flow (black arrow) due to a pinned contact line and reduced contact angle [42].

The use of surfactants [38], temperature gradients [39,40], surface modification [41], particle shape modification [42] all have unique ways of modifying the size and morphology of an aqueous colloidal deposition pattern. However, this work focuses on characterizing the deposition profile of colloids and the manipulation of profiles with the application of electric fields; Electrowetting (EW).

1.5.1 Electrowetting

Electrowetting on dielectric (EWOD) devices are microfluidic devices that manipulate fluid interfaces by applying electric fields (Fig. 1.17) [43–45,50–52,54,57–66]. EWOD devices consist of a flat conductive electrode patterned onto a substrate generally using photolithographic techniques. The electrode is covered with electrically insulating dielectric and hydrophobic layers. The droplet placed on the EWOD device beads up on the hydrophobic surface. When a voltage is applied, the electrowetting effect will cause the droplet to spread.

Application of the field results in an electrowetting force on the interface that decreases the apparent contact angle from θ_0 to θ_U. In order for this manipulation to take place, a ground electrode must be present in the system. Typical configurations for sessile droplets include direct insertion of a ground wire into the fluid (Fig. 1.17a) or the addition of a ground electrode in the same plane as the actuation electrode (Fig. 1.17b).

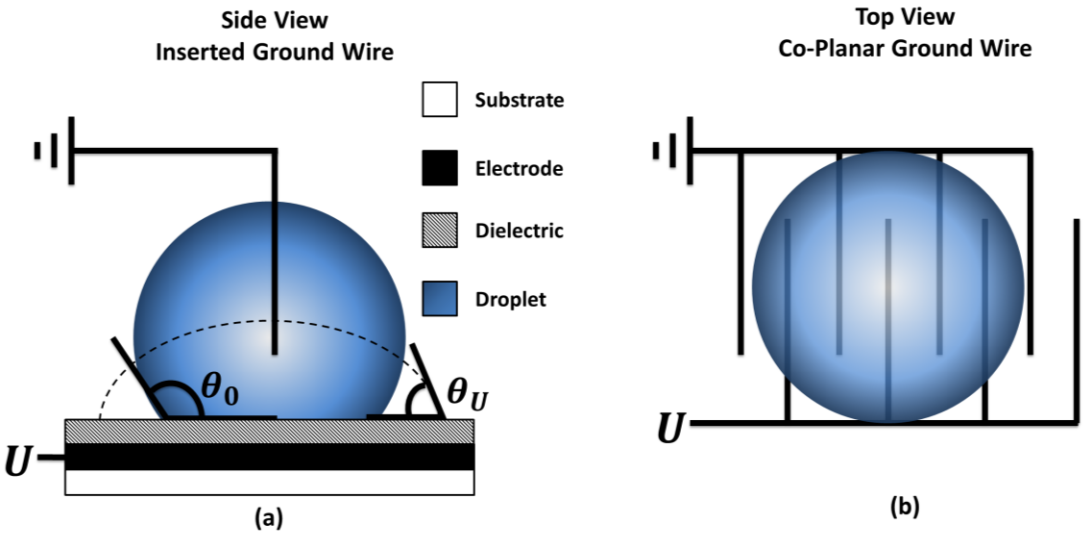

Figure 1.17: Sketch of typical electrowetting on dielectric (EWOD) setup with an (a) inserted ground wire or (b) co-planar ground wire. As a voltage is applied through the droplet the apparent contact angle changes from θ_0 to θ_U.

Once a voltage is applied between the electrode of an EWOD device the apparent contact angle of the droplet decreases. This electrowetting process is described by the Young-Lippmann (or electrowetting) equation (Fig. 1.18) (Eq. 1.17) [57]:

$$cos\theta_U = cos\theta_0 + \eta \, . \tag{1.17}$$

Here θ_U represents the voltage-dependent apparent contact angle in the system, θ_0 represents the apparent contact angle of the system at zero voltage, and η is the dimensionless electrowetting number. The elctrowetting number is a ratio of electrical energy at the solid-liquid interface to the interfacial energy at the liquid-medium interface (Eq. 1.18):

$$\eta = \frac{cU^2}{2\gamma_{LV}} , \tag{1.18}$$

where γ_{LV} represents the interfacial tension between the fluid droplet and the ambient medium, U represents the voltage, and c is the capacitance per unit area between the fluid droplet and the electrode for a typical inserted ground wire setup given by (Eq. 1.19):

$$c = \frac{\varepsilon_r \varepsilon_0}{d} , \tag{1.19}$$

where ε_r is the dielectric constant of the insulator, ε_0 represents vacuum permittivity, and d is the thickness of the insulating layer.

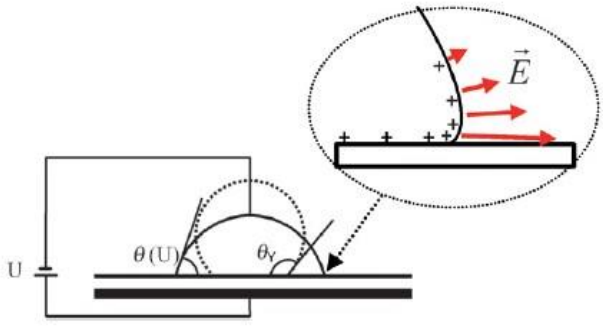

Figure 1.18: Schematic of a generic electrowetting setup at zero applied voltage (dashed line), and with an applied voltage (solid line). An electric field at the contact line is presented (red arrows) [57].

1.5.2 AC Actuation

The application of an Alternating Current (AC) [43,44] electric field has been used to modify the evaporation and pattern formation of colloidal suspensions. Eral et. al. used a transparent Indium Tin Oxide (ITO) electrode patterned device covered in a 5 μm layer of SU8 with an advancing and receding contact angle of $\theta_a = 85°$ and $\theta_r = 60°$, respectively. A root-mean-square voltage of $V_{rms} = 200\ V$ was applied to a colloidal droplet at varying frequencies to understand the effect of AC electrowetting on particle deposition during evaporation (Fig. 1.19). As a voltage is applied to the colloidal droplet, the apparent contact angle reduces increasing the surface area of the droplet, and increasing the evaporative flux.

The observed suppression of the coffee stain was attributed to (i) prevention of pinning at the TCL and (ii) internal flow fields produced by the AC that counteracted the evaporative flux. Experimental results observed are in Figure 1.20 [44].

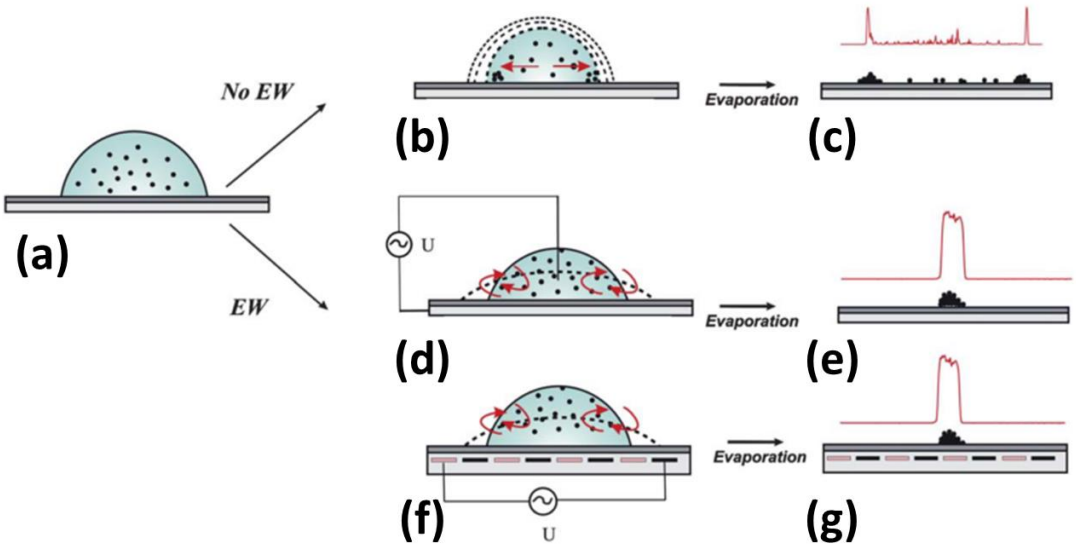

Figure 1.19: Illustration of (a) a colloidal droplet on a surface, (b) evaporation without electrowetting (EW), (c) the resultant coffee stain formation, (d) evaporation with AC EW in the conventional setup, (e) the resultant deposition, (f) evaporation with AC EW in an interdigitated electrode set up, and (f) the resultant deposition [44].

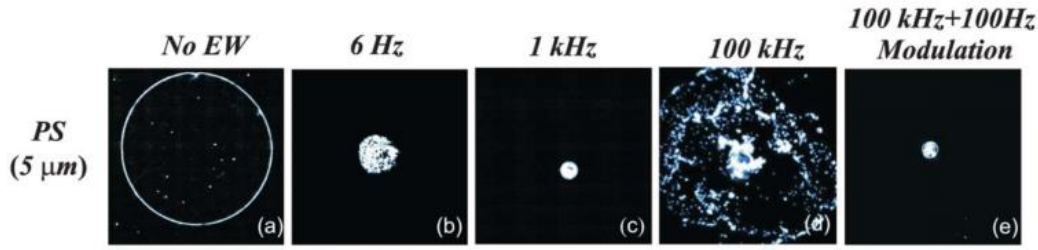

Figure 1.20: Top down deposition patterns of an aqueous colloidal suspension containing $5\mu m$ diameter polystyrene particles after (a) no electrowetting (EW), and AC EW with $V_{rms} = 200\ V$ at frequencies of (b) 6 Hz, (c) 1 kHz, (d) 100 kHz, and (e) 100 kHz + 100 Hz Modulation [44].

In [43] a regime map was created to study the effects of volume fraction of particles to fluid ϕ and the size of the particles on the ability to suppress the coffee stain formation with AC EW (Fig. 1.21).

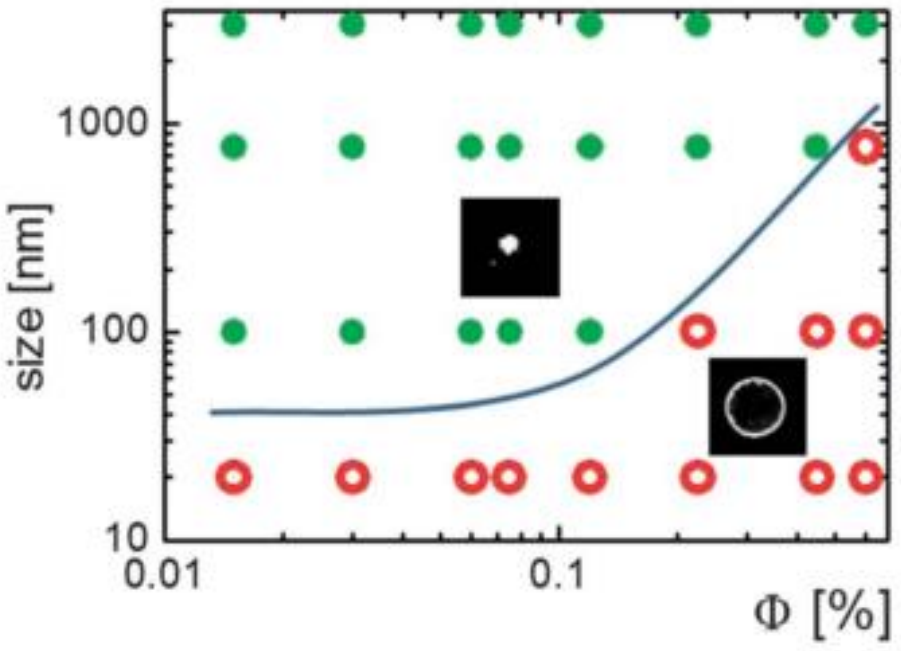

Figure 1.21: Regime map of coffee stain suppression for polystyrene particles based on volume fraction ϕ and particle size using AC EW where voltage is 300 V at 1 kHz frequency. The green solid circles represent successful suppression of the coffee stain, and the red open circles represent unsuccessful suppression [43].

Interestingly, Eral et. al. used two different geometries (Fig. 1.19): inserted ground, and a co-planar ground wire. It is unclear whether they differentiate between the two cases, but it seems implied that the applied voltage was the same in both cases. Other works suggest that the electrowetting force changes with electrode pattern [64–66]. However in [43,44], the effect of electrode geometry has not been studied in the cases presented. The regime map presented in [43] was also generated at a single voltage. While they did not see an electrophoretic / dielectric force in the AC case, the presence of that force on the particles should be dependent on many factors (i.e. applied voltage, electrode geometry, electrode orientation, particle type, carrier fluids, et cetera). All of these factors should be considered.

In [65], a coplanar electrode pattern was used that is similar to the coplanar electrode pattern presented in [43,44] (Fig. 1.22). A $\sim$50 Å thick chromium and $\sim$1000 Å thick gold metal layer was used for the electrodes. Silicon dioxide at a thickness of $\sim$3000 Å was used as the dielectric layer. Cytop® at a thickness of $\sim$2000 Å was used as the hydrophobic layer.

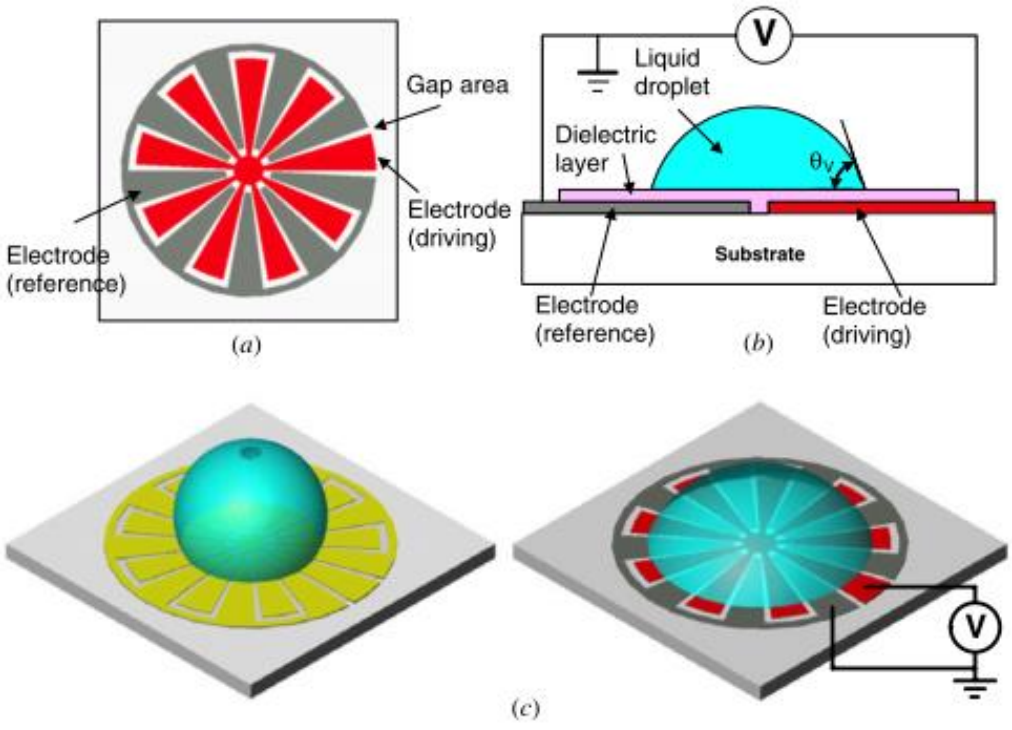

Figure 1.22: A sessile droplet on a coplanar electrode: (a) top view of electrode arrangement, (b) side view of electrode arrangement with an applied voltage, and (c) a representation of the apparent contact angle when a voltage is applied [65].

When modeling the apparent contact angle change due to an EW force, the capacitance per unit area between the electrode and the fluid droplet is very important. The capacitance per unit area governs the electrowetting behavior as shown in Equations 1.17 – 1.19. When modifying the electrode shape and geometry the capacitance per unit area changes, and the Young-Lippmann equation must be modified to properly model the behavior of the droplet under actuation. The Young-Lippmann equation was modified in [65] to account for the gap area of insulating material between electrodes by using Equation 1.20:

$$cos\theta_U = \frac{\varepsilon_r \varepsilon_0}{2\gamma_{LV} d}\left(\frac{A_d}{A_t}\left(\frac{A_r}{A_d+A_r}\right)^2 + \frac{A_r}{A_t}\left(\frac{A_d}{A_d+A_r}\right)^2\right)U^2 + cos\theta_0 \,, \tag{1.20}$$

where θ_U and θ_0 are the apparent contact angle at an applied voltage U and at zero applied voltage, respectively, ε_r and ε_0 are the dielectric constant of the insulator and a vacuum, respectively, γ_{LG} is the interfacial surface tension at the liquid-vapor interface, d is the dielectric layer thickness, and A corresponds to the area, where A_d is the area of the driving electrode, A_r is the area of the reference electrode, and A_t is the total area of the electrode. Various gap areas were modeled in [65], and plotted versus experimental data illustrating the importance of the capacitance per unit area on the apparent contact angle change that was not presented in [43,44] (Fig. 1.23).

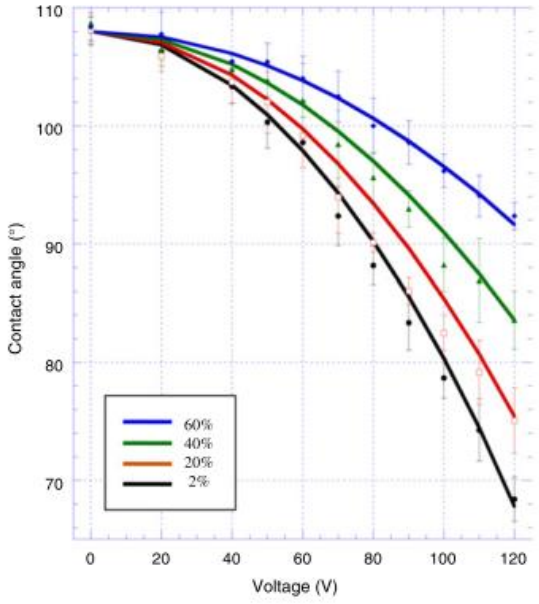

Figure 1.23: The apparent contact angle change of an EWOD setup with coplanar electrodes at various gap spaces. Experimental data and theoretical curves are presented [65].

1.5.3 DC Actuation

Particles suspended in a polar liquid may acquire a charge resulting in different particle-particle and particle-medium interactions. Application of a DC voltage deforms the droplet interface and provides a net force on particles within the droplet, inducing an electrokinetic motion that drives the particles to the electrode with the opposite charge (i.e. electrophoresis, EP). Many factors influence how these particles deposit including: (i) particle size, (ii) particle charge, (iii) DC field strength, and (iv) DC field direction.

This electrophoretic phenomenon has been used to suppress the coffee stain effect with a ground electrode inserted into a 3 μL colloidal droplet (Fig. 1.24) [45]. In [45], the application of a DC EW field on 25 nm TiO_2 particle-laden sessile droplet applies an EP force on the particles. The EP force dominates over the advective force driven by evaporation (Fig. 1.24a). As such, particles are drawn down to the surface much faster than they are drawn out to the TCL. The resultant deposition patterns observed were more uniform due to a continuous and smoother recession of the contact line by applying a constant electrowetting force on the contact line (Fig. 1.24b) The DC EW also effectively suppressed a "stick-slip" regime where the contact line pins and unpins repeatedly (Fig. 1.24c).

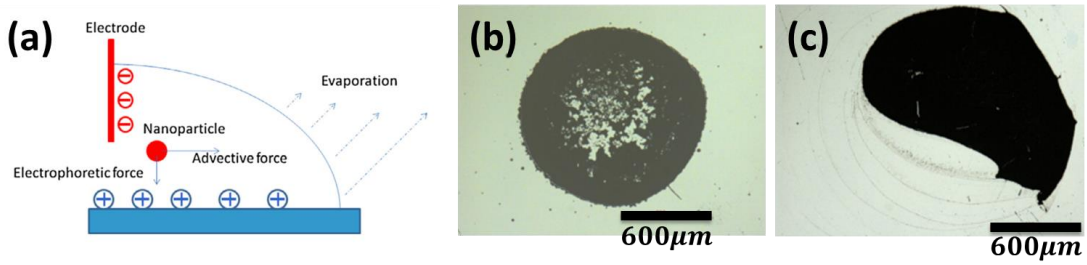

Figure 1.24: (a) Side view image of sessile droplet under DC electrowetting actuation with the advective and electrophoretic force acting on the nanoparticle during evaporation. Top view images of evaporative deposition pattern of 0.1 % TiO_2-water nanofluid after (b) DC EW with voltage $V = 18\ V$ and (c) free evaporation [45].

The relative strength of the advective and electrophoretic forces has been studied by comparing their characteristic velocities [45,67–69]. The electrophoretic velocity v_{ep} used in [45] was based on two forces. A vertical force from the DC voltage U induced electric field E acted on the nanoparticle toward the surface, $F \downarrow = qE$, where $E = -\delta U/\delta y \approx U/h$, q is the charge on the particle, y is the vertical distance, and h is the droplet height. A Stokes-type viscous force, $F \uparrow = 6\pi\mu a v_{ep}$ acted against this, where μ is the liquid viscosity, and a is the particle radius. The balance of these forces gives Equation 1.20:

$$v_{ep} \approx \frac{qU}{6\pi h\mu a}, \tag{1.20}$$

An isolated spherical particle has a zeta-potential that can be calculated using Equation 1.21:

$$\zeta = \frac{q}{4\pi\varepsilon_r\varepsilon_0 a} - \frac{q}{4\pi\varepsilon_r\varepsilon_0\left(a+\frac{1}{k}\right)} = \frac{q}{4\pi\varepsilon_r\varepsilon_0 a(ka+1)}, \tag{1.21}$$

where ε_r is the permittivity of the fluid, ε_0 is the vacuum permittivity, and $1/k$ is the Debye length. The particle size plays a significant role on the electrophoretic velocity [45,67–69]. When ka is smaller than unity, the effective charge of the particle can be represented by Equation 1.22:

$$q = 4\pi a\varepsilon_r\varepsilon_0\zeta, \tag{1.22}$$

The electrophoretic velocity v_{ep} used in [45] was valid for particles on the order of nanometers, and was calculated using Equation 1.23:

$$v_{ep} = \frac{2}{3}\frac{\varepsilon_r\varepsilon_0}{\mu}\zeta\frac{U}{h}, \tag{1.23}$$

A simplified model derived from Deegan et. al. was used to quantify the advective velocity v_{adv} found in [45] (Eq. 1.24):

$$v_{adv}(r) \approx \frac{r}{2h}\left(K - \frac{J_0}{\rho}\right), \tag{1.24}$$

where r is the radius of the droplet, K is the linear constant of the droplet height change over time, J_0 is the evaporative flux of a flat meniscus, and ρ is the liquid density.

To compare the importance of the advective force and the electrophoretic force, a ratio $\bar{R}$ of timescales t based on the advective and electrophoretic velocity was used (Eq. 1.25):

$$\bar{R} = \frac{t_{adv}}{t_{ep}} \approx \frac{v_{ep}}{v_{adv}} \frac{d_{adv}}{d_{ep}} \approx \frac{\varepsilon_r \varepsilon_0}{\eta r \dot{h}} \zeta U \ . \tag{1.25}$$

Qualitatively, when $\bar{R}$ is large, the particles move to the surface at a faster rate than they move to the contact line, resulting in a more uniform deposition.

An electrophoretic effect was characterized by $v_{ep} \approx 100.0\ \mu m/s$ with a corresponding migration distance and characteristic time of $1.4\ x\ 10^{-3}\ m$ and $10\ s$, respectively. The advective effect was characterized by $v_{adv} \approx 10.0\ \mu m/s$ with a corresponding migration distance and characteristic time of $1.0\ x\ 10^{-3}\ m$ and $100\ s$, respectively.

No previous work in this area has examined repulsive DC fields which could recirculate the particles. However, using an inserted ground in these cases may cause deposition on the inserted electrode and not the substrate, so the EW setup and geometry should be considered. Additionally, recirculation may have two effects: (i) enhancing of the "coffee stain" formation in a droplet that was in the CCR regime by bringing more of the particles to the ring or (ii) enhancing the uniformity and reducing the size of a spot that was normally in the CCA regime by further unpinning the contact line allowing it to move more freely.

2.0 GAPS IN THE RESEARCH

Electrowetting on dielectric (EWOD) has been successfully used to control the deposition patterns left by the dispersed phase in colloidal suspensions using both AC and DC. In EWOD applications, the introduction of an electric field can alter the interface shape of a sessile droplet provided that the droplet is (i) grounded and (ii) separated from the active electrode by a dielectric layer to prevent electrolysis.

Application of an AC field at moderate frequencies has resulted in a transient electrowetting (EW) force on the Triple Contact Line (TCL) without applying a net force to the dispersed phase. This suppresses the coffee stain effect by delaying contact line pinning of the liquid on the substrate which results in smaller, more uniform depositions.

Application of a DC field results in a constant EW force on the TCL while introducing a net electrophoretic force on the dispersed phase within the droplet. It has been shown that an attractive electrophoretic force can dominate over evaporative effects typically seen in coffee stain depositions. This results in a large uniform deposition on the substrate.

While both AC and DC actuation schemes have been used to successfully suppress the coffee stain effect, several fundamental questions remain open. A partial list of outstanding questions is listed below:

1. **How does surface selection affect the resultant deposition pattern observed in electrowetting assisted desiccation?** Electrowetting on dielectric requires the introduction of a dielectric layer between the droplet and the actuation electrode. Many polymers have been used in electrowetting on dielectric studies including Cytop, Teflon, SU-8, SiO_2, and Parylene. Selection of these materials should be optimized for applications interested in suppressing or enhancing the coffee-stain effect.

2. **How do the shape and orientation of the actuation and ground electrodes affect the wetting behavior of a droplet?** Eral et. al. discuss the use of both an inserted ground electrode and a co-planar interdigitated electrode array. These cases are discussed in a manner that suggests that the cases are interchangeable, while other electrowetting studies have found that electrode geometry is an important factor in the evolution of apparent contact angle with applied voltage.

3. **How does the observed desiccation pattern change with the amplitude of the applied voltage?** The reduction in apparent contact angle due to the electrowetting force is not infinite. At some applied voltage, contact angle saturation occurs and the observed apparent contact angle no longer follows the Young-Lippmann equation. This saturation would not necessarily occur for the electrophoretic force. All studies in both AC and DC actuation select an applied voltage that is above the saturation voltage. The effect of applied voltage in these cases has not been studied.

3.0 RESEARCH QUESTION

Electrowetting (EW) actuation may offer the ability to enhance or suppress of the coffee stain effect in a variety of applications. However, implementation of this technique requires that the colloidal droplet be separated from the active electrode by a dielectric layer [43–45,50–52,54,57–66] to prevent electrolysis. The addition of a dielectric polymer surface is an important variable for colloidal deposition [9–37]. Once a polymer layer is implemented, Electrowetting on Dielectric (EWOD) actuation has the potential to dynamically control colloidal deposition left by desiccated droplets to either suppress or enhance the coffee stain effect. It may also allow for independent control of the fluidic interface and deposition of particles via EW and electrokinetic forces.

EW assisted desiccation of colloidal suspensions has been achieved using multiple electrode geometries [43–45]. While no distinction is made between the performance of different electrode geometries in [43,44], pervious works have shown that electrode geometry affects the EW force [64–66] and thus would affect colloidal deposition.

The major goal of this thesis is to examine the question: **What are the effects of polymer selection on the drying dynamics and resultant deposition patterns of desiccated colloidal materials?**

To answer this question, this work seeks to experimentally characterize of the desiccation of colloidal droplets on substrates that are commonly used in EWOD applications. Characterization of the behavior of these systems in the unactuated case is the first step toward understanding the effect of surface selection on deposition patterns in EW assisted desiccation.

This thesis will also present preliminary data that demonstrates that the effects of

1. Electrode geometry and orientation; and
2. Magnitude of the applied voltage

on EWOD actuation of colloidal suspensions to determine if these applications are worthy of further study.

4.0 EXPERIMENTAL METHODOLOGY

This investigation seeks to understand the effects of surface selection and electrowetting actuation on the deposition patterns left by desiccated colloidal solutions. In an effort to provide a clear description of the experimental methodology used in this investigation, the this chapter provides a detailed description of the

1. Experimental facility used;
2. Device fabrication protocol;
3. Preparation of aqueous colloidal suspensions;
4. Electrowetting control system;
5. Data collection; and
6. Data analysis.

A diagram of the experimental methodology is shown in Figure 4.1.

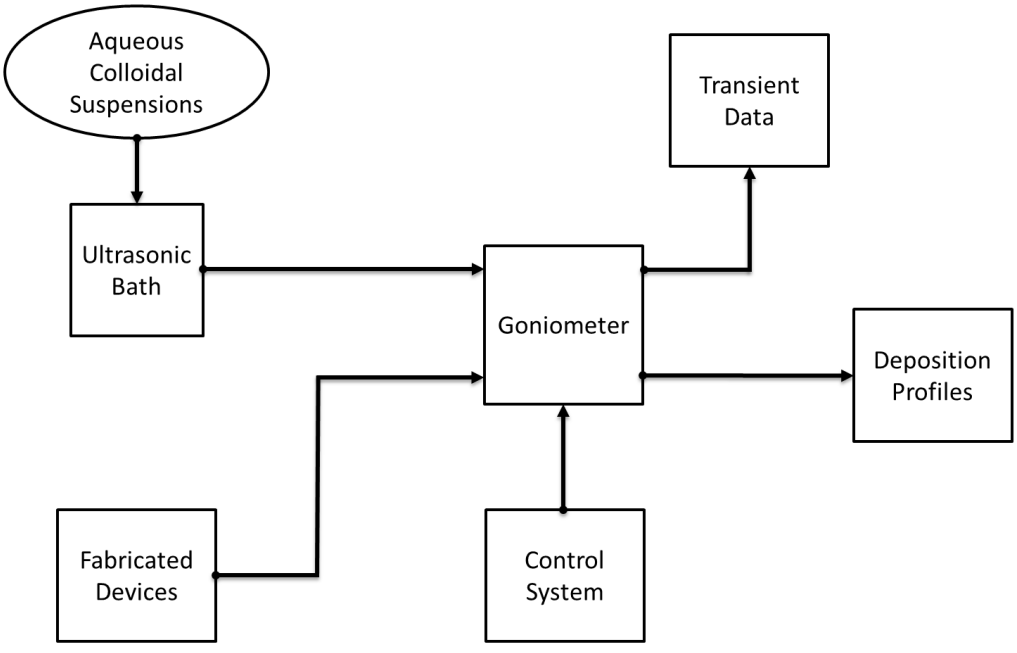

Figure 4.1: Schematic diagram of experimental methodology.

4.1 Fluids and Substrates

4.1.1 Colloidal Suspensions

Deionized water was used as the solvent for all colloidal suspensions in this investigation. It was obtained from the Semiconductor & Microsystems Fabrication Laboratory (SMFL) at Rochester Institute of Technology (RIT) with a conductivity of $18.2\ x\ 10^{-6}\ \Omega/\mathrm{cm}$.

In all cases examined here, $1.1 \pm 0.035\ \mu m$ diameter fluorescent carboxylate-modified polystyrene microspheres (Catalog Number: F-8823, Lot Number: 1173400) with a charge of $0.0175\ meq/g$ are used as the colloidal material. Aqueous colloidal suspensions at a volume fraction of 0.05 % were prepared by diluting a 2 % stock solution of commercially prepared polystyrene particles (Life Technologies) in deionized water. The 2 % stock solution was placed in an ultrasonic bath (Bransonic 1800) for 15 minutes prior to dilution. Diluted solutions were sonicated for 15 minutes in an ultrasonic bath before deposition of an aqueous colloidal suspension onto a substrate for desiccation. Similar solutions and methods were presented in [45].

4.1.2 Substrates

Substrate preparation was completed in the SMFL at RIT. Substrates were prepared to obtain flat, uniform surfaces with limited surface defects.

Glass substrates were cleaned in a soap clean solution. A lint-free cleanroom wipe was used to rid the surface of dirt and residues. Glass substrates were rinsed thoroughly with DI water, and dried by a nitrogen gun. Isopropanol was used to remove oils, and organic residues. After the isopropanol clean, substrates were rinsed with DI water, and dried again with a nitrogen gun.

Silicon substrates were cleaned using a basic Radio Corporation of America (RCA) clean in the Metal Oxide Semiconductor (MOS) RCA Bench. This RCA clean is used to remove organic containments, particles, thin oxide layer, light mobile ions, and heavier metal ions. First, the substrate is placed in a Piranha clean, a 3:1 mixture of sulfuric acid (H_2SO_4) and hydrogen peroxide (H_2O_2), at $100°C$. The Piranha clean is used to remove most organic matter. Next, the substrates are rinsed with DI for 5 minutes. The substrates are then placed in the Standard Clean 1 (SC-1), a 5:1:1 solution of DI water (H_2O), aqueous ammonium hydroxide (NH_4OH), and

aqueous hydrogen peroxide (H_2O_2), at $75°C$. The SC-1 is used to remove organic matter, and particles, however a thin layer of oxide is grown chemically by the hydrogen peroxide. The substrates are rinsed in DI for another 5 minutes, and placed in a 50:1 solution of H_2O, and Hydrofluoric acid (HF) for 1 minute to remove the thin oxide layer. Next, the substrates are placed in the Standard Clean 2 (SC-2), a 5:1:1 solution of DI H_2O, aqueous hydrochloric acid (HCl), and aqueous H_2O_2 at $75°C$. The SC-2 is used to remove metallic contaminants. Finally, the substrates are rinsed for 5 minutes, and then placed in the Spin Rinse/Dryer (SRD).

Substrates were left bare or coated with a polymer layer to compare a range of equilibrium/resting contact angles on hydrophilic to hydrophobic surfaces (Table 4.1). Surfaces investigated include: Glass, Kapton HN, SU-8 3005, and Teflon Amorphous Fluoropolymer (AF).

Table 4.1: Equilibrium contact angle θ_0 of Teflon AF, SU-8 3005, Kapton HN, and Glass.

Surface		**Teflon AF**	**SU-8 3005**	**Kapton HN**	**Glass**
θ_0	[°]	120.49 ± 5.35	88.68 ± 4.68	88.65 ± 5.01	23.87 ± 4.68

4.1.3 EWOD Device Fabrication

Device fabrication was completed in the SMFL at RIT. A side view of the device layout is presented in Figure 4.2a, and an example completed device is presented in Figure 4.2b.

Silicon substrates are scribed, and a basic RCA clean is performed in the MOS RCA Bench as explained in section 4.1.3 (Fig. 4.3a). The clean silicon wafers have a layer of Silicon Dioxide (SiO_2) grown to a thickness of approximately *5000 Å*, electrically insulating the substrate (Fig. 4.3b). The SiO_2 growth is completed in the Bruce Furnace with a wet oxidation process. The wet oxidation process uses hydrogen gas, and oxygen which produces steam to increase the rate of SiO_2 growth.

A metal layer is deposited using the CVC 601 DC Sputter Tool with a Physical Vapor Deposition (PVD) process. Electrodes are formed by depositing and patterning a 8000 Å layer of aluminum (Fig. 4.3c). Sputter deposition is a PVD process where energetic ions generated in a DC plasma are accelerated towards a "target". Energy is transferred into the target material allowing it to

sputter onto your substrate. Dummy wafers are included in this process to measure the actual thickness of the Al sputter with the Tencor P2 Profilometer.

The metal layer was patterned using standard photolithographic techniques (Fig. 4.3d-h). A positive photoresist (PR) is spun onto the aluminum using the CEE Manual Photoresist Spinner at a thickness of $1.5\mu m$ (Fig. 4.3d). The PR was measured with the Nanometrics Spectrophotometer. The photoresist was covered with a positive mask that will define the geometry of the electrodes and exposed to UV light with the Karl Suss MA150 Contact Aligner (Fig. 4.3e). The exposed photoresist was removed after being developed in the CEE Manual Photoresist Developer (Fig. 4.3f). The exposed metal was etched in the Aluminum Etch Wet Bench (Fig. 4.3g) and inspected at the Leica Inspection Station to make sure the aluminum was completely removed and no undercutting was present. The photoresist was stripped in the Positive Resist Solvent Strip Wet Bench (Fig. 4.3h).

A SiO_2 dielectric layer was used when an insulating layer was needed. The dielectric layer was deposited using a Plasma Enhanced Chemical Vapor Deposition (PECVD) process using the AME P5000. Tetraethyl Orthosilicate (TEOS) is used as source to deposit the silicon dioxide (Fig. 4.3i). TEOS is heated up to 390 °C, the wafer is brought into the chamber, and is subject to a Radio Frequency (RF) Plasma. This layer is patterned using standard photolithographic techniques similar to the metal layer to expose the bond pads (Fig. 4.3j). However the etching of the silicon dioxide is completed in the Drytek 482 Quad Etcher (i.e. Reactive Ion Etcher).

Various hydrophobic layers are deposited over the patterned electrodes with the SCS Manual Photoresist Spinner (Fig. 4.3k). In certain cases, the dielectric layer acted as a hydrophobic layer. The overall process flow is presented in Figure 4.3.

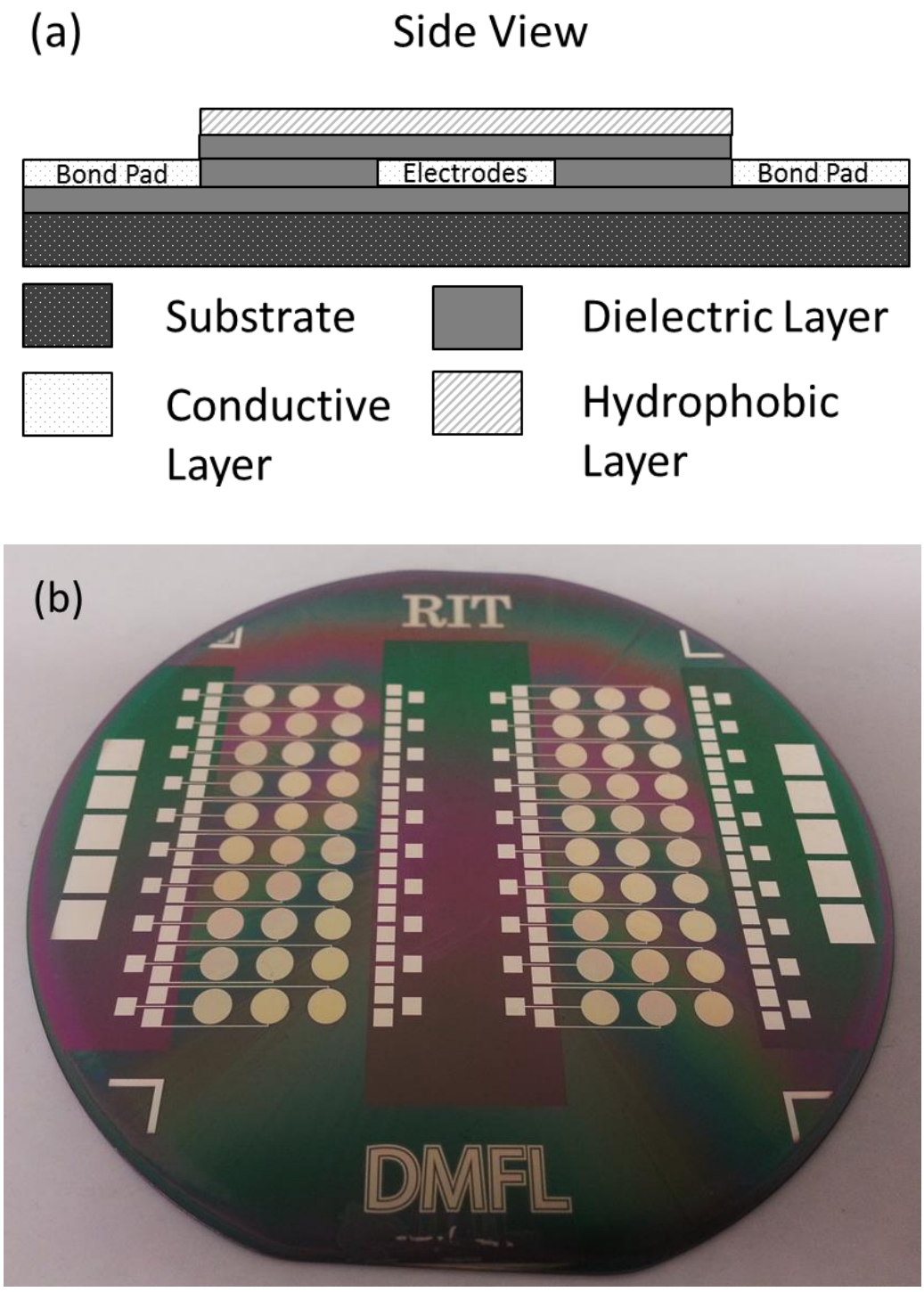

Figure 4.2: (a) Side view sketch of electrowetting on dielectric device, and (b) Top view of sample fabricated device consisting of a silicon substrate electrically insulated by silicon dioxide, patterned aluminum electrodes, and coated with SU-8 3005 as a dielectric/hydrophobic surface.

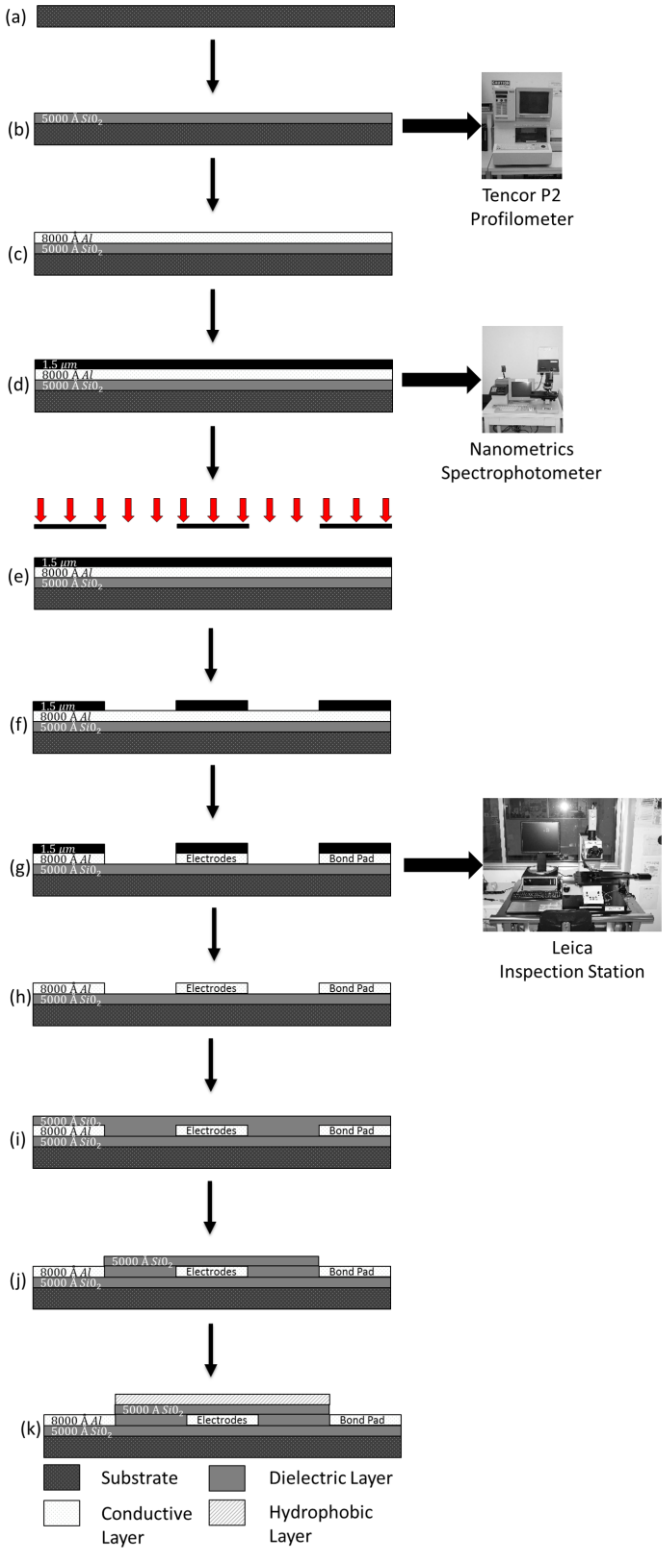

Figure 4.3: Process flow for EWOD device fabrication.

4.1.5 Substrate Surface Preparation

Surface homogeneity can affect the deposition pattern left by desiccated colloidal droplets. Using the same surface, but slightly varying how the surface is cleaned can greatly affect the droplet evaporation, and colloidal desiccation profiles obtained. A uniform, homogeneous surface is highly important for repeatable experiments [8,29,33,35]. Proper cleaning of the four surfaces (Glass, Kapton HN Polyimide Tape, SU-8 3005 Photoresist, and Teflon AF) observed in this thesis was paramount to the consistency and repeatability between experiments.

I first observed the importance of surface cleanliness on evaporation dynamics and deposition patterns when deciding on a cleaning procedure for glass slides. Two cases are presented in Figure 4.4 where aqueous colloidal suspensions of polystyrene are desiccated on two glass slides with differing cleaning protocols: (i) Glass Cleaning Protocol (GCP) A, and (ii) Glass Cleaning Protocol (GCP) B.

In GCP A, the substrate was rinsed with DI water for a minimum of five minutes, and dried via air gun. In GCP B, the substrate was immersed in an acetone bath. This bath was placed in an ultrasonic bath for 15 minutes. The glass substrates were rinsed with IPA, and dried via nitrogen air gun. Finally, an aqueous (10-1-1) solution of ($DI\ H_20 - NH_4OH - H_2O_2$) was prepared. Substrates are placed in solution for ten minutes, followed by a DI water rinse, and nitrogen air gun dry. Two 1 μL colloidal suspensions of 1.1μm diameter fluorescent PS particles were deposited onto the two glass substrates. At least 4 depositions were obtained of each cleaning protocol. Fluorescent images were acquired using Leica MZ16F fluorescence stereomicroscope, and a Sony DFW-V500 color camera. Image processing was completed to quantify the intensity over the radial position of the deposition profile in MATLAB and will be discussed in depth in Section 4.3

A representative fluorescent image of the deposition pattern left on a substrate subjected to GCP A is presented in Figure 4.4a. The resultant spot exhibits a typical coffee stain pattern. The intensity peaks sharply along the outer edge of the droplet (Fig. 4.4b). High intensity is indicative of fluorescence which occurs due to the presence of particles in a particular location. In these cases, the contact line remains pinned and the evaporative flow dominates over the Marangoni flow, which results in a coffee stain type pattern.

A representative fluorescent image of the deposition pattern after the rigorous cleaning protocol is presented in Figure 4.4c. Here, desiccation results in a concentric ring pattern. The fluorescence intensity has multiple smaller peaks as distance from the droplet center increases (Fig. 4.4d). This pattern observed resembles the slip-stick pattern discussed in [45].The intensity of the peaks seen here indicate that particles are more weakly concentrated in several rings rather than strongly concentrated at the original periphery. In this case, the contact line is initially pinned and colloidal material is deposited at the periphery. At some point, the contact line becomes unpinned and recedes. It becomes pinned again and colloidal material is then deposited at the new periphery. This process repeats itself, creating the concentric ring pattern shown in Figure 4.4c.

This preliminary work was published at the ASME 2015 International Technical Conference and Exhibition on Packaging and Integration of Electronic and Photonic Microsystems and ASME 2015 12th International Conference on Nanochannels, Microchannels, and Minichannels (InterPACKICNMM2015).

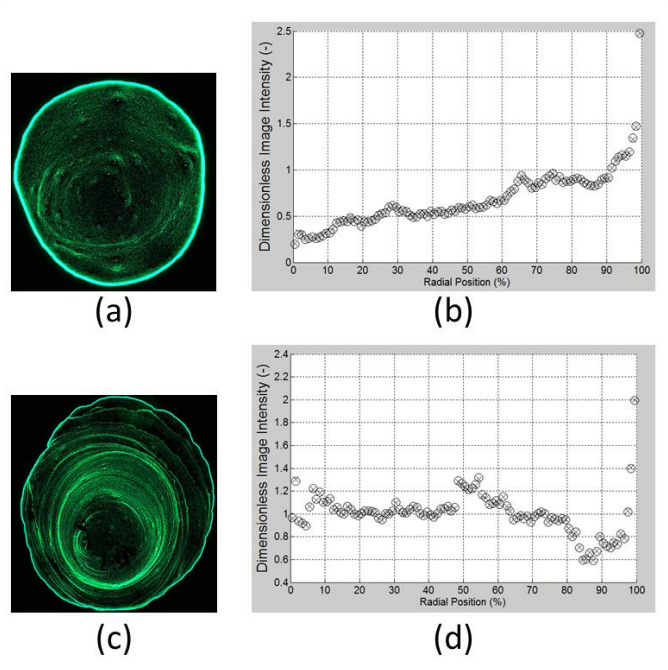

Figure 4.4: (a, c) Fluorescent deposition patterns left after the evaporation of an aqueous colloidal suspension on glass substrates and (b, d) dimensionless intensity versus radial position. Substrates were cleaned with (a-b) CP A and (c-d) CP B giving a coffee ring distribution and a slip-stick pattern.

This work showcased the ability to affect the deposition of particles on a substrate by just changing the way the surface was prepared. As a result of this work, glass surfaces were subsequently cleaned of organic residues and particulates prior to droplet desiccation. Prior to the deposition of aqueous colloidal suspensions, the substrates were cleaned with: (i) a soap clean solution, (ii) an Isopropanol bath (removal of organics), (iii) rinsed with DI H_2O for at least 5 minutes (removal of particulates), and (iv) dried with a nitrogen gun.

Kapton HN polyimide film tape was prepared in two ways: (i) Kapton CP A (KCP A), and (ii) Kapton CP B (KCP B). During KCP A the glass substrate was cleaned as previously stated to remove organics and particulates from the surface the Kapton tape would adhere to. The Kapton tape was then rolled onto the surface with a rubber roller to avoid bubbles and deformations in the surface. During KCP B an additional surface clean was implemented. The surface of Kapton was cleaned in the same manner that the Glass substrate was: with an Isopropanol bath (removal of organics), rinsed with DI H_2O for at least 5 minutes (removal of particulates), and dried with a nitrogen gun. These two cleaning procedure resulted in quite significant droplet profile depositions (Fig. 4.5). The fluorescent images produced were taken using a Leica SP5 Spectral Confocal Laser Scanning Microscope.

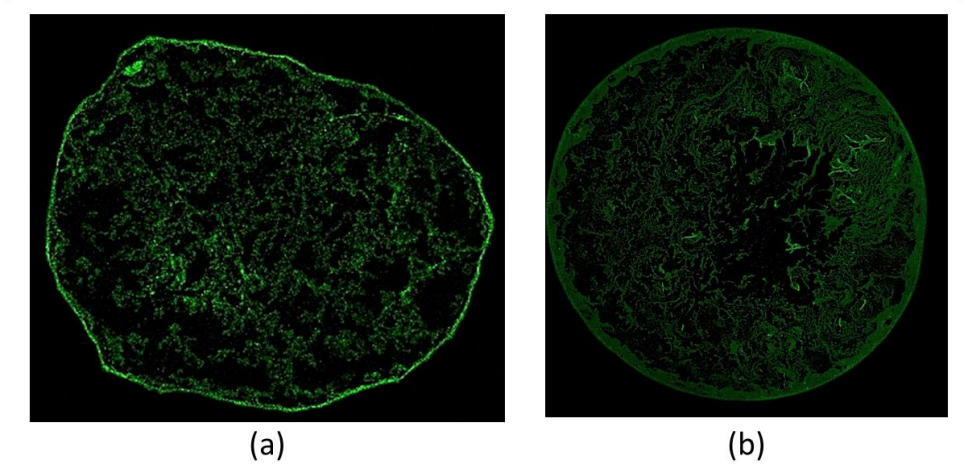

Figure 4.5: Fluorescent deposition patterns left after the evaporation of an aqueous colloidal suspension on Kapton HN where the surface was cleaned in accordance to (a) KCP A and (b) KCP B.

A fluorescent image of the deposition pattern left on a substrate subjected to KCP A is presented in Figure 4.5a. The resultant deposition pattern gives a thin highly intense coffee ring pattern with high non-uniformity along the periphery. A fluorescent image of the deposition pattern left on a substrate subjected to KCP B is presented in Figure 4.5b. The resultant deposition pattern gave a thicker less intense coffee stain pattern, however the periphery was extremely uniform. As a result of this work, when depositing on Kapton HN polyimide film tape, KCP B was used.

For certain polymers the cleaning of the surface prior to desiccation was observed to foul the surface. A deposition pattern on Teflon AF that has been cleaned (Fig. 4.6a) in the same methods as Kapton HN, performs differently compared to the surface that has not been cleaned (Fig. 4.6b). The Teflon AF surface becomes fouled easily resulting in the wetting of the droplet to the hydrophilic surface, rather than the initial hydrophobic surface. As a result, in Figure 4.6a the droplet spread out to wet the surface resulting in a very large coffee stain formation with very little solute distributed in the center of the spot. However, in Figure 4.6b the solute deposits in a very uniform manner. The fluorescent images produced were taken using a Leica SP5 Spectral Confocal Laser Scanning Microscope.

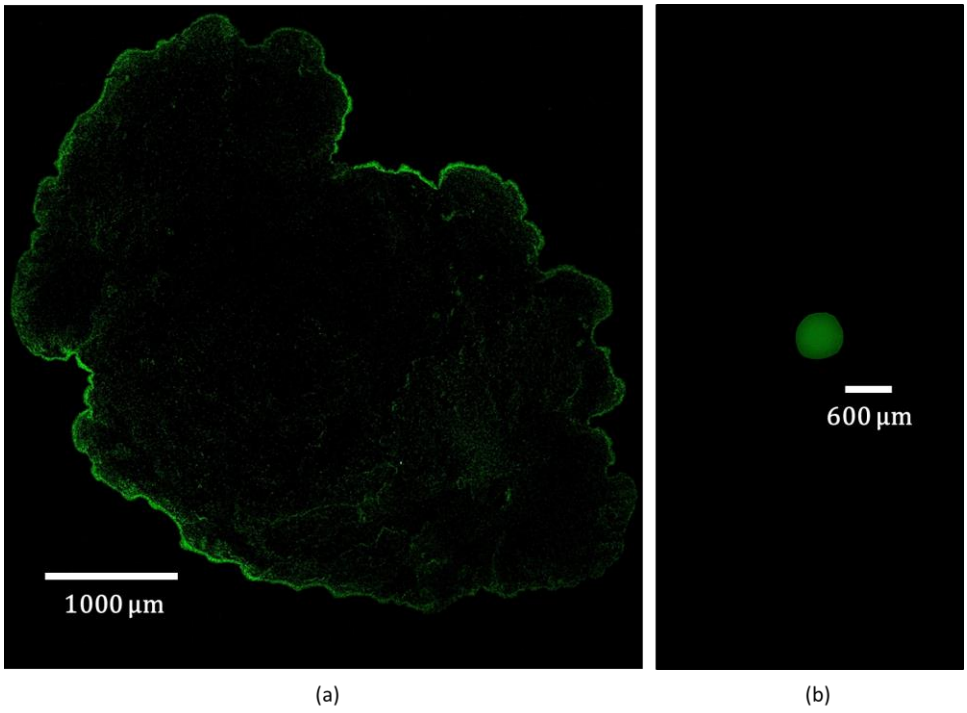

Figure 4.6: Fluorescent deposition patterns left after the evaporation of an aqueous colloidal suspension on Teflon AF where the surface was (a) fouled due to attempted cleaning and (b) not cleaned.

As a result of this work, when depositing on Teflon AF and SU-8 3005 that was just processed in the cleanroom, the surface did not undergo any additional cleaning.

These results show that surface preparation can influence colloidal deposition on the substrate. As such, care was taken to prepare each substrate in a consistent matter. Desiccation experiments were also repeated a minimum of 10 times. The average properties and statistical analysis for each case are presented below in the Results section.

4.2 Control System

Cases involving the application of an electric field in EWOD devices were completed using a control system consisting of a National Instruments PXI system (NI PXI-5402, NI PXI-4072), and a Trek PZD700A high voltage amplifier (Fig. 4.7).

A frequency signal is generated by the NI PXI-5402 Arbitrary Function Generator. The amplitude of this signal is amplified with a gain of 200 by a Trek PZD700A high voltage amplifier. Output voltage is monitored by the NI PXI-4072 Flex DMM and LCR Meter. The monitor voltage is the $1V/200V$ "step down" voltage output given by the amplifier. Amplified actuation signals used in this investigation ranged between 0 and 500 V_{RMS} at a frequency of 1 kHz.

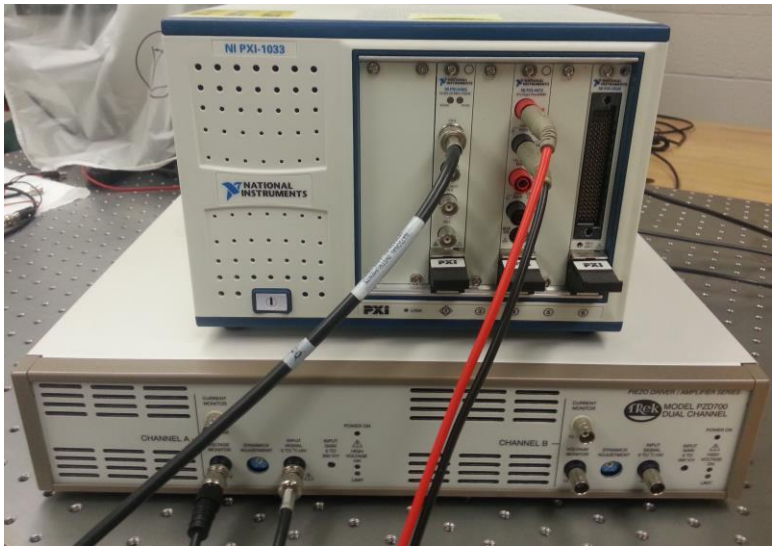

Figure 4.7: Control System consisting of a National Instruments PXI system (NI PXI-5402, NI PXI-4072), and a Trek PZD700A high voltage amplifier used during the application of an electric field in EWOD devices.

4.3 Data Collection and Analysis

The goal of this work is to quantitatively compare the deposition patterns left by desiccated colloidal suspensions on a variety of polymer substrates suitable for electrowetting on dielectric application. The transient evolution of the droplet interface during desiccation is also observed to better understand the formation of the patterns left by these suspension. Fluorescent confocal images of the desiccated deposition pattern are used to provide a quantitative analysis of the radial distribution of colloidal material deposited on the surface. These data are compared for a variety of surfaces in an effort to understand the effects of surface selection in electrowetting assisted desiccation and to provide guidelines for selecting the appropriate polymer for applications that enhance or suppress the coffee stain effect.

4.3.1 Transient Optical Measurements

The transient profile of the droplet interface during deposition was monitored using a Ramé-Hart Model 250 Standard Goniometer/Tensiometer with DROPimage Advanced software (Fig. 4.8). The droplet stage on this device was leveled and locked in place prior to desiccation. A test droplet was deposited to obtain the correct focal plane and each subsequent droplet was placed in this same plane (Fig. 4.8a).

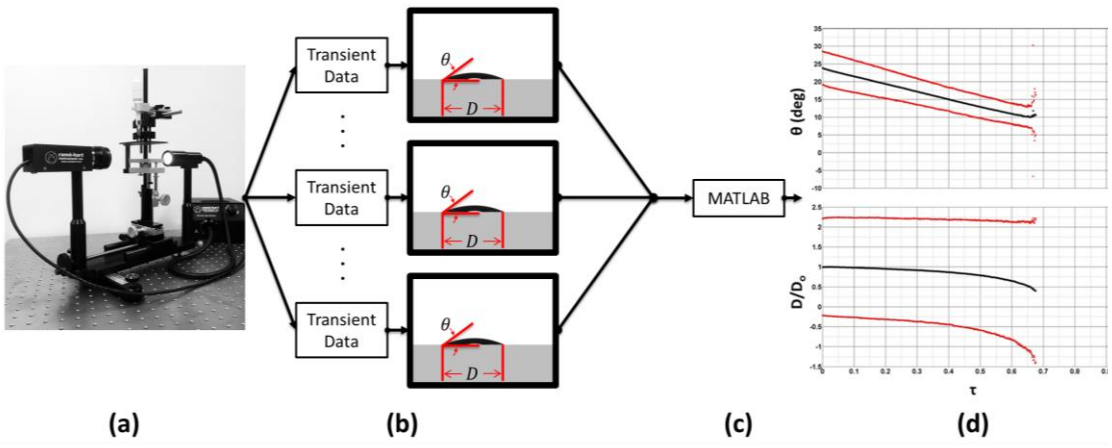

Figure 4.8: Process flow for transient optical measurements and analysis consisting of (a) Ramé-Hart 250 standard goniometer / tensiometer, (b) transient data collection, (c) MATLAB statistical analysis, and (d) general output of contact angle θ and normalized diameter D/D_0 versus normalized time τ.

During desiccation, transient measurements of contact angle and contact diameter were calculated optically using Ramé-Hart DROPimage Advanced software. A purely numeric calculation for contact angles were calculated using numerical derivation of the profile at a specified contact point. The contact point is where the droplet touches the substrate, i.e., the baseline. The contact angle was calculated by selecting a circular profile using a least squares curve fit [36]. Transient measurements were determined at a time interval of 0.5 s. This procedure was repeated 10 times for each surface examined (Fig. 4.8b).

Transient contact angle and contact diameter measurements from multiple trials on the same surface were exported into MATLAB (Fig. 4.8c). Custom code was then used to determine average values and standard deviations for the contact angles θ and normalized contact diameters D/D_0 versus normalized time τ (Fig. 4.8d). This procedure was repeated for each individual surface. The custom MATLAB code may be found in Appendix B.

4.3.2 Optical Measurements of Deposition Patterns

Fluorescent images of deposition profiles left by the desiccation of colloidal droplets presented in this work were acquired using a Leica SP5 Spectral Confocal Laser Scanning Microscope located in the Confocal Microscopy Lab (CML) at RIT (Fig. 4.9 a,b).

Image acquisition parameters were based on the size and fluorescent properties of the particles used. The Argon Laser is adjusted using the Acousto Optical Tunable Filter (AOTF) to image each sample at an excitation wavelength of 496 nm. A Leica HyD detector was used to image the range of wavelengths between 515 and 550 nm.

Low temporal and high spatial resolutions were used to define each individual particle in the deposition pattern. Each individual pixel was smaller than the size of the particles used in this experiment, so the intensity of each particle could be resolved. The gain was adjusted for each image in order to present the greatest amount of fluorescent data without oversaturation of the image. When analyzing the images the gains of the more intense images were normalized to the less intense images by taking a ratio of the gain values, so every image was based off of the lowest gain ratio scale. Gain values and corresponding gain ratios used are presented in Table 4.2.

Table 4.2: Gain values and gain ratios used for image analysis for Teflon AF, SU-8 3005, Kapton HN, and Glass.

Surface	**Teflon AF**	**SU-8 3005**	**Kapton HN**	**Glass**
Gain Value	10	20	100	100
Gain Ratio	100/10	100/20	1	1

Additionally, each surface characterized was measured to find the average intensity of the background that would be included in the imaged depositions. The background intensity of many biological samples that are generally fluorescently imaged have been found to be significant due to the added intensity from cell culture mediums and other components fluorescing. This fluorescence adds to the overall signal measured, and needs to be subtracted from the overall signal to produce accurate and precise quantitative data [70,71]. The representative background intensity was subtracted from each image processed, and the average intensity of the background of three characteristic surfaces is presented in Table 4.3. Each value has been multiplied by the gain factor represented in Table 4.2.

Table 4.3: Background intensity I_B of TeflonAF, SU-8 3005, Kapton HN, and Glass.

Surface		**Teflon AF**	**SU-8 3005**	**Kapton HN**	**Glass**
I_B	[bit]	2.90 ± 0.30	6.42 ± 1.51	0.95 ± 0.11	0.65 ± 0.12

Images acquired in the CML were analyzed with a custom code in MATLAB (Appendix B) to produce fluorescent intensity profiles of droplet depositions based on the radial position (Fig. 4.9c,d). Each deposition was not perfectly circular (Fig. 4.9b), so a methodology was created to better represent the image intensity of a non-uniform circular deposition (Fig. 4.10). The image was broken up into angular sectors (Fig. 4.10a), swept across the entire profile of the droplet (Fig. 4.10b), and sectioned into radial divisions (Fig. 4.10c). The image was quantified based on the percentage of the radial position from the center of the deposition to the radius following the contour of the deposition (Fig. 4.10d).

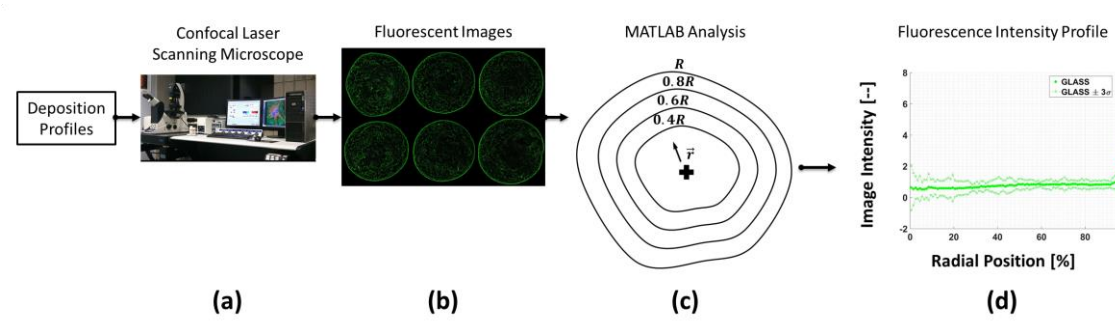

Figure 4.9: Process Flow for optical measurements and analysis of deposition profiles including (a – b) Fluorescent Image acquisition, (c) MATLAB image analysis, and (d) a general output of image intensity versus radial position.

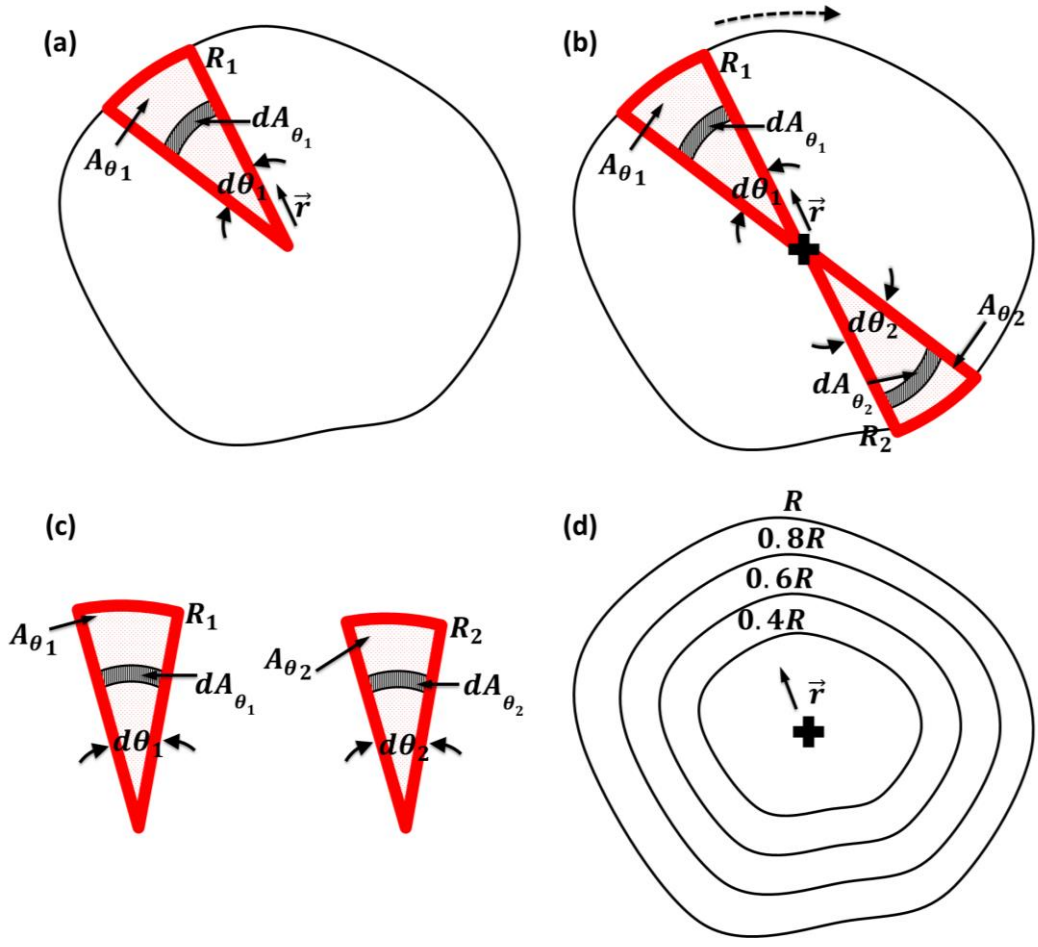

Figure 4.10: Schematic of image intensity analysis completed in MATLAB consisting of: (a) breaking up an image into angular sectors, (b) sweeping across entire profile, (c) breaking angular sectors into radial divisions, and (d) analyzing image intensity based on radial position.

The custom code created in MATLAB analyzed each fluorescent image produced in the CML. The fluorescent image was processed by:

(i) Reading in the original image (Fig. 4.11a);

(ii) Converting the RGB image to grayscale;

(iii) Setting a grayscale threshold via the Otsu Method [72];

(iv) Converting the grayscale image to black and white;

(v) Finding the largest boundary and the center point (Fig. 4.11b);

(vi) Calculating the average intensity and radius of the image;

(vii) Dividing the image up into 100 angular sectors (Fig. 4.12);

(viii) Sectioning each angular sector into 100 annular divisions → annular sectors (Fig. 4.12);

(ix) Calculating the intensity of each angular sector as a function of the local radius; and

(x) Calculating the average intensity along the radial segment of each image (Fig. 4.9d).

At least 10 images were repeated on all surfaces analyzed producing image intensity versus radial position of an image (Fig. 4.9b).

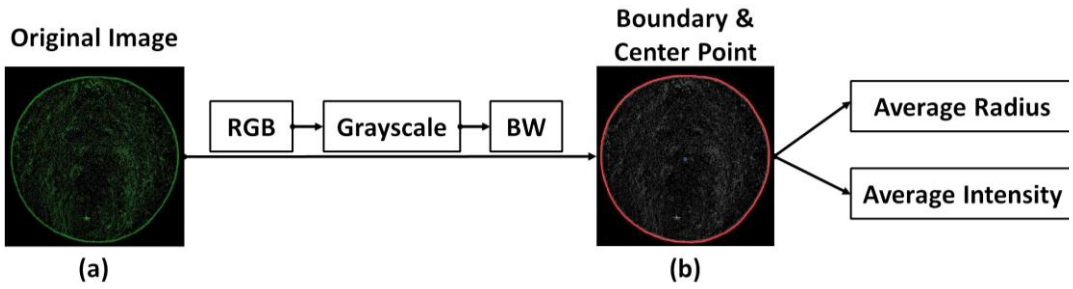

Figure 4.11: Fluorescent Image Analysis Process Flow in MATLAB: (a) input of original RGB image, conversion to grayscale, conversion to BW using the Otsu Method [72], (b) boundary and center point location, (c) resultant average intensity and radius of total droplet.

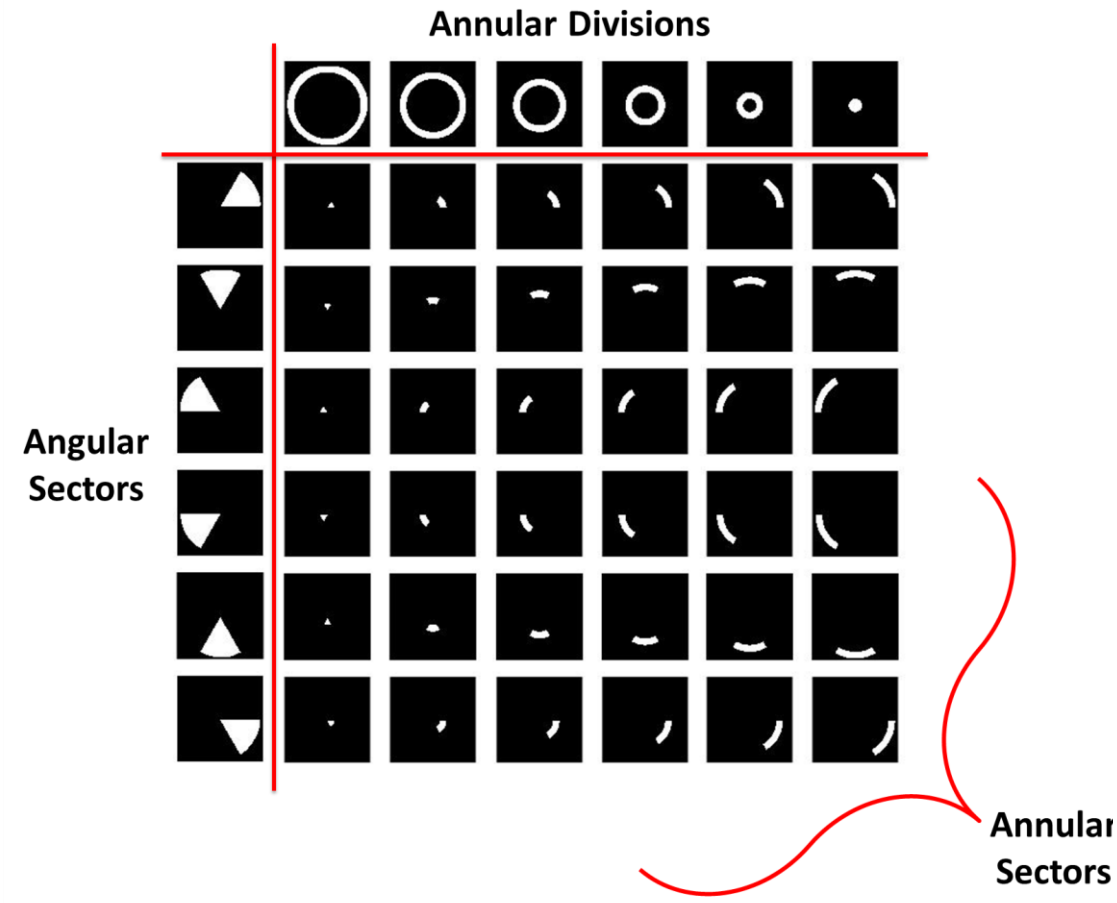

Figure 4.12: Schematic representation of the breakdown of a droplet into angular sectors that get broken up into angular divisions resulting in annular sectors. A 6 x 6 matrix division is illustrated, however during image analysis all images were broken up into 100 angular sectors and 100 annular divisions.

5.0 RESULTS & ANALYSIS

Control of aqueous colloidal deposition has advantages in combustion engines [26], micro/nano fabrication [18,37], and the manufacturing of novel optical and electronic material [28]. The presence of the coffee stain pattern is undesirable in many printing [14–16,27] and medical diagnostics processes [9,19]. Suppression of the coffee stain effect has been achieved by the application of an electric field [43–45]. While coffee stains are undesirable in many applications, they have recently been used to produce low cost transparent conductive films by controlling colloidal deposition of conductive inks [14–16] and carbon nanotubes [13]. Feature sizes were reduced by exploiting the coffee stain effect to create parallel lines from printed rivulets [14,15] and overlapping conductive rings from droplets [13,16]. Enhancement of the coffee stain effect may also be beneficial for controlled deposition of metal vapor [46] and biological structures [47].

The wide variety of applications for the enhancement or suppression of the coffee stain effect requires deposition on a variety of surfaces. Electrowetting on Dielectric (EWOD) actuation has the potential to dynamically control colloidal deposition left by desiccated droplets to either suppress or enhance the coffee stain effect. It may also allow for independent control of the fluidic interface and deposition of particles via Electrowetting (EW) and electrokinetic forces.

This work will observe the transient evolution of a droplet interface shape during desiccation as well as the resulting colloidal deposition. Qualitative and quantitative comparisons of these results will be used to compare multiple different cases in an effort to provide insight into the questions posed above. Unactuated colloidal suspensions will be desiccated on a variety of substrates commonly used in EWOD applications.

Preliminary results will also be presented examining droplets actuated via AC EW to examine the effect of electrode geometry and applied voltage on EW behavior and colloidal depositions in these cases.

5.1 Effect of Surface Selection on Colloidal Droplet Desiccation

EWOD actuation has the potential to dynamically control the contact line [43] and the motion of particles [45] in a colloidal suspension as it dried. This means of actuation has been used to suppress the coffee stain effect with AC [43,44] and DC [45] actuation. As such, it has the potential to independently control the fluidic interface and deposition of particles via EW and electrokinetic forces. A fundamental understanding of this phenomenon may also be used to develop an actuation scheme that can be used to enhance the coffee stain effect.

A dielectric material is required for EW actuation in order to prevent electrolysis. In some cases, an additional hydrophobice layer is added above the dielectric layer to increase the equilibrium contact angle of the fluid [73]. Recent works that use EW actuation to control colloidal deposition have used multiple polymer surfaces without a rationale for the selection of a specific polymer [43–45]. Since pervious works have shown that surface selection is an important criterion for colloidal deposition [8,30,31,35], it is reasonable to examine how these depositions form on substrates that are commonly used in electrowetting on dielectric applications.

Surface interaction with aqueous colloidal suspensions plays an important role in formation of deposition profiles. It seems likely that surface selection is an important parameter that should be selected carefully based on experimental or theoretical data.

5.1.1 Transient Interface Shape and Deposition Profile Left during Colloidal Droplet Desiccation on Glass and SU-8 3005

Surface interaction with aqueous colloidal suspensions plays an important role in formation of deposition profiles [26,41]. Transient interface shape and deposition profile observations can help understand how colloidal suspensions interact with various surfaces.

An aqueous colloidal suspension containing 1.1 μm diameter fluorescent carboxylate-modified polystyrene microspheres was prepared at a volume fraction of 0.05%. A $1\mu L$ droplet was desiccated on Glass and SU-8 3005 to understand the effect that adding a polymer coating has on colloidal deposition. For each case, at least 10 trials were performed. Every transient deposition was observed using a Ramé-Hart Model 250 Standard Goniometer/Tensiometer with DROPimage Advanced software to better understand the transient interface shape. Each

deposition profile left by the colloidal droplet desiccation was imaged using a Leica SP5 Spectral Confocal Laser Scanning Microscope in the Confocal Microscopy Laboratory (CML).

Colloidal deposition patterns for Glass and SU-8 3005 are shown in Figure 5.1. Addition of an SU-8 3005 layer plays an important role in the resultant distribution of colloidal material on the surface.

On Glass, the resultant deposition pattern resembles a typical coffee stain deposition, with the majority of particles deposited at the periphery of the spot (Fig. 5.1a). The initial average contact diameter $D_I = 2.85 \pm 0.52\ mm$ is approximately the same as the final deposition diameter $D_F = 2.86 \pm 0.23\ mm$ with $D_I/D_F = 0.99 \pm 0.05\ [-]$. On SU-8 3005, the resultant deposition pattern appears to be smaller, more uniform, and more intense than the deposition profile observed on Glass (Fig. 5.1b). Interestingly, the deposition on SU-8 3005 resulted in an initial contact diameter $D_I = 1.58 \pm 0.12\ mm$ and a final deposition diameter $D_F = 0.76\ \pm 0.06\ mm$, and a corresponding $D_I/D_F = 2.09 \pm 0.07\ [-]$. The observed diameter reduction suggests the contact line moves in the SU-8 3005 case, but not on Glass.

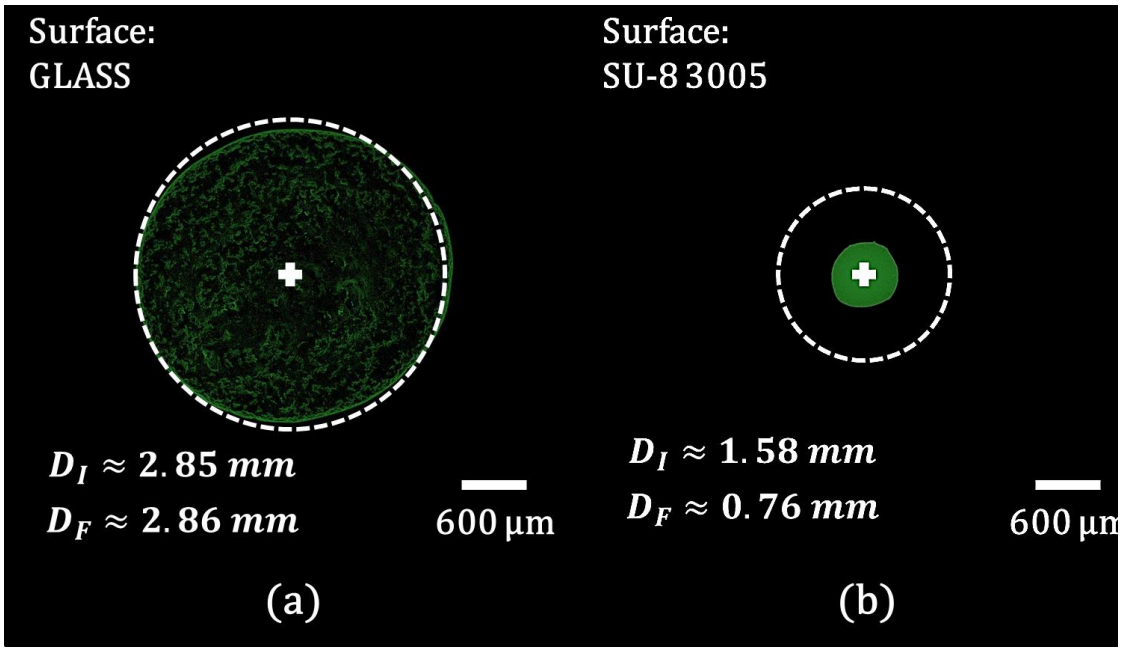

Figure 5.1: Top down view of deposition profile left during colloidal droplet desiccation on (a) Glass and (b) SU-8 3005. The initial contact diameter of the droplet is represented by a dashed line.

Fluorescent Images acquired via the CML (Fig. 5.1) were analyzed with a custom MATLAB code producing quantitative data about the resultant desiccation shape, size, and intensity profile (Table 5.1). On Glass, the average spot intensity $\bar{I}$ of the resultant deposition pattern was calculated to be $3.59 \pm 1.53\ [bit]$. On SU-8 3005, the average intensity $\bar{I}$ of the resultant deposition pattern was calculated to be $243.42 \pm 22.10\ [bit]$.

The SU-8 3005 spot is much more intense than the spot on Glass due to the smaller final diameter of the desiccation. The collection of fluorescent particles in a smaller overall final diameter results in a larger mean intensity.

Table 5.1: Equilibrium contact angle θ_0, average initial diameter D_I, average final diameter D_F, diameter ratio D_I/D_F, and average Intensity $\bar{I}$ of Glass and SU-8 3005.

Surface		**Glass**	**SU-8 3005**
θ_0	$[°]$	23.87 ± 4.68	88.68 ± 4.68
D_I	$[mm]$	2.85 ± 0.52	1.58 ± 0.12
D_F	$[mm]$	2.86 ± 0.23	0.76 ± 0.06
D_I/D_F	$[--]$	0.99 ± 0.05	2.09 ± 0.07
$\bar{I}$	$[bit]$	3.59 ± 1.53	243.42 ± 22.10

The average intensity and average final diameter data was used to normalize the intensity values and the radial positions presented in Figure 5.2. The deposition of material on Glass resembles a traditional coffee stain pattern with a maximum intensity of $17.85\ [bit]$ occurring at the periphery of the deposition. This maximum intensity is 397.8 % larger than the average intensity of the spot (Fig. 5.2a). Interestingly, the deposition pattern observed on SU-8 3005 was significantly more uniform. The maximum intensity of $293.22\ [bit]$ occurred at the center of the droplet and was only 20.5% greater than the mean. This maximum intensity held constant from 0% to around 30% of the radial position. At this point the intensity appeared to follow a decreasing trend up until around 98% of the radial position where the intensity drops off to a minimum value of $49.17\ [bit]$. The minimum intensity occurring at the periphery of the droplet is 20.2% of the mean intensity (Fig. 5.2b).

As shown in Figures 5.1 b and 5.2 b, the deposition left on SU8 is smaller, more intense and more uniform. Not only that, the final diameter of the SU-8 3005 deposition decreased to 48.1 % of the

initial diameter while the initial and final diameters on Glass are approximately equal. This suggests that drying dynamics, and particle deposition on SU-8 3005 are significantly different than those on Glass. In order to understand more clearly how the particles deposit on the substrate transient observations of the interface shape is needed.

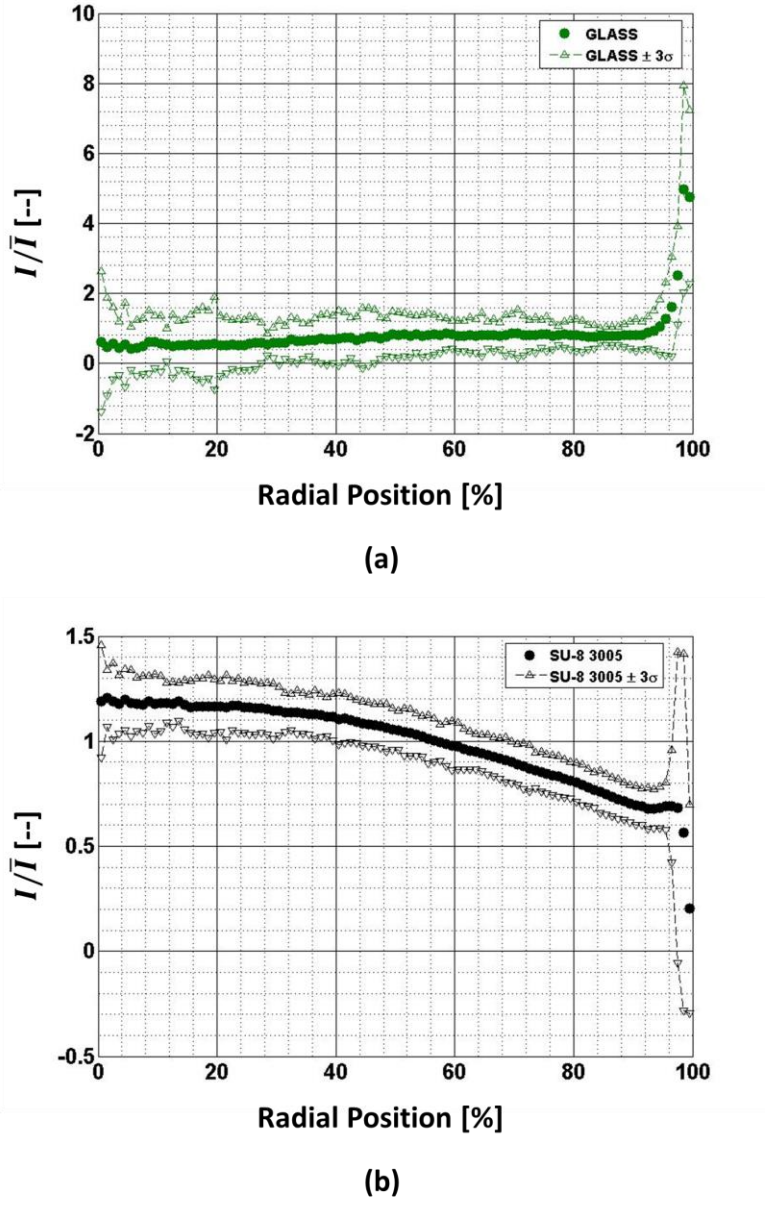

Figure 5.2: Normalized image intensity $I/\bar{I}$ versus radial position (solid dots) with three standard deviations (dashed lines) for (a) Glass and (b) SU-8 3005.

Transient deposition was observed using a Ramé-Hart Model 250 Standard Goniometer/Tensiometer with DROPimage Advanced software to better understand the transient interface shape of the sessile droplet on Glass and SU-8 3005. Backlit images of side view interface profiles for droplets containing 1.1 μm diameter fluorescent microspheres are presented in Figure 5.3. Droplets were desiccated on Glass (Fig. 5.3-Ia-g) and on SU-8 3005 (Fig. 5.3-IIa-g) with a total evaporation time of 417 ± 62 sec and 759 ± 143 sec, respectively. The total evaporation time was used to calculate the normalized time τ given in the side view transient interface shape profile presented in Figure 5.3.

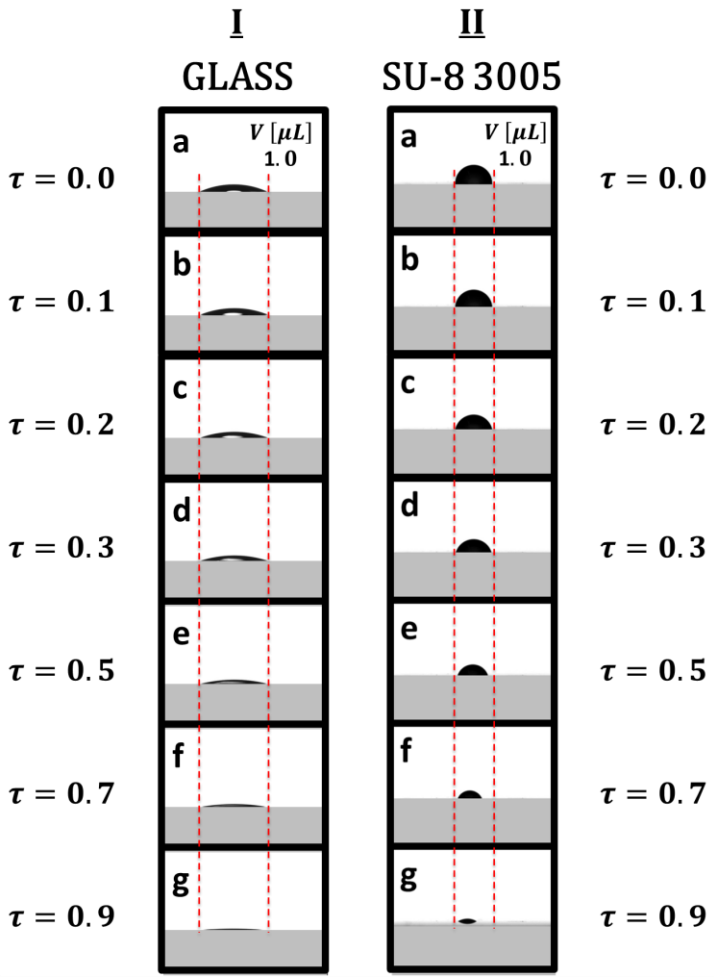

Figure 5.3: Side view images of evaporating colloidal droplet on (I) Glass and (II) SU-8 3005 at (a) $\tau = 0.0$, (b) $\tau = 0.1$, (c) $\tau = 0.2$, (d) $\tau = 0.3$, (e) $\tau = 0.5$, (f) $\tau = 0.7$, (g) $\tau = 0.9$. Red dashed lines indicate the initial contact area of the droplet on the substrate.

The contact angle θ and normalized diameter D/D_0 (where $D_0 = D_F$) profiles presented in Figure 5.4 were produced using a custom code in MATLAB that analyzed the side view images of evaporating colloidal droplets on Glass and SU-8 3005. The total drying time was used to calculate the normalized time τ presented these graphs.

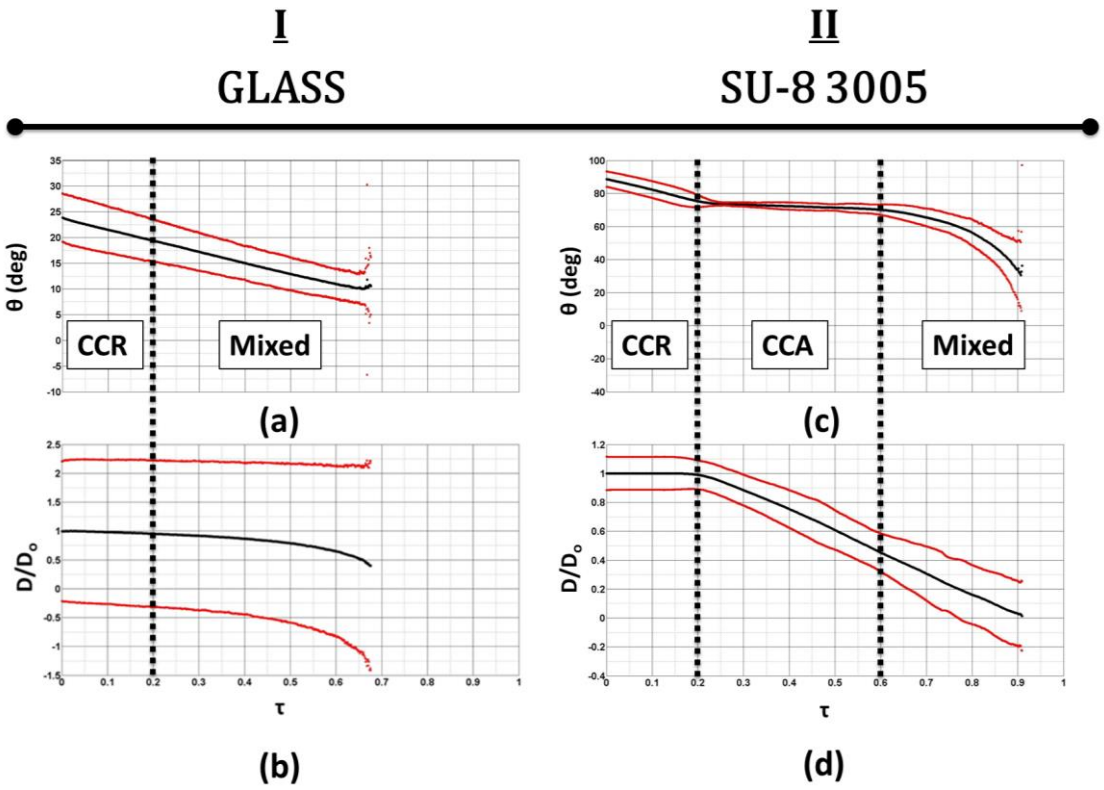

Figure 5.4: (a,c) Contact angle (θ) and (b,d) normalized diameter (D/D_0) of evaporating colloidal droplet on Glass and SU-8 3005 as a function of normalized time (τ).

Quantitative analysis of the transient contact angle and normalized contact diameter of the droplets desiccated on glass with corresponding regimes is presented in Figure 5.4a,b. For the droplets desiccated on glass, the desiccation process can be segmented into two observable regimes. These regimes are representative of the: (i) Constant Contact Radius (CCR) and (ii) mixed mode regimes observed in [26,48]. From $\tau = 0.0 - 0.2$ the Triple Contact Line (TCL) is pinned (Fig. 5.3-Ia-c). As a result the contact angle decreases from $\theta_0 \approx 24°$ to $\theta \approx 19°$ while the contact diameter remains at a constant $D \approx 2.84\ mm$ (Fig. 5.4a,b). This CCR regime we

observe occurs when the contact line is pinned. Reductions in the droplet volume are due to evaporative flux at the TCL resulting in a decreased contact angle over time. As the contact angle decreases more, the evaporative flux increases bringing more solute to the pinned TCL. At approximately $\tau = 0.2$ the contact angle and contact diameter both decrease with time (Fig. 5.4a,b) until the droplet is so small that the software cannot observe the droplet anymore (Fig. 5.3-Id-g). While the Ramé-Hart DROPImage Advanced software is unable to measure contact angles below approximately 20° reliably [74], transient side view images in Figure 5.3-Ia-c seems to be consistent with the CCR regime and Figure 5.3-Id-g seems to be consistent with the mixed phase described in [26,48] where the contact angle and diameter both reduce over time. The software picks up a decrease in the diameter that could be due to the inability for the software to detect lower contact angles resulting in inaccuracies in measurements at these low contact angles. The deposition profiles presented repeatedly gave coffee-stain patterns where the particles are drawn to the TCL indicating a pinned contact line for the majority of the desiccation.

Quantitative analysis of the transient contact angle and normalized contact diameter of the droplets desiccated on SU-8 3005 with corresponding regimes is presented in Figure 5.4c,d. For the droplets desiccated on SU-8 3005, the desiccation process can be segmented into three observable regimes. These regimes are representative of the: (i) CCR, (ii) Constant Contact Angle (CCA), and (iii) mixed mode regimes observed in [26,48]. In the CCR regime, the Triple Contact Line (TCL) is pinned from $\tau = 0.0 - 0.2$ (Fig. 5.3-IIa-c). Here, the contact angle decreases from $\theta_0 \approx 89°$ to $\theta \approx 72°$ while the contact diameter remains at a constant $D \approx 1.58\ mm$ (Fig. 5.4c,d). During this regime, the contact line is pinned and the reduction in volume caused by evaporation at the TCL results in a reduction in the contact angle over time. As the evaporative flux draws the particles to the pinned TCL, the Marangoni flow acts in the opposite direction to resuspend the particles due to the temperature gradient across the droplet. During this regime particles may be deposited at the TCL, however it is unable to view these particles optically with the software in current use.

As the contact angle decreases, the force pulling in the contact line increases. In this case, that force eventually overcomes contact line friction and the TCL slips free. A constant contact angle and receding diameter is observed from $\tau = 0.2 - 0.6$ (Fig. 5.3-IIc-e) (i.e. CCA regime). Here, the contact angle stays at approximately $72°$ while the diameter recedes to around 45% of the initial diameter (Fig. 5.4c,d). If particles were deposited onto the surface at the TCL during the CCR regime, the slipping and recession of the TCL may have resuspended these particles. This

conclusion can be drawn from the lack of fluorescent particles left on the substrate at the initial diameter as observed in Figure 5.1b.

For $\tau = 0.6$, both the contact angle and contact diameter decrease with time (Fig. 5.3-IIf,g). This is characteristic of the mixed regime that occurs due to either the combination of the contact line slipping and the contact angle decreasing or intermittent changes between both the CCA and CCR regime (Fig. 5.4c,d). It is theorized that the particles deposit onto the substrate at some point during this regime. From the transient measurements, the deposition profile is observed to reduce to 48.1 % of the initial diameter just before the droplet enters the third regime (Fig. 5.4d) at around $\tau = 0.6$. The evaporative flux continues to bring particles to the TCL, but at this point the particles start to deposit onto the surface. When observing the transient side view images, the droplet continues to reduce in diameter, and move inwards (Fig. 5.3-IIf,g). As the diameter decreases, more particles continue to deposit onto the surface while the contact line recedes inwards. The result is a greater amount of solute built up at the center than the edge of the resultant deposition. A larger overall intensity at the center of the deposition is observed (Fig. 5.2b). The larger deposition at the center may be attributed to more time to deposit in the center of the droplet or the Marangoni flow resuspending particles and bringing them to the center of the droplet to pack there. There are many forces at play when this contact line is pulling inwards and the small volume of fluid makes it difficult to observe what occurs during this regime. To understand how these particles deposit at this regime, a different method of transient observations that can individually resolve each particle is necessary for future experiments.

In future experiments, a potential improvement to this experimental setup could be the incorporation of a camera below or above the substrate to optically observe and track individual particles moving at the TCL (e.g. particle image velocimetry). Incorporation of a particle image velocimetry (PIV) transient observation can lead to better understanding of the packing order at the TCL, and motion of the streamlines in the colloidal suspension during evaporation. However, at this time the Digital Microfluidics Laboratory (DMFL) did not have this capability. Future collaboration with other partners at RIT with this technology should be pursued to improve qualitative and quantitative observations of evaporating colloidal suspensions.

For desiccated droplets, understanding the transition into different evaporative regimes is necessary for understanding how these colloidal suspensions deposit onto different substrates. The receding contact angle is of particular importance as it governs when the contact line will

unpin (Fig. 5.5). Both Glass and SU-8 3005 started in the CCR regime. In the CCR regime, the Contact Radius (CR) stays the same while the Contact Angle (CA) decreases. Since SU-8 3005 has a larger receding CA (i.e. smaller hysteresis) it makes it more likely to have a moving contact line. When the contact line recedes early in the process, suppression of the coffee stain is more likely because there is not a lot of the solute from the dispersed phase built up at the TCL. The moving contact line sweeps the solute inward resulting in most of the deposition occurring at the end of the process after the contact line has receded. Therefore, when depositing a fluid on a substrate with a large receding contact angle and a small hysteresis the resultant spot after total evaporation is observed to be smaller than the original diameter given by the equilibrium contact angle. The receding CA on Glass was too low to even be measured accurately (i.e. $< 20°$). The low receding CA resulted in the contact line remaining pinned for the majority of the process. Therefore, most of the solute is deposited at the periphery. Deposition of the solute at the periphery decreases the mobility of the contact line more by acting like a wedge. Since the CA continues to decrease, the height at the edge of the droplet is further reduced. This increases the evaporative flux at the contact line, which brings more solute to the edge of the droplet. One method to predict the evaporative regimes that a droplet on a surface will experience could be to measure the receding contact angle.

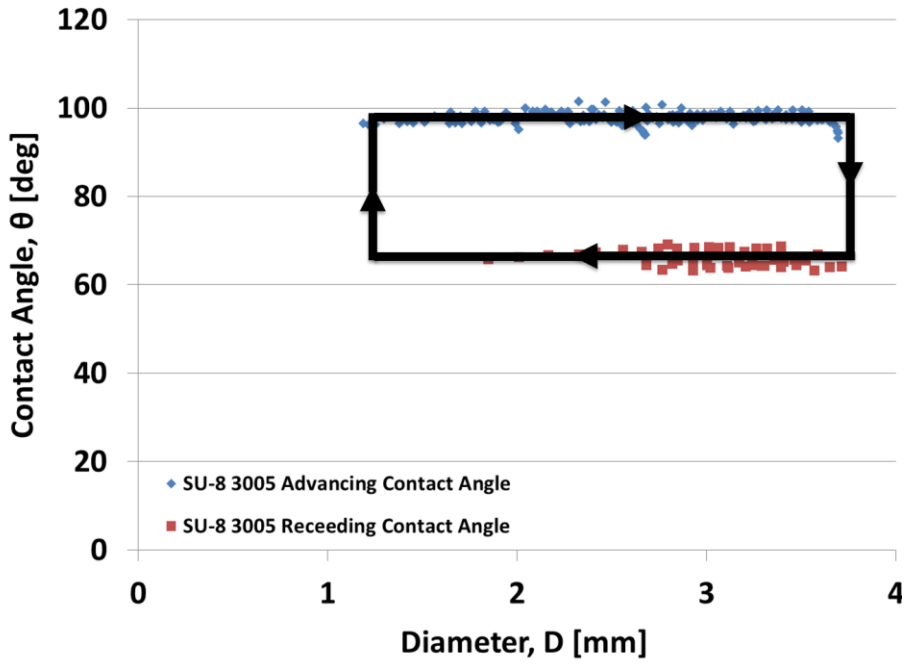

Figure 5.5: Advancing and receding contact angle of SU-8 3005. Black arrow shows the direction of fluid.

The small receding contact angle on Glass makes it harder for the contact line of a droplet to move on the substrate and was observed to stay pinned at the TCL resulting in a deposition pattern at the same diameter as the original contact diameter. The small hysteresis on SU-8 3005 makes it easier for the TCL of the droplet to move on the substrate and sweep the solute inward resulting in a smaller resultant deposition diameter than the original diameter given by the equilibrium contact angle.

In the case of Glass and SU-8 3005, the resultant deposition pattern appears to be a function of: (i) the equilibrium contact angle and (ii) receding contact angle. The equilibrium contact angle determines the initial diameter of the droplet. A decrease in the contact angle to a contact angle must occur for the contact line to move. However, the contact angle of the droplet must be reduced to some value close to the receding contact angle for the contact line to unpin. If the receding contact angle is very large (i.e. small hysteresis) the contact line has more of an ability to move. Therefore, the resultant spot after total evaporation is observed to be smaller than the original diameter when depositing a fluid on a substrate with a large receding contact angle.

The comparison of desiccation of colloidal suspensions on Glass and SU-8 3005 suggests that,

1. Initial contact diameter can be determined from the droplet equilibrium CA;
2. Reduction in contact diameter can be predicted from the receding CA;
3. Smaller depositions are expected to have a higher intensity; and
4. Droplets with mobile contact lines are expected to produce more uniform depositions.

Transition into a regime where the contact angle has been decreased to a value close to the receding contact angle (e.g. the CCA region) is beneficial for applications seeking to suppress the appearance of the coffee ring formation. This transition is easier for solid-liquid systems that have a smaller hysteresis and larger receding contact angle. Conversely, applications who seek to enhance the coffee stain pattern would benefit for the selection of a material that has a very large hysteresis and small receding contact angle resulting in a pinned TCL. These surfaces may move directly from the CCR region to the mixed region. Since different surfaces may be more appropriate for different applications, a method to identify which surfaces transition from the CCR to the CCA and mixed regimes, and at what point is necessary. Transient observations of the interface during deposition are required to understand how the final deposition pattern is formed.

5.1.2 Transient Interface Shape and Deposition Profile Left during Colloidal Droplet Desiccation on Multiple Surfaces

Section 5.1.1 shows that adding a polymer layer has the potential to impact transient interface shape and deposition patterns left during colloidal droplet desiccation. Surface interaction with aqueous colloidal suspensions plays an important role in formation of deposition profiles. Transient interface shape and deposition profile observations can help understand how colloidal suspensions interact with various surfaces. Selection of a polymer layer in EWOD assisted colloidal droplet desiccation is important and care should be taken in the selection process.

Results presented above suggest that the evaporative characteristics of an aqueous colloidal droplet may be predicted by characterizing the hysteresis of the continuous phase of the appropriate colloidal suspension. The coffee ring effect may be suppressed when transitioning into a regime where the contact angle has been decreased to a value close to the receding contact angle (e.g. the CCA region). However, the coffee ring effect may be enhanced when a material has a very small receding contact angle resulting in a pinned TCL. These surfaces may move directly from the CCR region to the mixed region. Observing the transient interface shape and deposition profile on multiple surfaces can be used to test the viability of these predictions.

The comparison of colloidal deposition on glass and SU-8 3005 suggests that the relative size, average intensity, and intensity distribution of the colloidal deposition can be predicted using the (i) equilibrium contact angle and (ii) receding contact angle. This section will use those parameters to predict the colloidal deposition patterns left on Teflon AF and Kapton HN polyimide film tape. Teflon AF was chosen as it is commonly chosen as a hydrophobic layer in digital microfluidic applications, while Kapton HN is a common material used in flexible electronics. The measured equilibrium contact angle θ_0, advancing contact angle θ_a, and receding contact angle θ_r are presented in Table 5.2.

Table 5.2: Equilibrium contact angle θ_0 and receding contact angle θ_r of Glass, Kapton HN, SU-8 3005, and Teflon AF.

Surface		**Glass**	**Kapton HN**	**SU-8 3005**	**Teflon AF**
θ_0	[°]	23.87 ± 4.68	86.05 ± 5.01	88.68 ± 4.68	120.49 ± 5.35
θ_a	[°]	N/A	N/A	97.64 ± 4.17	124.62 ± 3.90
θ_r	[°]	N/A	N/A	65.89 ± 5.55	111.92 ± 4.20

While the equilibrium contact angle is similar for Kapton HN and SU-8 3005, the receding contact angle for Kapton HN is significantly lower. The θ_r for Kapton HN was too low to even be measured accurately (i.e. $< 20°$) just like θ_r for Glass. Kapton HN is predicted to (i) have an initial contact diameter similar to SU-8 3005, (ii) have a pinned TCL for the majority of the process, and (iii) have more deposition at the periphery.

Teflon AF has an equilibrium and receding contact angle that is larger than both SU-8 3005 and Glass. Teflon AF is predicted to (i) have a smaller initial contact diameter than SU-8 3005 due to the large θ_0, (ii) have a TCL that unpins and recedes much more easily than the TCL of SU-8 3005, and (iii) have a more overall uniform deposition pattern of particles. The recession of the TCL is due to the smaller hysteresis and larger receding contact angle measured.

An aqueous colloidal suspension containing 1.1 μm diameter fluorescent carboxylate-modified polystyrene microspheres was prepared at a volume fraction of 0.05%. A 1 μL droplet was desiccated on Glass, SU-8 3005, and Kapton HN to understand the effect that adding a polymer coating has on colloidal deposition. A 2 μL droplet was desiccated on Teflon AF due to the hydrophobicity of the surface and the inability for a 1 μL droplet to disengage from the pipette tip and wet the Teflon AF surface. For each case, at least 10 trials were performed. Every transient deposition was observed using a Ramé-Hart Model 250 Standard Goniometer/Tensiometer with DROPimage Advanced software to better understand the transient interface shape. Each deposition profile left by the colloidal droplet desiccation was imaged using a Leica SP5 Spectral Confocal Laser Scanning Microscope in the Confocal Microscopy Laboratory (CML).

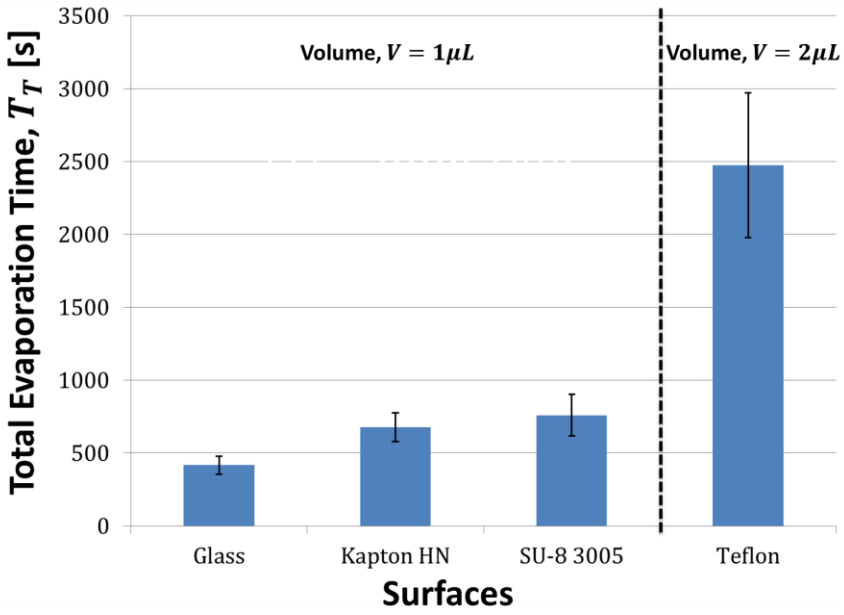

Figure 5.6: Total drying time of colloidal droplets on Glass, Kapton HN, SU-8 3005, and Teflon AF.

The total evaporation times for aqueous colloidal suspensions on Glass, Kapton HN polyimide film tape, SU-8 3005, and Teflon AF are $417 \pm 62\ s$, $678 \pm 99\ s$, $759 \pm 143\ s$, and $2475 \pm 498\ sec$ respectively (Fig. 5.6). It is worth noting that the increased evaporation time in Teflon AF is not only due to the larger contact angle, but also due to the larger volume used.

Addition of a polymer layer plays an important role in the resultant distribution of colloidal material on the surface. Representative colloidal deposition patterns for Glass, Kapton HN, SU-8 3005, and Teflon AF are shown in Figure 5.7.

Like Glass, the deposition pattern on Kapton HN resembles a coffee stain deposition. The initial average contact diameter $D_I = 1.64 \pm 0.11\ mm$ is approximately the same as the final deposition diameter $D_F = 1.64 \pm 0.12\ mm$ with $D_I/D_F = 1.00 \pm 0.09\ [-]$. The observed diameter did not seem to reduce suggesting a pinned TCL on Kapton HN. The larger initial contact angle of Kapton HN resulted in a smaller initial contact diameter than the contact diameter observed on Glass.

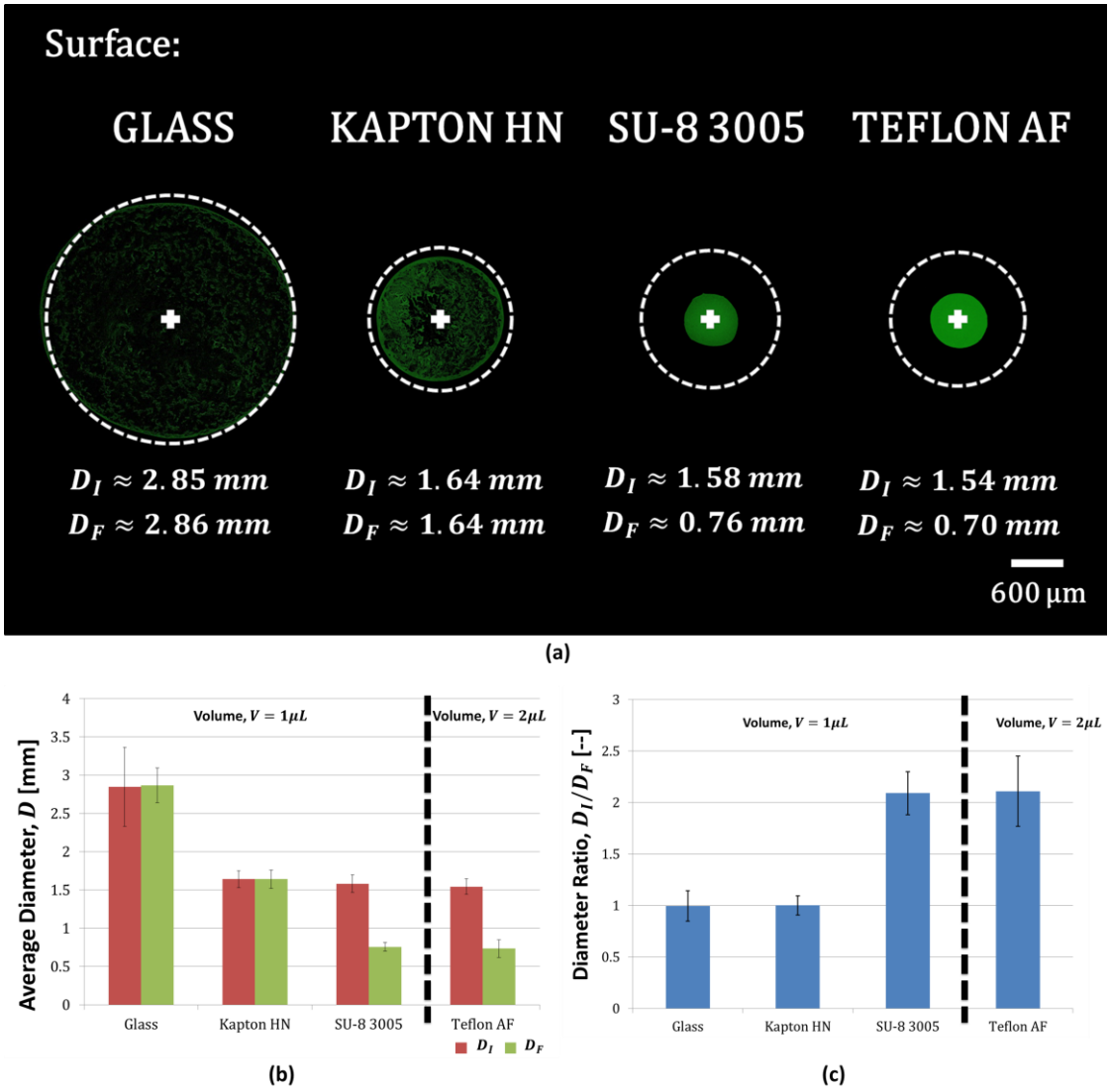

Figure 5.7: (a) Top down view of deposition profile, (b) Average Diameter (D) of colloidal droplet during desiccation, and (c) diameter ratio of initial diameter D_I to final diameter D_F on Glass, Kapton HN, SU-8 3005, and Teflon AF. The initial contact diameter of the droplet is represented by a white dashed line.

Like SU8, Teflon AF has a large receding contact angle. The resultant deposition pattern on Teflon AF appears to be smaller, more uniform, and more intense than the deposition profile observed on Glass and Kapton HN. The deposition on Teflon AF resulted in an initial contact diameter $D_I = 1.54 \pm 0.10\ mm$ and a final deposition diameter $D_F = 0.73 \pm 0.11\ mm$, and a corresponding $D_I/D_F = 2.11 \pm 0.34\ [-]$. The observed diameter reduction suggests the contact line moves in the Teflon AF case as predicted by a high receding contact angle. However, the large initial contact angle of Teflon AF did not result in a significantly smaller initial contact

diameter when compared to SU-8 3005. This is attributed to the larger (2 μL) volume used for Teflon AF depositions, while SU-8 3005 depositions used 1 μL sized volumes. If a smaller volume of fluid is used for Teflon AF, a smaller initial diameter should occur and smaller final deposition pattern may occur.

Fluorescent Images acquired via the CML (Fig. 5.7a) were analyzed via MATLAB producing quantitative data about the resultant desiccation shape, size, and intensity profile (Table 5.3).

The average spot intensity $\bar{I}$ of the resultant deposition pattern on Glass, Kapton HN, SU-8 3005, and Teflon AF are presented in Table 5.3 and Figure 5.8. As predicted, Kapton HN had a larger average intensity than Glass due to the smaller initial contact diameter. Teflon AF had a significantly larger average intensity due to the large equilibrium and receding contact angle producing a small, uniform, and intense spot. This increased intensity of the Teflon AF spots presented is also attributed to the larger volume of fluid used during desiccation resulting in more particles concentrating in the final deposition.

Table 5.3: Equilibrium contact angle θ_0, average initial diameter D_I, average final diameter D_F, diameter ratio D_I/D_F, and average intensity $\bar{I}$ of Glass, Kapton HN, SU-8 3005, and Teflon AF.

Surface		**Glass**	**Kapton HN**	**SU-8 3005**	**Teflon AF**
θ_0	[°]	23.87 ± 4.68	86.05 ± 5.01	88.68 ± 4.68	120.49 ± 5.35
D_I	$[mm]$	2.85 ± 0.52	1.64 ± 0.11	1.58 ± 0.12	1.54 ± 0.10
D_F	$[mm]$	2.86 ± 0.23	1.64 ± 0.12	0.76 ± 0.06	0.73 ± 0.11
D_I/D_F	$[--]$	0.99 ± 0.05	1.00 ± 0.09	2.09 ± 0.07	2.11 ± 0.34
$\bar{I}$	$[bit]$	3.59 ± 1.53	11.92 ± 5.74	243.42 ± 22.10	870.09 ± 195.90

The average intensity and average final diameter data was used to normalize the intensity values and the radial position given in Figure 5.9.

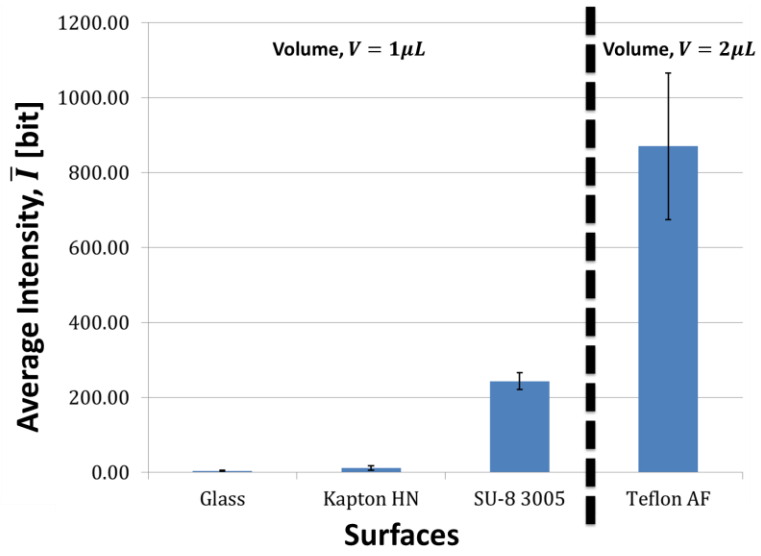

Figure 5.8: Average intensity of Glass, Kapton HN, SU-8 3005, and Teflon AF.

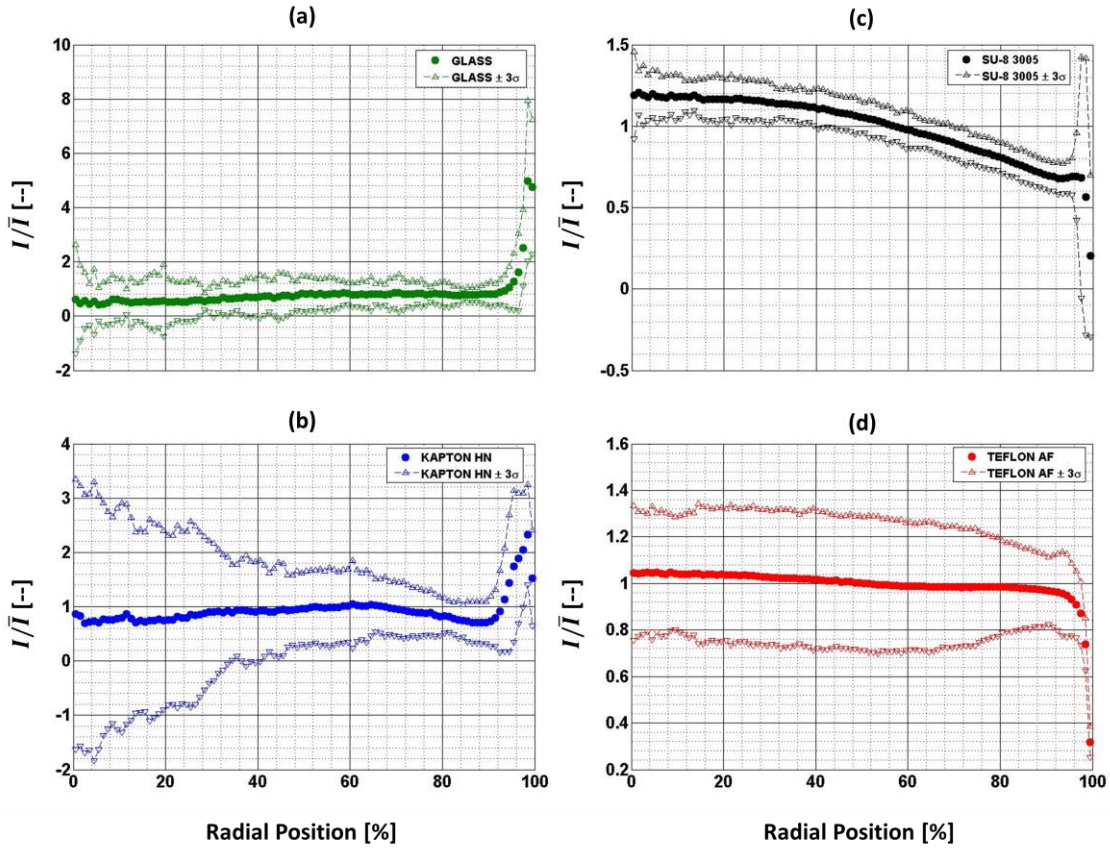

Figure 5.9: Normalized intensity $I/\bar{I}$ versus radial position of (a) Glass, (b) Kapton HN, (c) SU-8 3005, and (d) Teflon AF.

As predicted, the deposition observed on Kapton HN resembles a traditional coffee stain pattern similar to the coffee stain produced when depositing on Glass. However, the equilibrium contact angle of Kapton HN is similar to SU-8 3005 so the initial contact diameter is smaller and more intense than observed on Glass. Here, the maximum intensity ($27.78\ [bit]$) occurred at the periphery of the deposition and was 133.1 % larger than the average intensity of the spot. However, the variance in droplet intensity for Kapton HN is much greater than that of Glass. This may be attributed to surface imperfections on the Kapton HN polyimide film tape inhibiting the outward radial motion of the particles to the periphery. The imperfections on Kapton HN are varied resulting in this large variance of intensity in the center of the coffee-stain.

As predicted, the deposition pattern observed on Teflon AF was smaller, more intense, and more uniform than the pattern observed on SU-8 3005. Like SU8, the deposition pattern observed on Teflon AF exhibits evidence of a receding contact line. The final diameter of the Teflon AF deposition is 110% smaller than the initial diameter. The maximum intensity of $911.45\ [bit]$ occurred at the center of the droplet, but was only 4.8 % greater than the mean. This maximum intensity had a very slight decrease from 0 % to around 60 % of the radial position. At that point the intensity appeared to stay fairly constant up until 90 % of the radial position where the intensity drops off. The minimum intensity occurs at the periphery of the droplet with a value of $277.17\ [bit]$ that is 31.9 % of the mean intensity. The increased intensity in the deposition on Teflon is expected due to the higher equilibrium contact angle and droplet volume. Interestingly, the variance in the Teflon AF spot is greater than SU-8 3005. Additionally, Teflon AF did not produce a large variability in the intensity over the deposition profile as observed in SU-8 3005. Although there is a greater intensity at the center of the deposition on Teflon AF, it is not as significant of an increased intensity as observed for SU-8 3005.

Transient deposition was observed using a Ramé-Hart Model 250 Standard Goniometer/Tensiometer with DROPimage Advanced software to better understand the transient interface shape. Backlit images of side view interface profiles for droplets containing 1.1 μm diameter fluorescent microspheres are presented in Figure 5.10. Droplets were desiccated on Glass (Fig. 5.9-Ia-g), Kapton HN (Fig. 5.10-IIa-g), SU-8 3005 (Fig. 5.10-IIIa-g), and Teflon AF (Fig. 5.10-IVa-g). The total evaporation time was used to calculate the normalized time τ given in the side view transient interface shape profile presented in Figure 5.10.

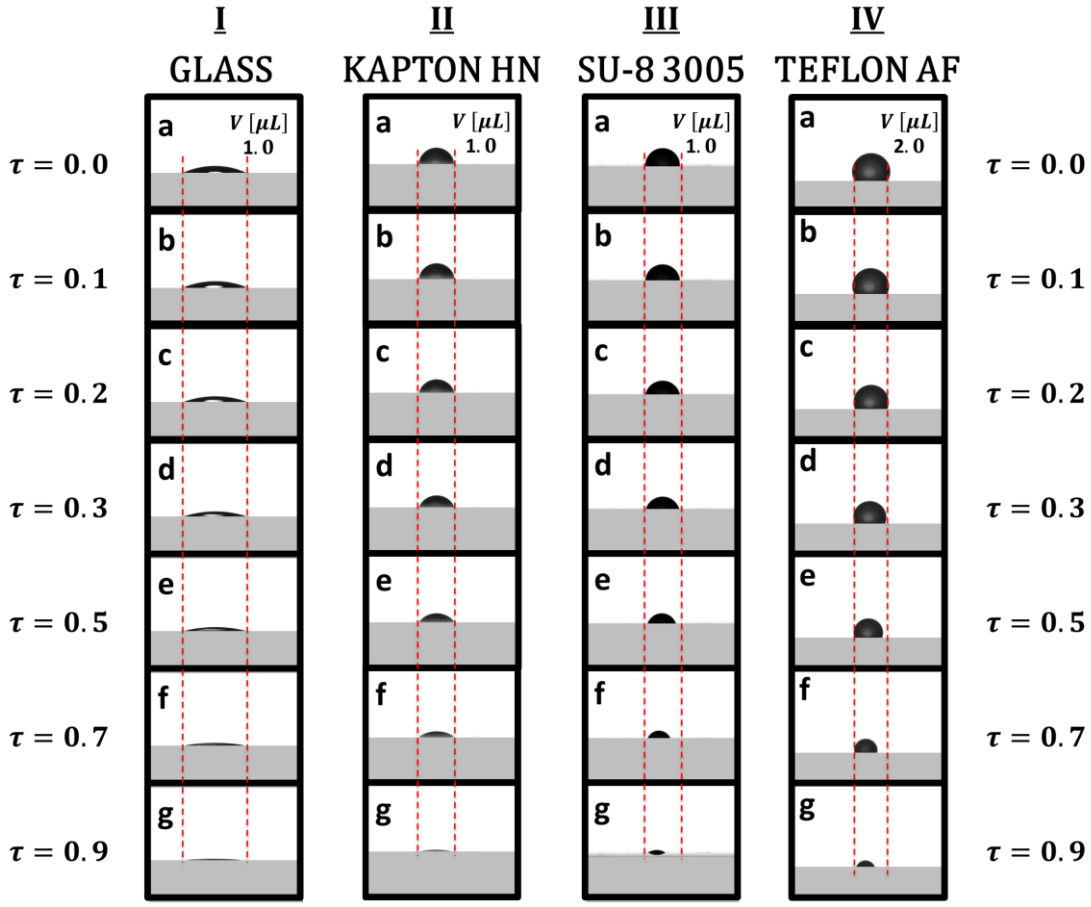

Figure 5.10: Backlit images of side view interface profiles of evaporating colloidal droplet at normalized time (a) $\tau = 0.0$, (b) $\tau = 0.1$, (c) $\tau = 0.2$, (d) $\tau = 0.3$, (e) $\tau = 0.5$, (f) $\tau = 0.7$, and (g) $\tau = 0.9$ on Glass, Kapton HN, SU-8 3005, and Teflon AF. Red dashed lines indicate initial contact diameter of the droplet.

The contact angle θ and normalized diameter D/D_0 where $D_0 = D_F$ profiles presented in Figure 5.11 were produced using a custom code in MATLAB. The total drying time was used to calculate the normalized time τ presented these graphs. The resultant deposition patterns observed in Figure 5.7a are predicted to be a function of the hysteresis, equilibrium contact angle, and receding contact angles. The equilibrium contact angle determines the initial diameter of the droplet. The hysteresis affects how close the receding contact angle is to the equilibrium contact angle. The receding contact angle affects the change in contact angle. A decrease in contact angle to a value close to the receding contact angle is required for the contact angle to recede suggesting that the contact angle of the droplet must be reduced to some value close to the receding contact angle for the resultant spot to be smaller than the original diameter.

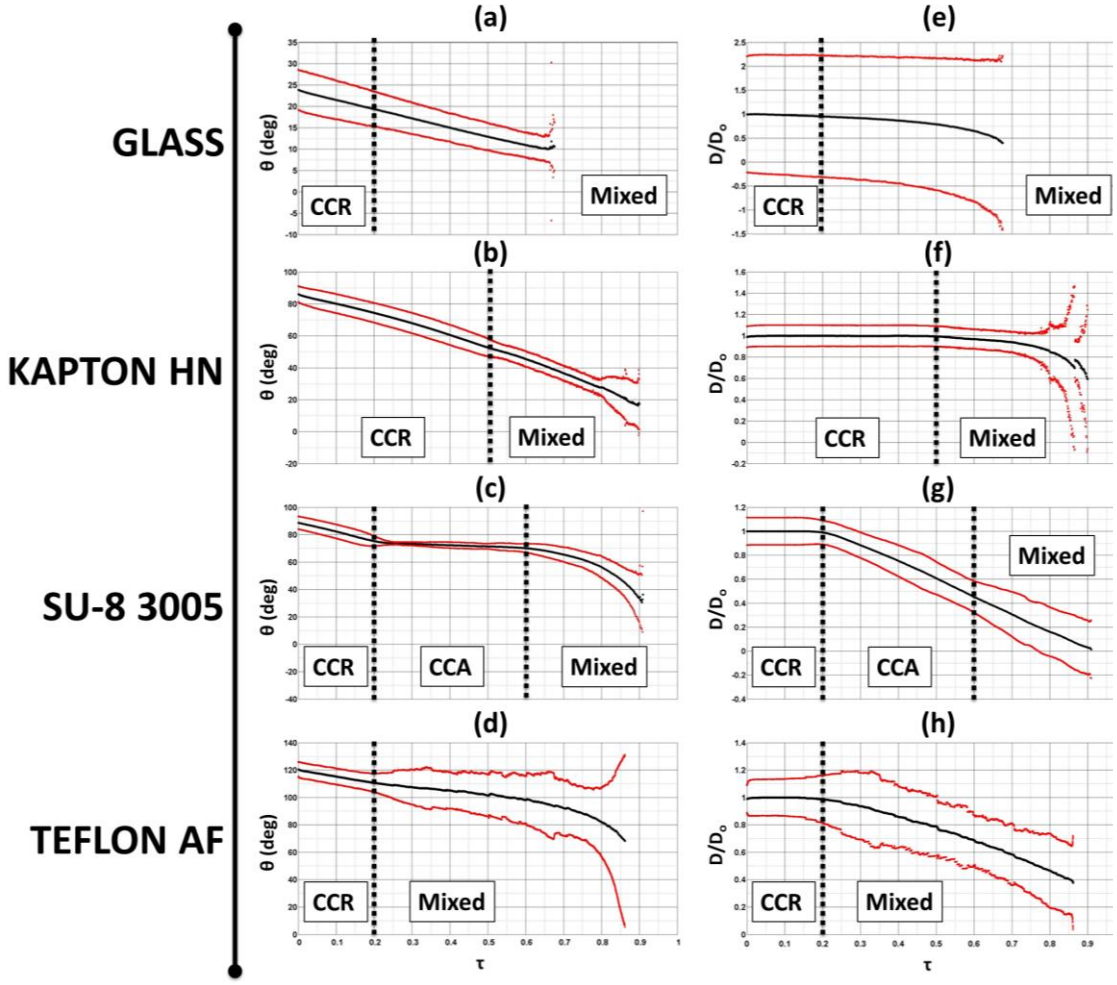

Figure 5.11: (a) Contact Angle (ϑ) and (b) normalized diameter (D/D_0) of evaporating colloidal droplet on Glass, Kapton HN, SU-8 3005, and Teflon AF as a function of normalized time (τ).

Quantitative analysis of the transient contact angle and normalized contact diameter of the droplets desiccated on Kapton HN with corresponding regimes is presented in Figure 5.11 b,f. For the droplets desiccated on Kapton HN, the desiccation process can be segmented into two observable regimes as predicted. These regimes are representative of the: (i) CCR and (ii) mixed mode regimes observed in [26,48]. From $\tau = 0.0 - 0.5$ the TCL is pinned during the CCR regime (Fig. 5.9-II a-e). As a result the contact angle decreases from $\theta_0 \approx 86°$ to $\theta \approx 53°$ while the contact diameter remains fairly constant at a $D \approx 1.65\ mm$ (Fig. 5.11 b,f). This CCR regime we observe occurs when the contact line is pinned. Reductions on the droplet volume are due to evaporative flux at the TCL resulting in a decreased contact angle over time. As the contact angle decreases more, the evaporative flux increases bringing more solute to the pinned TCL. At around

$\tau = 0.5$ the contact angle and contact diameter both decrease with time (Fig. 5.11b,f) until the droplet is so small that the software cannot observe the droplet (Fig. 5.11-IIf,g). While the Ramé-Hart DROPImage Advanced software is unable to measure contact angles below approximately 20° reliably [74], transient side view images in Figure 5.11-II a-e seems to be consistent with the CCR regime and Figure 5.11-IIf,g seems to be consistent with the mixed phase described in [26,48] where the contact angle and diameter both reduce over time. The deposition profiles presented repeatedly gave coffee-stain patterns which indicate a pinned contact line for the majority of the desiccation.

Kapton HN and Glass both transition from the CCR regime into the mixed regime, however Kapton HN takes longer to transition suggesting that the receding contact angle on Kapton HN may be less than on Glass. However, both surfaces result in similar a coffee-stain deposition pattern.

Quantitative analysis of the transient contact angle and normalized contact diameter of the droplets desiccated on Teflon AF with corresponding regimes is presented in Figure 5.11 d,h. Interestingly, for the droplets desiccated on Teflon AF, the desiccation process can be segmented into only two observable regimes similar to Glass and Kapton HN. These regimes are representative of the: (i) CCR and (ii) mixed mode regimes observed in [26,48]. From $\tau = 0.0 - 0.2$ the TCL is pinned (Fig. 5.9-IVa-c). As a result the contact angle decreases from $\theta_0 \approx 120°$ to $\theta \approx 111°$ while the contact diameter remains at a constant $D \approx 1.54$ (Fig. 5.11c,g). This CCR regime we observe occurs when the contact line is pinned and reductions on the droplet volume are due to evaporative flux at the three phase contact line resulting in a decreased contact angle. As the contact angle decreases, the force pulling in the contact line increases and eventually overcomes the surface and slips free. Teflon AF never enters a CCA regime and instead goes into the mixed regime at around $\tau = 0.2$ where both the contact angle and contact diameter decrease with time (Fig. 5.9-IVd-g). The mixed regime we observe occurs due to either the combination of the contact line slipping and the contact angle decreasing or intermittent changes between both the CCA and CCR regime (Fig. 5.11d,h). The mixed regime we observe can be split up into two different segments. From $\tau = 0.2 - 0.75$ the decrease in contact angle is approximately linear with a small slope. At $\tau > 0.75$, the slope begins to increase with time causing a more rapid decrease in contact angle. The first segment of the mixed regime may act similar to the CCA regime on SU-8 3005. During this first segment, the solute that may have deposited during the CCR regime is resuspended and swept inwards as the contact line recedes. At $\tau \approx 0.75$ the

diameter of the droplet reduces to ≈ 52.2 % of the initial diameter. The second segment of this regime looks similar to the mixed regime on SU-8 3005 and is theorized to be the section where most of the deposition occurs. The final deposition has a diameter that is ≈ 47.4 % of the initial contact diameter. This diameter reduction is observed at $\tau \approx 0.79$ and may be when the particles start to deposit. However, the deposition on Teflon AF produces a more uniform spot than SU-8 3005. This may be attributed to the regimes described above. Teflon AF reaches the receding contact angle in the CCR regime, while SU-8 3005 does not reach the receding contact angle until it is in the CCA regime. As a result there is a different evaporative regime that leads to a potentially different deposition pattern that should be studied further. as previously mentioned, future experiments can be improved with the incorporation of optically observing and tracking individual particles moving to the TCL by the use of Particle Image Velocimetry (PIV). Incorporation of PIV may better lead to understanding of the packing order at the TCL, and motion of the streamlines in the colloidal suspension during evaporation.

Teflon AF has some advantages over SU-8 3005. The evaporated colloidal droplets produce smaller, more intense, and more uniform deposition patterns. Unfortunately, in approximately 30% of the cases performed on Teflon AF, crescent shaped depositions were observed on the substrate (Fig. 5.12). This formation appears to be due to asymmetric contact line pinning. This shape could not be observed in a 2-D plane. The facility should be augmented to include overhead imaging to better describe this phenomenon.

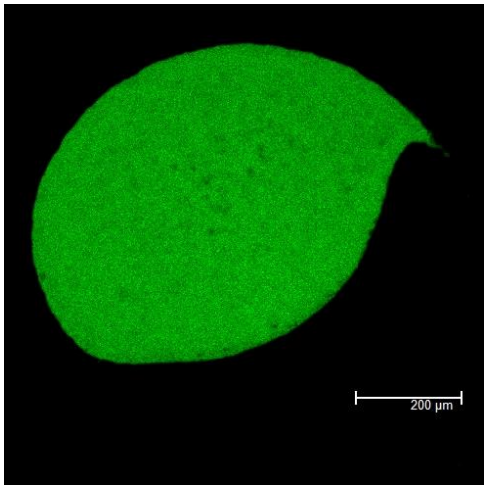

Figure 5.12: Crescent shaped deposition observed in approximately 30% of the cases performed on Teflon AF surfaces appearing to be due to asymmetric contact line pinning.

5.2 Effect of Electrode Geometry and Voltage on AC Electroweetting Assisted Colloidal Droplet Desiccation

Electrowetting on dielectric (EWOD) devices are microfluidic devices that manipulate fluid interfaces by applying electric fields [43–45,50–52,54,57–66]. General EWOD devices consist of a flat conductive electrode. The electrode is covered with electrically insulating dielectric and hydrophobic layers. The droplet placed on the EWOD device beads up on the hydrophobic surface. When a voltage is applied, the electrowetting effect will cause the droplet to spread. As long as the droplet is grounded, the application of an electric field results in an EW force on the interface that will decrease the apparent contact angle.

The insertion of a ground wire into the top of the droplet is typically used (Fig. 5.13a); however some applications make use of coplanar electrodes that do not pierce the droplet surface due to various applications (Fig. 5.13b,c). The Young-Lippmann equation is valid for the basic EWOD application where a ground wire is placed into the droplet. The capacitance per unit area is very simple for this model, however when using coplanar electrodes this value changes and the Young-Lippmann equation needs to be modified to account for this change in geometry [64–66]. Inserted ground, and a co-planar ground wire configurations were used in [43,44], but differentiation between the two cases was not presented. It seems implied that the applied voltage was the same in both cases, however the electrowetting behavior of the droplet is predicted to be dependent on electrode geometry [64–66]. The (i) orientation of the electrodes and (ii) geometry of the electrodes play an important role in how AC EW occurs and must be considered. These parameters will affect (i) the applied voltage needed for saturation to occur, (ii) the strength of the EW field, and (iii) the direction of the EW field.

Three different electrode geometries: (a) inserted ground wire, (b) simple coplanar electrode, and (c) coplanar InterDigitated Electrode (IDE) were compared for a system with a $1\ \mu L$ droplet of DI water on $3.6\ \mu m$ of SU-8 3005 (Fig. 5.13).

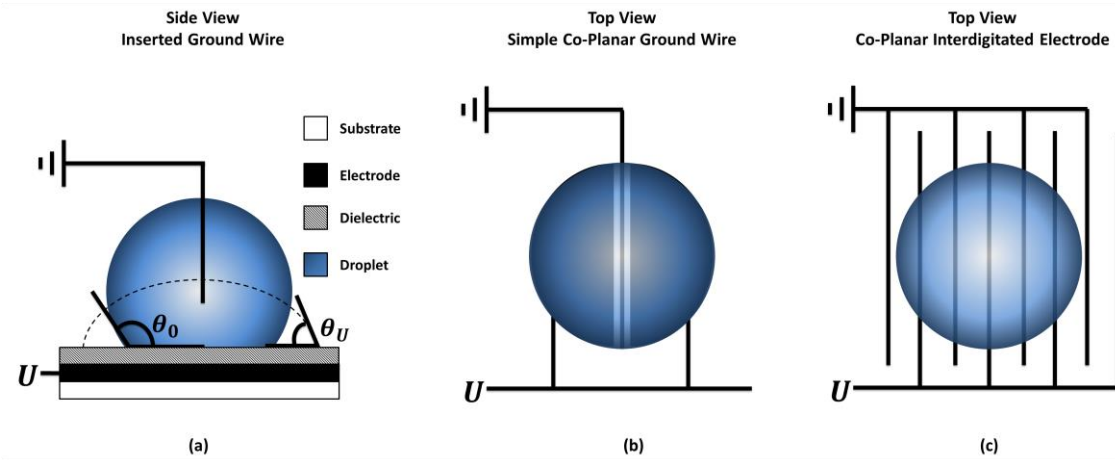

Figure 5.13: Sketch of typical electrowetting on dielectric (EWOD) setup with an (a) inserted ground wire, (b) a simple co-planar ground wire, and (c) a co-planar interdigitated electrode configuration. As a voltage is applied through the droplet the apparent contact angle changes from θ_0 to θ_U.

The Young-Lippmann equation remains the same in configuration (a) (Eq. 5.1):

$$cos\theta_U = cos\theta_0 + \eta\,, \tag{5.1}$$

where θ_U represents the voltage-dependent apparent contact angle in the system, $\theta_0 = 88.68°$ represents the apparent contact angle of the system at zero voltage, and η is the dimensionless electrowetting number. The elctrowetting number is a ratio of electrical energy at the solid-liquid interface to the interfacial energy at the liquid-medium interface (Eq. 5.2):

$$\eta = \frac{cU^2}{2\gamma_{LV}}\,, \tag{5.2}$$

where $\gamma_{LV} = 0.072\ N/m$ represents the surface tension of water at $25\ °C$, U represents the voltage, and c is the capacitance per unit area between the fluid droplet and the electrode for a typical inserted ground wire setup given by (Eq. 5.3):

$$c = \frac{\varepsilon_r \varepsilon_0}{d}\,, \tag{5.3}$$

where $\varepsilon_r = 3.28$ is the dielectric constant of the insulator (SU-8 3005), $\varepsilon_0 = 8.854\ x\ 10^{-12}\ F/m$ represents vacuum permittivity, and $d = 3.6\ \mu m$ is the thickness of the insulating layer.

The Young-Lippmann equation was modified to incorporate the change in capacitance per unit area of the simple coplanar electrode (Eq. 5.4):

$$cos\theta_U = \frac{C_1 U^2}{2\gamma_{LV}} + cos\theta_0\ , \tag{5.4}$$

where C_1 is the capacitance per unit area of the simple coplanar electrode (Eq. 5.5):

$$C_1 = \frac{\varepsilon_r \varepsilon_0 A_{e1} A_{g1}}{d(A_{e1} A_{g1}) A_D}\ , \tag{5.5}$$

where A_{e1} , A_{g1} , and A_D are the electrode area, ground wire area, and total droplet area for the simple coplanar electrode configuration, respectively. The droplet was assumed to be centered perfectly on the electrode.

The Young-Lippmann equation was again modified to incorporate the change in capacitance per unit area of the coplanar IDE (Eq. 5.6):

$$cos\theta_U = \frac{C_2 U^2}{2\gamma_{LV}} + cos\theta_0\ , \tag{5.6}$$

where C_2 is the capacitance per unit area of the coplanar IDE (Eq. 5.7):

$$C_2 = \frac{C_{2+} + C_{2-}}{2}\ , \tag{5.7}$$

where C_{2+} and C_{2-} are the capacitance per unit area of the system when the droplet is centered between two electrodes (+) and when the droplet is centered on an electrode (-), respectively for a coplanar IDE configuration. Any variation between these two scenarios will change the capacitance per unit area that is used in the EW equation. For a rough estimate, the average between these two extremes was used. Equation 5.7 expands to Equation 5.8:

$$C_2 = \frac{\left(\frac{\varepsilon_r \varepsilon_0 A_{e2+} A_{g2+}}{d(A_{e2+}+A_{g2+})A_D} + \frac{\varepsilon_r \varepsilon_0 A_{e2-} A_{g2-}}{d(A_{e2-}-A_{g2-})A_D}\right)}{2}, \tag{5.7}$$

where A_{e2+} , A_{g2+} , A_{e2-} , and A_{g2-} are the electrode area and ground wire area, when the droplet is centered between two electrodes (+) and when the droplet is centered on an electrode (-), respectively for a coplanar IDE configuration.

The theoretical models of both coplanar electrode configurations were compared to the inserted ground wire configuration and the experimental data was plotted on top of these curves using MATLAB (Fig. 5.14).

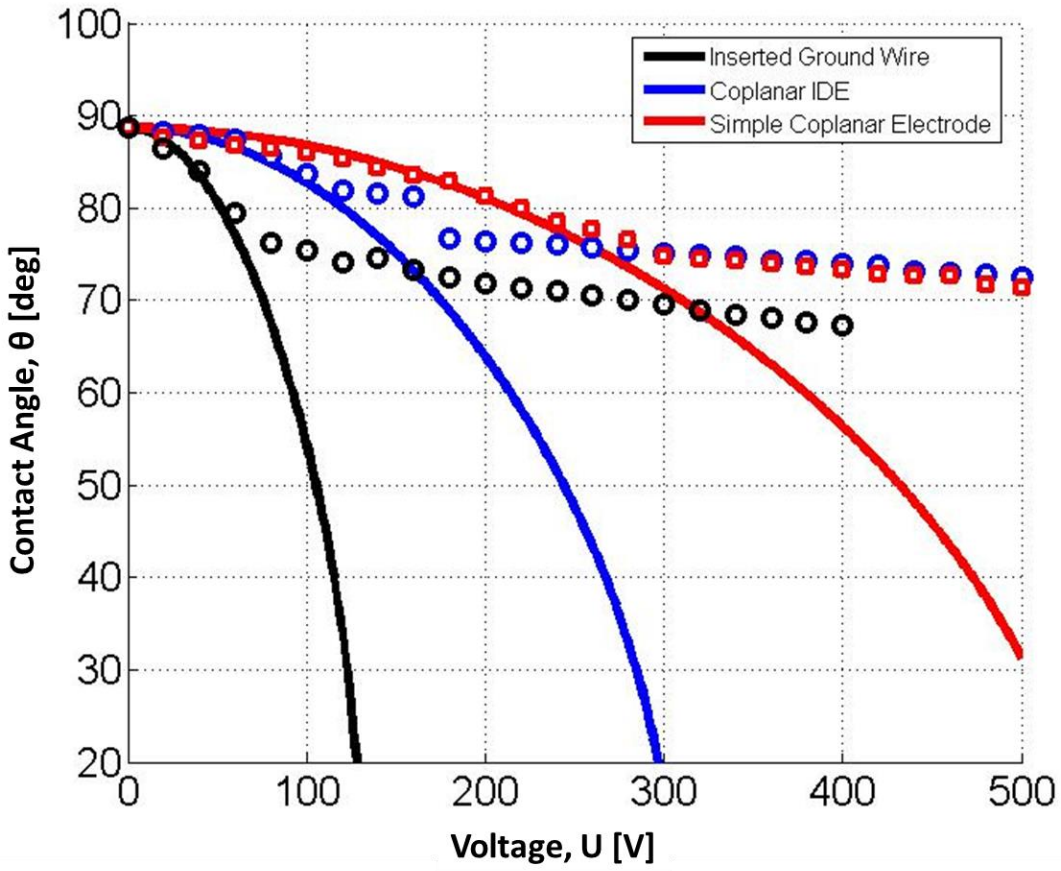

Figure 5.14: Theoretical curves (solid lines) and experimental data (points) for three EWOD configurations: (a) inserted ground wire, (b) a simple co-planar ground wire, and (c) a co-planar interdigitated electrode configuration. As a voltage is applied through the droplet the apparent contact angle changes, and eventually the droplet hits a saturation voltage where the EW force cannot change the contact angle any more.

The electrode width and spacing were kept constant at 80 μm and 40 μm, respectively. The experimental data followed the theoretical trends. Increasing the capacitance per unit area increased the actuation voltage required to achieve a particular reduction in the apparent contact angle. However improvements on the model can be made to better represent the location of the droplet, and the orientation of the electrode. For the coplanar electrodes, the voltage needs to pass through the dielectric layer twice which results in the swept out theoretical curve indicating a need for a higher voltage to reach saturation (i.e. when the data does not follow the Y-L equation).The inserted ground wire configuration appears to saturate at $\sim 80\ V$ reaching a $\theta_U \approx 76.2°$. The coplanar IDE configuration appears to initially saturate at $\sim 120\ V$ reaching a $\theta_U \approx 81.8°$. However, the contact angle drops again at $\sim 180\ V$ reaching a $\theta_U \approx 76.7°$ which is more reasonable for a saturation contact angle and saturation voltage. The droplet seemed to stick at one electrode and then slip free allowing the droplet to fully saturate. The simple coplanar electrode configuration appears to saturate at $\sim 280\ V$ reaching a $\theta_U \approx 76.5°$. The orientation and geometry of the electrodes play an important role in how AC EW occurs and must be considered. Modifying these parameters changes how the Young-Lippmann equation should be derived and how EW occurs.

In an attempt to replicate the work completed in [43,44], a $V_{rms} = 160\ V$ sine wave at 1 kHz was applied to a 1 μL colloidal droplet containing 1.1 μm diameter fluorescent carboxylate-modified polystyrene microspheres in an inserted ground wire EWOD configuration. The voltage applied was well above the saturation voltage for this configuration, and according to [43,44] a smaller more uniform deposition should have resulted due to (i) prevention of pinning at the TCL and (ii) internal flow fields produced by the AC that counteracted the evaporative flux [44]. However, in these preliminary results, this smaller uniform deposition did not occur (Fig. 5.15). In fact, a much larger deposition occurred with a resultant diameter of $\sim 1.77\ mm$. This droplet appeared to potentially have a net electrophoretic force pull the particles down to the surface resulting in a more uniform spread out deposition as observed in Figure 5.15.

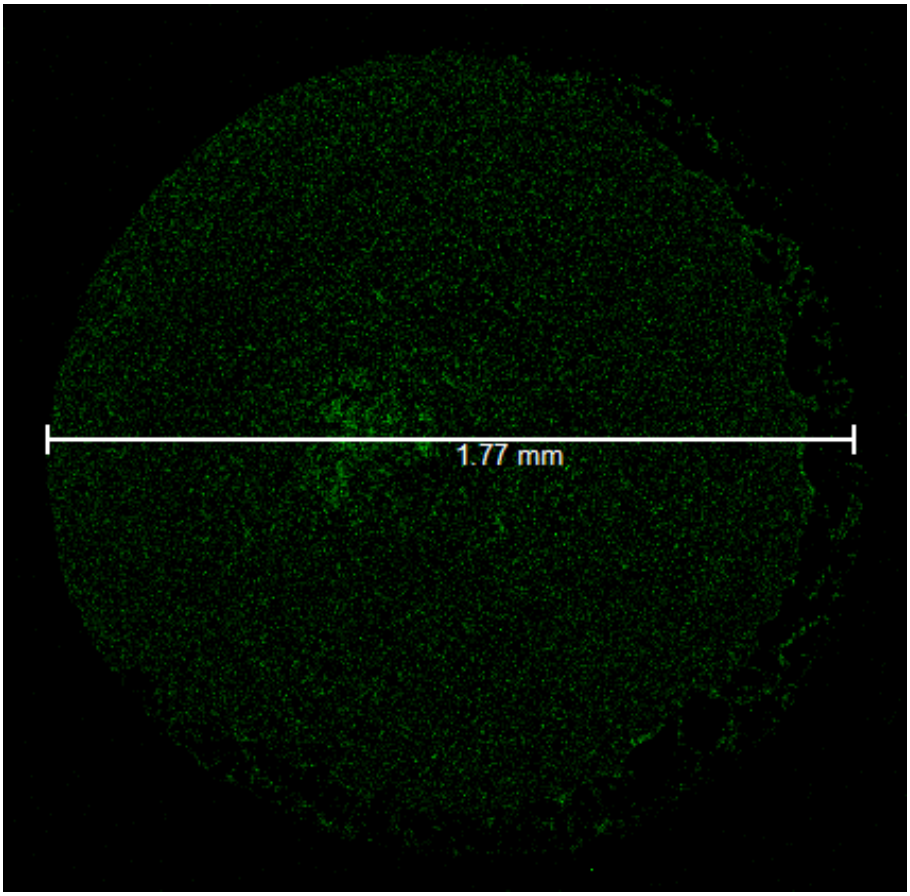

Figure 5.15: Top down view of deposition profile left during colloidal droplet desiccation on SU-8 3005 under the influence of an AC EW force with an applied voltage of $V_{rms} = 160\ V$ at 1 kHz frequency.

Here, the deposition has a fairly large diameter with a small overall average intensity ($\bar{I} = 10.27\ [bit]$) and more evenly distributed particles (Fig. 5.16) when compared to the unactuated case on SU-8 3005. The intensity appears to peak at $\sim$20 % of the radial position which can be visually seen by the brighter intensity observed toward the center of the droplet in Figure 5.15. The remainder of the deposition profile appears to be more uniform with a decrease in the intensity from 90 to 100 % of the radial position. This is attributed to the lack or particles on the right side of the deposition that may have occurred when the contact line slipped inward. While further study is required to understand this effect, the final distribution pattern is similar to that seen in the DC actuation case where electrophoretic effects dominate [45]. In order to understand this phenomenon more, the interplay between the advective and electrophoretic forces need to be observed and quantified. This preliminary work warrants further investigation into this phenomenon.

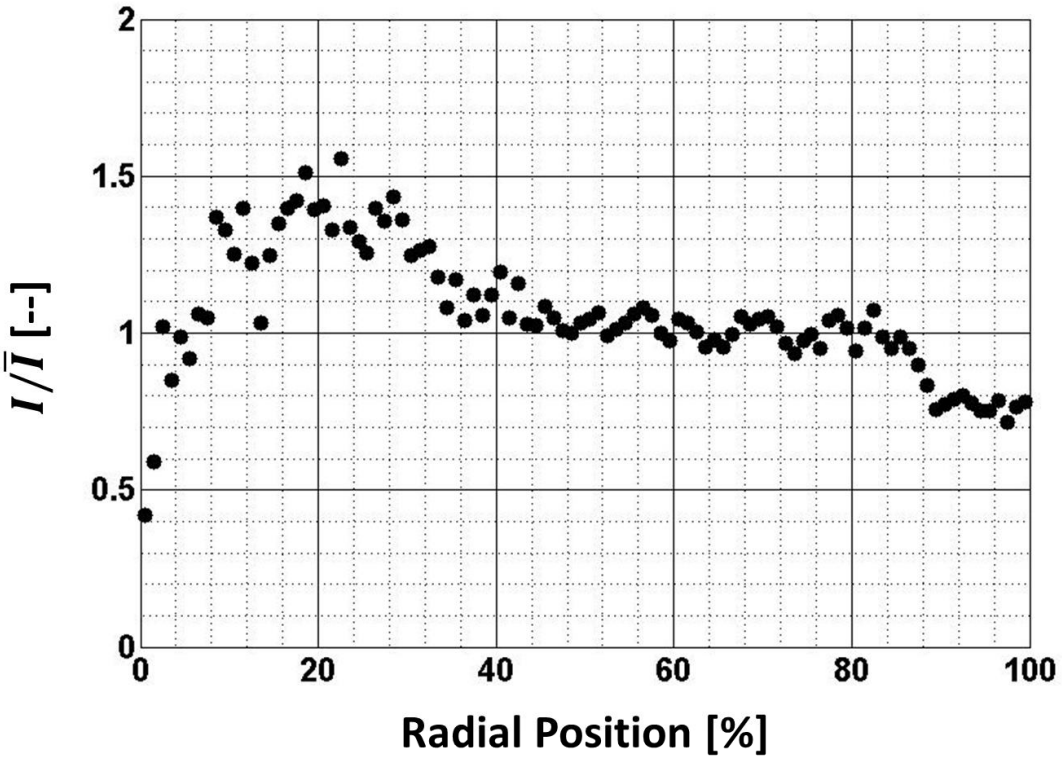

Figure 5.16: Normalized intensity $I/\bar{I}$ versus radial position of a deposition profile left during colloidal droplet desiccation on SU-8 3005 under the influence of an AC EW force with an applied voltage of $V_{rms} = 160\,V$ at 1 kHz frequency.

6.0 CONCLUSIONS

In the cases observed (Glass, Kapton HN, SU-8 3005, and Teflon AF), the resultant deposition pattern appears to be a function of: (i) the equilibrium contact angle and (ii) receding contact angle. The equilibrium contact angle determines the initial contact diameter of the aqueous colloidal suspension. A decrease in the contact angle must occur for the contact line to move. However, the contact angle of the droplet must be reduced to some value close to the receding contact angle for the contact line to move (i.e. unpin). If the receding contact angle is very large (i.e. small hysteresis) the contact line has more of an ability to move. Therefore, the resultant spot after total evaporation is observed to be smaller than the original diameter when depositing a fluid on a substrate with a large receding contact angle.

For all cases observed, the sessile droplet started in the CCR region. In the CCR region, the CR stays the same while the CA decreases. For Glass and Kapton HN, the receding contact angle was too low to even be measured accurately (i.e. $< 20°$). The low receding contact angle (i.e. large hysteresis) resulted in the contact line remaining pinned for the majority of the process. Therefore, most of the solute is deposited at the periphery. Deposition of the solute at the periphery decreases the mobility of the contact line more by acting like a wedge. Since the contact angle continues to decrease, the height at the edge of the droplet is further reduced. This increases the evaporative flux at the contact line, which brings more solute to the edge of the droplet. However, Kapton HN has an equilibrium contact angle that is much larger than that of Glass resulting in a smaller deposition profile with a more intense thick coffee stain pattern. When picking a substrate where a coffee stain deposition is preferred, the size of the deposition needed for the particular application can be predetermined based on the initial contact angle, and volume of the droplet.

Since SU-8 3005 and Teflon AF had larger receding CAs (i.e. smaller hysteresis) it makes them more likely to have a moving contact line. When the contact line recedes early in the process, suppression of the coffee stain is more likely. An at this point a large amount of the solute from the dispersed phase is not built up at the TCL. The moving contact line resuspends the solute and most of the deposition is observed at the end of the process after the contact line has receded to the final deposition diameter. Therefore, when depositing a fluid on a substrate with a large

receding contact angle and a small hysteresis the resultant spot after total evaporation is observed to be smaller than the original diameter given by the equilibrium contact angle.

However, SU-8 3005 and Teflon AF move into different regimes throughout the evaporation process. SU-8 3005 moves from the CCR regime to the CCA regime when the CA reaches approximately 72° at $\tau = 0.2$. This contact angle is approximately 6° larger than the receding CA. The CL slips and recedes inward from $\tau = 0.2 - 0.6$ until SU-8 3005 hits the mixed regime where the CA and CL both decrease. This three region transition creates a fairly uniform spot with a larger intensity at the center and a slight decrease in intensity towards the edge of the droplet where the intensity drops off. It was theorized that the particles deposit onto the substrate at some point during the mixed regime. Once the droplet reaches the final deposition diameter, solute starts to deposit. However, the contact angle and contact diameter continue to decrease. As the diameter reduces, more particles continue to deposit onto the surface while the contact line recedes inwards. The result is a greater amount of solute built up at the center than the edge of the resultant deposition. A larger overall intensity at the center of the deposition is observed. The larger deposition at the center may be attributed to more time to deposit in the center of the droplet or the Marangoni flow resuspending particles and bringing them to the center of the droplet to pack there. There are many forces at play when this contact line is pulling inwards and the small volume of fluid makes it difficult to observe what occurs during this regime. To understand how these particles deposit at this regime, a different method of transient observations that can individually resolve each particle is necessary for future experiments.

Teflon AF moves directly from the CCR regime to the mixed regime similar to Glass and Kapton HN. This two regime transition creates a more uniform deposition that is more evenly distributed throughout the surface of the spot than the spot created on SU-8 3005. The intensity of this spot also drops off towards the periphery similar to SU-8 3005. However, Teflon AF moves into the mixed regime when the CA reaches approximately 111° at $\tau = 0.2$ which is approximately 1° smaller than the receding CA. The mixed regime we observe can be split up into two different segments. From $\tau = 0.2 - 0.75$ the decrease in contact angle is approximately linear with a small slope. At $\tau > 0.75$, the slope begins to increase with time causing a more rapid decrease in contact angle. The first segment of the mixed regime may act similar to the CCA regime on SU-8 3005. During this first segment, the solute that may have deposited during the CCR regime is resuspended and swept inwards as the contact line recedes. The second segment of this regime looks similar to the mixed regime on SU-8 3005. It was theorized that the second segment was

where most of the deposition occurs because the final deposition diameter occurs during this segment. However, the deposition on Teflon AF produces a more uniform spot than SU-8 3005 and may be attributed to the regimes described in the results section. Teflon AF reaches the receding contact angle in the CCR regime, while SU-8 3005 does not reach the receding contact angle until it is in the CCA regime. There is a different evaporative regime that leads to a potentially different deposition pattern that should be studied further through the incorporation of PIV.

Teflon AF has some advantages over SU-8 3005. The evaporated colloidal droplets produce smaller, more intense, and more uniform deposition patterns. Unfortunately, crescent shaped depositions were observed on the substrate for approximately 30 % of the cases performed on Teflon AF. This formation appears to be due to asymmetric contact line pinning. This shape could not be observed in a 2-D plane. The facility should be augmented to include overhead imaging to better describe this phenomenon in future work.

In the case of Glass, Kapton HN, SU-8 3005, and Teflon AF, the resultant deposition pattern appears to be a function of: (i) the equilibrium contact angle and (ii) receding contact angle. The equilibrium contact angle determines the initial diameter of the droplet. A decrease in the contact angle must occur for the contact line to move. However, the contact angle of the droplet must be reduced to some value close to the receding contact angle for the contact line to move. If the receding contact angle is very large (i.e. small hysteresis) the contact line has more of an ability to move. Therefore, the resultant spot after total evaporation is observed to be smaller than the original diameter when depositing a fluid on a substrate with a large receding contact angle and a small hysteresis.

The comparison of desiccation of colloidal suspensions on Glass, Kapton HN, SU-8 3005, Teflon AF proved that,

1. Initial contact diameter can be determined from the droplet equilibrium CA;
2. Reduction in contact diameter can be predicted from the receding CA;
3. Smaller depositions have a higher intensity; and
4. Droplets with mobile contact lines are expected to produce more uniform depositions.

Transition into a regime where the contact angle has been decreased to a value close to the receding contact angle (e.g. the CCA region) is beneficial for applications seeking to suppress the appearance of the coffee ring formation. This transition is easier for solid-liquid systems that have a smaller hysteresis and larger receding contact angle. Conversely, applications who seek to enhance the coffee stain pattern would benefit for the selection of a material that has a very large hysteresis and small receding contact angle resulting in a pinned TCL. These surfaces may move directly from the CCR region to the mixed region. Different surfaces may be more appropriate for different applications. Therefore, predicting regime transitions based off of (i) the equilibrium contact angle and (ii) receding contact angle, is an appropriate and necessary methodology for selecting surfaces for specific applications. These predictions may be reaffirmed with transient observations of the interface during deposition in order to fully understand how the final deposition pattern is formed.

Preliminary investigation into the effect of (i) electrode geometry, (ii) electrode orientation, and (iii) the effect of AC EWOD was presented. EWOD devices are microfluidic devices that manipulate fluid interfaces by applying electric field and require different surfaces for various applications. In the preliminary work presented SU-8 3005 is used as both a dielectric and hydrophobic layer. The application of the EW field results in an EW force on the interface that will decrease the apparent contact angle.

The Young-Lippmann equation is valid for the basic EWOD application where a ground wire is placed into the droplet. The capacitance per unit area is very simple for this model, however when using coplanar electrodes this value changes and the Young-Lippmann equation needs to be modified to account for this change in geometry. However in some work that has been published, both an inserted ground, and a co-planar ground wire configuration were used, but differentiation between the two cases was not presented. It seemed implied that the applied voltage was the same in both cases, however using the same applied voltage would yield very different results.

Three different electrode geometries: (a) inserted ground wire, (b) simple coplanar electrode, and (c) coplanar InterDigitated Electrode (IDE) were compared for a system with a $1\ \mu L$ droplet of DI water on $3.6\ \mu m$ of SU-8 3005 and modified Young-Lippmann equation was presented for both configuration (b) and (c). The electrode width and spacing for the coplanar configurations were kept constant at $80\ \mu m$ and $40\ \mu m$, respectively. The experimental data followed the theoretical trends, however improvements on the model can made to better represent the location of the

droplet, and the orientation of the electrode. For the coplanar electrodes, the voltage needs to pass through the dielectric layer twice which resulted in the theoretical curve sweeping out indicating a need for a higher voltage to reach saturation (i.e. when the data does not follow the Y-L equation). The orientation and geometry of the electrodes have been shown to play an important role in how AC EW occurs and must be considered. Modifying these parameters changes how the Young-Lippmann equation should be derived and how EW affects the apparent contact angle as a voltage is applied through the droplet.

Preliminary investigation into the effect of AC EW was completed at a $V_{rms} = 160\ V$ sine wave at $1\ kHz$ was applied to a $1\ \mu L$ colloidal droplet containing $1.1\ \mu m$ diameter fluorescent carboxylate-modified polystyrene microspheres in an inserted ground wire EWOD configuration. The applied voltage was well above saturation for this configuration, and according to [43,44] a smaller more uniform deposition should have resulted due to (i) prevention of pinning at the TCL and (ii) internal flow fields produced by the AC that counteracted the evaporative flux [44]. However, in these preliminary results, this smaller uniform deposition did not occur. A larger deposition occurred with a resultant diameter of $\sim 1.77\ mm$. This droplet appeared to potentially have a net electrophoretic force pull the particles down to the surface resulting in a more uniform spread out deposition. In order to understand this phenomenon more, the interplay between the advective and electrophoretic forces need to be observed and quantified. This preliminary work warrants further investigation into this phenomenon and should be studied further.

REFERENCES

[1] T. Graham, Liquid Diffusion Applied to Analysis, Philos. Trans. R. Soc. London. 151 (1861) 183–224. doi:10.1098/rstl.1861.0011.

[2] K.S. Birdi, Handbook of Surface and Colloid Chemistry, 2003.

[3] K.S. Birdi, Surface and Colloid Chemistry: Principles and Applications, 2010.

[4] P. Tabeling, Introduction to Microfluidics, 2010.

[5] P. Hänggi, F. Marchesoni, Introduction: 100 years of Brownian motion, Chaos. 15 (2005) 1–5. doi:10.1063/1.1895505.

[6] M.D. Haw, Colloidal suspensions, Brownian motion, molecular reality: a short history, J. Phys. Condens. Matter. 14 (2002) 7769–7779. doi:10.1088/0953-8984/14/33/315.

[7] R. Brown, XXVII. A brief account of microscopical observations made in the months of June, July and August 1827, on the particles contained in the pollen of plants; and on the general existence of active molecules in organic and inorganic bodies, Philos. Mag. Ser. 2. 4 (1828) 161–173. doi:10.1080/14786442808674769.

[8] P.G. De Gennes, Wetting: Statics and dynamics, Rev. Mod. Phys. 57 (1985) 827–863. doi:10.1103/RevModPhys.57.827.

[9] V. Ragoonanan, A. Aksan, Heterogeneity in desiccated solutions: implications for biostabilization., Biophys. J. 94 (2008) 2212–2227. doi:10.1529/biophysj.107.110684.

[10] A. Panacek, L. Kvitek, R. Prucek, M. Kolar, R. Vecerova, N. Pizurova, et al., Silver Colloid Nanoparticles : Synthesis , Characterization , and Their Antibacterial Activity, (2006) 16248–16253.

[11] T. Neuberger, B. Schöpf, H. Hofmann, M. Hofmann, B. Von Rechenberg, Superparamagnetic nanoparticles for biomedical applications: Possibilities and limitations of a new drug delivery system, J. Magn. Magn. Mater. 293 (2005) 483–496. doi:10.1016/j.jmmm.2005.01.064.

[12] A. Ito, M. Shinkai, H. Honda, T. Kobayashi, Medical application of functionalized magnetic nanoparticles., J. Biosci. Bioeng. 100 (2005) 1–11. doi:10.1263/jbb.100.1.

[13] A. Shimoni, S. Azoubel, S. Magdassi, Inkjet printing of flexible high-performance carbon nanotube transparent conductive films by “coffee ring effect,” Nanoscale. (2014) 1–6. doi:10.1039/c4nr02133a.

[14] V. Bromberg, S. Ma, F.D. Egitto, T.J. Singler, Highly conductive lines by plasma-induced conversion of inkjet-printed silver nitrate traces, J. Mater. Chem. C. 1 (2013) 6842. doi:10.1039/c3tc31361a.

[15] V. Bromberg, S. Ma, T.J. Singler, High-resolution inkjet printing of electrically conducting lines of silver nanoparticles by edge-enhanced twin-line deposition, Appl. Phys. Lett. 102 (2013). doi:10.1063/1.4807782.

[16] M. Layani, M. Gruchko, O. Milo, I. Balberg, D. Azulay, S. Magdassi, Transparent conductive coatings by printing coffee ring arrays obtained at room temperature, ACS Nano. 3 (2009) 3537–3542. doi:10.1021/nn901239z.

[17] O. Choi, K.K. Deng, N.J. Kim, L. Ross, R.Y. Surampalli, Z. Hu, The inhibitory effects of silver nanoparticles, silver ions, and silver chloride colloids on microbial growth, Water Res. 42 (2008) 3066–3074. doi:10.1016/j.watres.2008.02.021.

[18] G.T. Carroll, D. Wang, N.J. Turro, J.T. Koberstein, Photochemical micropatterning of carbohydrates on a surface, Langmuir. 22 (2006) 2899–2905. doi:10.1021/la0531042.

[19] C.P. Gulka, J.D. Swartz, J.R. Trantum, K.M. Davis, C.M. Peak, A.J. Denton, et al., Coffee Rings as Low-Resource Diagnostics : Detection of the Malaria Biomarker Plasmodium falciparum Histidine-Rich Protein-II Using a Surface-Coupled Ring of Ni (II) NTA Gold-Plated Polystyrene Particles, (2014).

[20] G. Bracco, B. Holst, Surface science techniques, 2013. doi:10.1007/978-3-642-34243-1.

[21] C. Neinhuis, Characterization and Distribution of Water-repellent, Self-cleaning Plant Surfaces, Ann. Bot. 79 (1997) 667–677. doi:10.1006/anbo.1997.0400.

[22] L. Feng, Y. Zhang, J. Xi, Y. Zhu, N. Wang, F. Xia, et al., Petal effect: A superhydrophobic state with high adhesive force, Langmuir. 24 (2008) 4114–4119. doi:10.1021/la703821h.

[23] B. Bhushan, Y.C. Jung, Natural and biomimetic artificial surfaces for superhydrophobicity, self-cleaning, low adhesion, and drag reduction, Prog. Mater. Sci. 56 (2011) 1–108. doi:10.1016/j.pmatsci.2010.04.003.

[24] Y. Lai, Y. Tang, J. Gong, D. Gong, L. Chi, C. Lin, et al., Transparent superhydrophobic/superhydrophilic TiO2-based coatings for self-cleaning and anti-fogging, J. Mater. Chem. (2012) 7420–7426. doi:10.1039/c2jm16298a.

[25] J. Yuan, X. Liu, O. Akbulut, J. Hu, S.L. Suib, J. Kong, et al., Superwetting nanowire membranes for selective absorption, Nat. Nanotechnol. 3 (2008) 332–336. doi:10.1038/nnano.2008.136.

[26] H.Y. Erbil, Evaporation of pure liquid sessile and spherical suspended drops: A review, Adv. Colloid Interface Sci. 170 (2012) 67–86. doi:10.1016/j.cis.2011.12.006.

[27] J. Park, J. Moon, Control of colloidal particle deposit patterns within picoliter droplets ejected by ink-jet printing, Langmuir. 22 (2006) 3506–3513. doi:10.1021/la053450j.

[28] T. Kawase, H. Sirringhaus, R.H. Friend, T. Shimoda, Inkjet printed via-hole interconnections and resistors for all-polymer transistor circuits, Adv. Mater. 13 (2001) 1601–1605. doi:10.1002/1521-4095(200111)13:21<1601::AID-ADMA1601>3.0.CO;2-X.

[29] D. Bonn, J. Eggers, J. Indekeu, J. Meunier, Wetting and spreading, Rev. Mod. Phys. 81 (2009) 739–805. doi:10.1103/RevModPhys.81.739.

[30] T. Young, An Essay on the Cohesion of Fluids, Philos. Trans. R. Soc. London. 95 (1805) 65–87. doi:10.1098/rstl.1805.0005.

[31] A. Dupré, Théorie mécanique de la chaleur, Gauthier-Villars. (1869).

[32] K. Kabza, J.E. Gestwicki, J.L. McGrath, Contact angle goniometry as a tool for surface tension measurements of solids, using zisman plot method. A physical chemistry experiment, J. Chem. Educ. 77 (2000) 63–65. doi:10.1021/ed077p63.

[33] E.B. Dussan, On the Spreading of Liquids on Solid Surfaces: Static and Dynamic Contact Lines, Annu. Rev. Fluid Mech. 11 (1979) 371–400. doi:10.1146/annurev.fl.11.010179.002103.

[34] J.T. Korhonen, T. Huhtamäki, O. Ikkala, R.H. a Ras, Reliable measurement of the receding contact angle, Langmuir. 29 (2013) 3858–3863. doi:10.1021/la400009m.

[35] M.E.R. SHANAHAN, EFFECTS OF SURFACE FLAWS ON THE WETTABILITY OF SOLIDS, J. Adhes. Sci. Technol. 6 (1992) 489–501. doi:10.1163/156856192X00818.

[36] W. Zisman, Relation of the Equilibrium Contact Angle to Liquid and Solid Constitution, Contact Angle, Wettability, Adhes. 43 (1964) 1–51. doi:doi:10.1021/ba-1964-0043.ch001\n10.1021/ba-1964-0043.ch001.

[37] C.Y. Lee, B.J. Zhang, J. Park, K.J. Kim, Water droplet evaporation on Cu-based hydrophobic surfaces with nano- and micro-structures, Int. J. Heat Mass Transf. 55 (2012) 2151–2159. doi:10.1016/j.ijheatmasstransfer.2011.12.019.

[38] V.L. Morales, J.Y. Parlange, M. Wu, F.J. Pérez-Reche, W. Zhang, W. Sang, et al., Surfactant-mediated control of colloid pattern assembly and attachment strength in evaporating droplets, Langmuir. 29 (2013) 1831–1840. doi:10.1021/la304685b.

[39] H. Hu, R.G. Larson, Marangoni effect reverses coffee-ring depositions, J. Phys. Chem. B. 110 (2006) 7090–7094. doi:10.1021/jp0609232.

[40] B.M. Weon, J.H. Je, Fingering inside the coffee ring, Phys. Rev. E - Stat. Nonlinear, Soft Matter Phys. 87 (2013) 1–6. doi:10.1103/PhysRevE.87.013003.

[41] L. Cui, J. Zhang, X. Zhang, Y. Li, Z. Wang, H. Gao, et al., Avoiding coffee ring structure based on hydrophobic silicon pillar arrays during single-drop evaporation, Soft Matter. 8 (2012) 10448. doi:10.1039/c2sm26271a.

[42] P.J. Yunker, T. Still, M. a Lohr, a G. Yodh, Suppression of the coffee-ring effect by shape-dependent capillary interactions., Nature. 476 (2011) 308–311. doi:10.1038/nature10344.

[43] D. Mampallil, H.B. Eral, D. van den Ende, F. Mugele, Control of evaporating complex fluids through electrowetting, Soft Matter. 8 (2012) 10614. doi:10.1039/c2sm26103k.

[44] H.B. Eral, D.M. Augustine, M.H.G. Duits, F. Mugele, Suppressing the coffee stain effect: how to control colloidal self-assembly in evaporating drops using electrowetting, Soft Matter. 7 (2011) 4954. doi:10.1039/c1sm05183k.

[45] D. Orejon, K. Sefiane, M.E.R. Shanahan, Evaporation of nanofluid droplets with applied DC potential, J. Colloid Interface Sci. 407 (2013) 29–38. doi:10.1016/j.jcis.2013.05.079.

[46] T. Tsujioka, Metal-vapor deposition modulation on polymer surfaces prepared by the coffee-ring effect, Soft Matter. 9 (2013) 5681. doi:10.1039/c3sm00113j.

[47] R. Gebhardt, J.-M. Teulon, J.-L. Pellequer, M. Burghammer, J.-P. Colletier, C. Riekel, Virus particle assembly into crystalline domains enabled by the coffee ring effect., Soft Matter. 10 (2014) 5458–62. doi:10.1039/c4sm00414k.

[48] B.J. Zhang, J. Park, K.J. Kim, H. Yoon, Biologically inspired tunable hydrophilic/hydrophobic surfaces: a copper oxide self-assembly multitier approach, Bioinspir. Biomim. 7 (2012) 036011. doi:10.1088/1748-3182/7/3/036011.

[49] L.F. Pease, D.H. Tsai, J.L. Hertz, R. a. Zangmeister, M.R. Zachariah, M.J. Tarlov, Packing and size determination of colloidal nanoclusters, Langmuir. 26 (2010) 11384–11390. doi:10.1021/la100839t.

[50] R.D. Deegan, O. Bakajin, T.F. Dupont, G. Huber, S.R. Nagel, T. a Witten, Capillary flow as the cause of ring stains from dried liquid drops, Nature. 389 (1997) 827–829. doi:10.1038/39827.

[51] R. Deegan, Pattern formation in drying drops, Phys. Rev. E. 61 (2000) 475–485. doi:10.1103/PhysRevE.61.475.

[52] R.D. Deegan, O. Bakajin, T.F. Dupont, G. Huber, S.R. Nagel, T. a. Witten, Contact line deposits in an evaporating drop, Phys. Rev. E - Stat. Physics, Plasmas, Fluids, Relat. Interdiscip. Top. 62 (2000) 756–765. doi:10.1103/PhysRevE.62.756.

[53] K. Sefiane, Patterns from drying drops, Adv. Colloid Interface Sci. 206 (2014) 372–381. doi:10.1016/j.cis.2013.05.002.

[54] J.-H. Kim, S. Il Ahn, J.H. Kim, W.-C. Zin, Evaporation of water droplets on polymer surfaces., Langmuir. 23 (2007) 6163–6169. doi:10.1021/la0636309.

[55] D.R. Adams, M. Toner, R. Langer, Microflow and crack formation patterns in drying sessile droplets of liposomes suspended in trehalose solutions, Langmuir. 24 (2008) 7688–7697. doi:10.1021/la703835w.

[56] S. Das, P.R. Waghmare, M. Fan, N.S.K. Gunda, S.S. Roy, S.K. Mitra, Dynamics of liquid droplets in an evaporating drop: liquid droplet “coffee stain” effect, RSC Adv. 2 (2012) 8390. doi:10.1039/c2ra20743e.

[57] F. Mugele, Fundamental challenges in electrowetting: from equilibrium shapes to contact angle saturation and drop dynamics, Soft Matter. 5 (2009) 3377. doi:10.1039/b904493k.

[58] W.C. Nelson, C.-J. “Cj” Kim, Droplet Actuation by Electrowetting-on-Dielectric (EWOD): A Review, J. Adhes. Sci. Technol. ahead-of-p (2012) 1–25. doi:10.1163/156856111X599562.

[59] S.K. Cho, H. Moon, C.J. Kim, Creating, transporting, cutting, and merging liquid droplets by electrowetting-based actuation for digital microfluidic circuits, J. Microelectromechanical Syst. 12 (2003) 70–80. doi:10.1109/JMEMS.2002.807467.

[60] D. Mampallil, D. Tiwari, D. van den Ende, F. Mugele, Sample preconcentration inside sessile droplets using electrowetting, Biomicrofluidics. 7 (2013). doi:10.1063/1.4815931.

[61] T.B. Jones, On the relationship of dielectrophoresis and electrowetting, Langmuir. 18 (2002) 4437–4443. doi:10.1021/la025616b.

[62] K.H. Kang, How electrostatic fields change contact angle in electrowetting, Langmuir. 18 (2002) 10318–10322. doi:10.1021/la0263615.

[63] M.J. Schertzer, S.I. Gubarenko, R. Ben-Mrad, P.E. Sullivan, An empirically validated analytical model of droplet dynamics in electrowetting on dielectric devices, Langmuir. 26 (2010) 19230–19238. doi:10.1021/la103702t.

[64] S. Kwon, L. Lee, Focal length control by microfabricated planar electrodes-based liquid lens (μPELL), 11th Int. Conf. Solid-State Sensors …. 1342 (2001) 1348– 1351. http://scholar.google.com/scholar?hl=en&btnG=Search&q=intitle:Focal+Length+Control+by+Microfabricated+Planar+Electrodes-based+Liquid+Lens+(?PELL)#0.

[65] U.-C. Yi, C.-J. Kim, Characterization of electrowetting actuation on addressable single-side coplanar electrodes, J. Micromechanics Microengineering. 16 (2006) 2053–2059. doi:10.1088/0960-1317/16/10/018.

[66] A. Vasudev, Z. Jiang, A capillary microgripper using electrowetting, Bienn. Univ. Microelectron. Symp. - Proc. (2008) 6–10. doi:10.1109/UGIM.2008.9.

[67] R.W. O’Brien, L.R. White, Electrophoretic mobility of a spherical colloidal particle, J. Chem. Soc. Faraday Trans. 2. 74 (1978) 1607. doi:10.1039/f29787401607.

[68] T. Ito, L. Sun, M. a. Bevan, R.M. Crooks, Comparison of nanoparticle size and electrophoretic mobility measurements using a carbon-nanotube-based coulter counter, dynamic light scattering, transmission electron microscopy, and phase analysis light scattering, Langmuir. 20 (2004) 6940–6945. doi:10.1021/la049524t.

[69] A. Palanisami, J.H. Miller, Simultaneous sizing and electrophoretic mobility measurement of sub-micron particles using Brownian motion, Electrophoresis. 31 (2010) 3613–3618. doi:10.1002/elps.201000291.

[70] T.-W. Chen, B.-J. Lin, E. Brunner, D. Schild, In situ background estimation in quantitative fluorescence imaging., Biophys. J. 90 (2006) 2534–2547. doi:10.1529/biophysj.105.070854.

[71] J.C. Waters, Accuracy and precision in quantitative fluorescence microscopy, J. Cell Biol. 185 (2009) 1135–1148. doi:10.1083/jcb.200903097.

[72] N. Otsu, THRESHOLD SELECTION METHOD FROM GRAY-LEVEL HISTOGRAMS, Ieee Trans. Syst. Man Cybern. 9 (1979) 62–66. <Go to ISI>://WOS:A1979GE96000010.

[73] R.B. Fair, A. Khlystov, T.D. Tailor, V. Ivanov, R.D. Evans, P.B. Griffin, et al., Chemical and biological applications of digital-microfluidic devices, Ieee Des. Test Comput. 24 (2007) 10–24. doi:10.1109/mdt.2007.8.

[74] G. Bracco, B. Holst, Surface science techniques, Springer Ser. Surf. Sci. 51 (2013). doi:10.1007/978-3-642-34243-1.

APPENDICES

Appendix A – Publications & Presentations

- 1 - Title: "Method for Characterization of Passive Mechanical Filtration of Particles in Digital Microfluidic Devices"
ASME 2014 International Mechanical Engineering Congress & Exposition (IMECE)
[Publication, Presentation]

- 2 - Title: "Electrowetting on Dielectric (EWOD) Assisted Droplet Desiccation"
ASME 2015 International Technical Conference and Exhibition on Packaging and Integration of Electronic and Photonic Microsystems & ASME 2015 13th International Conference on Nanochannels, Microchannels, and Minichannels (InterPACK2015&ICNMM2015)
[Publication]

- 3 - Title: "Transient Interface Shape and Deposition Profile Left by Desiccation of Colloidal Droplets on Multiple Surfaces"
ASME 2015 International Mechanical Engineering Congress & Exposition (IMECE)
[Publication]

- 4 - The 7th Annual Research and Creativity Symposium 2015
[Presentation]

- 5 - Title: "Effect of Polymer Layer Selection for Electrowetting Assisted Desiccation of Colloidal Droplets [in preparation]"
[Pending Publication]

Appendix B – Supplemental MATLAB Code

- Rame - Hart Import/Export Data Script -

```
%%  PETER DUNNING
%%%%%%%%%%%%%%%%%%%%%%%%%%%%%%%%%%%%%%%%%%%%%%%%%%%%%%%%%%%%%%%%%%%%%%%%%%%%
%%%%%%%%%%%%%%%%%%%%%%%%%%%%%%%%%%%%%%%%%%%%%%%%%%%%%%%%%%%%%%%%%%%%%%%%%%%%

clear all;
close all;
clc;
format compact;

%%%%%%%%%%%%%%%%%%%%%%%%%%%%%%%%%%%%%%%%%%%%%%%%%%%%%%%%%%%%%%%%%%%%%%%%%%%%
%%%%%%%%%%%%%%%%%%%%%%%%%%%%%%%%%%%%%%%%%%%%%%%%%%%%%%%%%%%%%%%%%%%%%%%%%%%%
%%  1 - Creates Matrix to be filled in with data
%%      1a - Finds directory specified

myFolder = inputdlg( ...
    'Specify directory with raw text files with no "s: ', ...
    'DATA IMPORT', [1 50]);
    %   Specify Folder Path, Use SHIFT + RIGHT-CLICK, Copy as Path,
    %   CTRL+V into the input pop up dialog box

myFolder = myFolder{1};
    %   Takes the Folder Path specified and makes it a String Variable

if ~isdir(myFolder)
  errorMessage = sprintf( ...
      'Error: The following folder does not exist:\n%s', myFolder);
  uiwait(warndlg(errorMessage));
  return;
end
    %   Error Handler that prints Error Message if the folder you
specified
    %   does not exist

%%%%%%%%%%%%%%%%%%%%%%%%%%%%%%%%%%%%%%%%%%%%%%%%%%%%%%%%%%%%%%%%%%%%%%%%%%%%
%%%%%%%%%%%%%%%%%%%%%%%%%%%%%%%%%%%%%%%%%%%%%%%%%%%%%%%%%%%%%%%%%%%%%%%%%%%%
%%      1b - Finds all .txt files in specified directory

filePattern         =   fullfile(myFolder, '*.txt');
    %   Specifies to find all *.txt files in your "myFolder"
    %   (Specified in 1a)
txtFiles            =   dir(filePattern);
    %   Structure created that has all of the text file directories
    %   that you can iterate through later on
Length_txtFiles     =   length(txtFiles);
    %   Takes the length/number of text files in the specified
    %   directory
clearvars filePattern
    %   Clears the variable filePattern (unused after this section)
```

```
%%%%%%%%%%%%%%%%%%%%%%%%%%%%%%%%%%%%%%%%%%%%%%%%%%%%%%%%%%%%%%%%%%%%%%%%%%%%
%%%%%%%%%%%%%%%%%%%%%%%%%%%%%%%%%%%%%%%%%%%%%%%%%%%%%%%%%%%%%%%%%%%%%%%%%%%%
%%      1c - For Loop: Finds the max length associated with .txt files
                %   Uses function "Matrix_Creation.m" to  do this

Number_Lengthm      =       zeros( 1 , Length_txtFiles );
    %   Created a matrix of zeros that have as many columns as number
    %   of files that we will look at
    %   This will be filled in with the max length of all the files, so
    %   we can use that length to create an overarching matrix full of
    %   NaNs that are all equal to the max length (so matrix operations
    %   are possible)

for k = 1:Length_txtFiles
    %   For Loop with a specified k length based on number of .txt
    %   files
  baseFileName      =       txtFiles(k).name;
    %   The Txt File Name
  fullFileName      =       fullfile(myFolder, baseFileName);
    %   The Folder + Txt File Name
  [ Number_length ] =       Matrix_Creation( fullFileName );
    %   Function "Matrix_Creation" will import the .txt files based on:
    %   1) filename = fullFileName
    %   2) startRow = 11 (Hardcoded into function)
    %   3) endRow = inf (Hardcoded into function)
    %   Function "Matrix_Creation" will export the Length of the
    %   Matrices needed in order to create a matrix array to import the
    %   data into

   Number_Lengthm(k) = Number_length;
    %   Fills in Matrix of lengths of data

    clearvars Number_length ...
        baseFileName fullFileName
        %   Clears vars that will be updated each loop
end

Max_length      =       max(Number_Lengthm);
    %   Max length needed to create Matrix Array of NaN values
    %   Every other variable will be based off of this
%%%%%%%%%%%%%%%%%%%%%%%%%%%%%%%%%%%%%%%%%%%%%%%%%%%%%%%%%%%%%%%%%%%%%%%%%%%%
%%%%%%%%%%%%%%%%%%%%%%%%%%%%%%%%%%%%%%%%%%%%%%%%%%%%%%%%%%%%%%%%%%%%%%%%%%%%
%%      1d - Creates max length NaN matrix for all variables
                    %   This is neccessary for matrix operations; all
                    %   of the matrices must be the same size in order
                    %   to complete operations;

V01_Number_m        =       NaN( Max_length , Length_txtFiles );
V02_Time_m          =       NaN( Max_length , Length_txtFiles );
V03_ThetaL_m        =       NaN( Max_length , Length_txtFiles );
V04_ThetaR_m        =       NaN( Max_length , Length_txtFiles );
V05_ThetaMean_m     =       NaN( Max_length , Length_txtFiles );
V06_ThetaDev_m      =       NaN( Max_length , Length_txtFiles );
V07_Height_m        =       NaN( Max_length , Length_txtFiles );
```

```
V08_Width_m          =       NaN( Max_length , Length_txtFiles );
V09_Area_m           =       NaN( Max_length , Length_txtFiles );
V10_Volume_m         =       NaN( Max_length , Length_txtFiles );
    %   Creates a NaN Matrix for all of the Variables

%%%%%%%%%%%%%%%%%%%%%%%%%%%%%%%%%%%%%%%%%%%%%%%%%%%%%%%%%%%%%%%%%%%%%%%%%%%%%%%
%%%%%%%%%%%%%%%%%%%%%%%%%%%%%%%%%%%%%%%%%%%%%%%%%%%%%%%%%%%%%%%%%%%%%%%%%%%%%%%
%%  2 - Imports all the data from the raw .txt files
%%      2a - For Loop: Drops data into preallocated matrices
                    %   Uses function "importfile.m" to  do this

for k = 1:Length_txtFiles
    %   For Loop with a specified k length based on number of .txt
    %   files
  baseFileName = txtFiles(k).name;
    %   The Base File Name
  fullFileName = fullfile(myFolder, baseFileName);
    %   The Folder + Base File Name
  fprintf(1, 'Now reading %s\n', fullFileName); % Pause
    %   Prints what file it is reading & Pauses if you want
  [Number,Time,ThetaL,ThetaR,ThetaMean, ...
      ThetaDev,Height,Width,Area,Volume] = importfile(fullFileName);
    %   Function "importfile" will import the .txt files based on:
    %   1) filename = fullFileName
    %   2) startRow = 11 (Hardcoded into function)
    %   3) endRow = inf (Hardcoded into function)
    %   Function "importfile" will export the left hand variables

    %%% DATA COMPRESSION INTO PREALLOCATED CELLS %%%
    %   Will fill in matrix based on:
    %   Row - 1:# - This number is the length of the txt file (based
    %   off k) Column - k - Based off of iteration (aka File #)
    V01_Number_m(     1:Number_Lengthm(1,k), k )    =          Number;
    V02_Time_m(       1:Number_Lengthm(1,k), k )    =          Time;
    V03_ThetaL_m(     1:Number_Lengthm(1,k), k )    =          ThetaL;
    V04_ThetaR_m(     1:Number_Lengthm(1,k), k )    =          ThetaR;
    V05_ThetaMean_m(  1:Number_Lengthm(1,k), k )    =          ThetaMean;
    V06_ThetaDev_m(   1:Number_Lengthm(1,k), k )    =          ThetaDev;
    V07_Height_m(     1:Number_Lengthm(1,k), k )    =          Height;
    V08_Width_m(      1:Number_Lengthm(1,k), k )    =          Width;
    V09_Area_m(       1:Number_Lengthm(1,k), k )    =          Area;
    V10_Volume_m(     1:Number_Lengthm(1,k), k )    =          Volume;

    clearvars Number Time ThetaL ThetaR ThetaMean ...
        ThetaDev Height Width Area Volume ...
        baseFileName fullFileName
        %   Clears vars that will be updated each loop
end

%%%%%%%%%%%%%%%%%%%%%%%%%%%%%%%%%%%%%%%%%%%%%%%%%%%%%%%%%%%%%%%%%%%%%%%%%%%%%%%
%%%%%%%%%%%%%%%%%%%%%%%%%%%%%%%%%%%%%%%%%%%%%%%%%%%%%%%%%%%%%%%%%%%%%%%%%%%%%%%
%%  3 - Data Calculation/Compression
%%      3a - Finds average of all data sets (excluding NaNs)

V01_Number_m_mean       =       nanmean(    V01_Number_m,       2    );
V02_Time_m_mean         =       nanmean(    V02_Time_m,         2    );
```

```
V03_ThetaL_m_mean       =       nanmean(    V03_ThetaL_m,       2    );
V04_ThetaR_m_mean       =       nanmean(    V04_ThetaR_m,       2    );
V05_ThetaMean_m_mean    =       nanmean(    V05_ThetaMean_m,    2    );
V06_ThetaDev_m_mean     =       nanmean(    V06_ThetaDev_m,     2    );
V07_Height_m_mean       =       nanmean(    V07_Height_m,       2    );
V08_Width_m_mean        =       nanmean(    V08_Width_m,        2    );
V09_Area_m_mean         =       nanmean(    V09_Area_m,         2    );
V10_Volume_m_mean       =       nanmean(    V10_Volume_m,       2    );
    %   Creates a mean of all of the data sets; the "2" means that it
    %   is averaged across the rows as oppossed to down the columns, so
    %   this averages each time step; so the time steps have to be the
    %   same

%%%%%%%%%%%%%%%%%%%%%%%%%%%%%%%%%%%%%%%%%%%%%%%%%%%%%%%%%%%%%%%%%%%%%%%%%%%%%%%
%%%%%%%%%%%%%%%%%%%%%%%%%%%%%%%%%%%%%%%%%%%%%%%%%%%%%%%%%%%%%%%%%%%%%%%%%%%%%%%
%%      3b - Finds std dev of all data sets (excluding NaNs)

V01_Number_m_std    =       nanstd(    V01_Number_m,       0, 2    );
V02_Time_m_std      =       nanstd(    V02_Time_m,         0, 2    );
V03_ThetaL_m_std    =       nanstd(    V03_ThetaL_m,       0, 2    );
V04_ThetaR_m_std    =       nanstd(    V04_ThetaR_m,       0, 2    );
V05_ThetaMean_m_std =       nanstd(    V05_ThetaMean_m,    0, 2    );
V06_ThetaDev_m_std  =       nanstd(    V06_ThetaDev_m,     0, 2    );
V07_Height_m_std    =       nanstd(    V07_Height_m,       0, 2    );
V08_Width_m_std     =       nanstd(    V08_Width_m,        0, 2    );
V09_Area_m_std      =       nanstd(    V09_Area_m,         0, 2    );
V10_Volume_m_std    =       nanstd(    V10_Volume_m,       0, 2    );
    %   Creates a std dev of all of the data sets; the "2" means that
    %   it is completed across the rows as oppossed to down the
    %   columns, so this takes sd @ each time step; so the time steps
    %   have to be the same

%%%%%%%%%%%%%%%%%%%%%%%%%%%%%%%%%%%%%%%%%%%%%%%%%%%%%%%%%%%%%%%%%%%%%%%%%%%%%%%
%%%%%%%%%%%%%%%%%%%%%%%%%%%%%%%%%%%%%%%%%%%%%%%%%%%%%%%%%%%%%%%%%%%%%%%%%%%%%%%
%%  4 - Data Export
%%      4a - Specify directory you want to save txt files in

DIR = inputdlg( ...
    'Specify directory you want to save txt files in with no "s: ',...
    'TXT DATA EXPORT', [1 50]);
    %   Specify Folder Path, Use SHIFT + RIGHT-CLICK, Copy as Path,
    %   CTRL+V into the input pop up dialog box
DIR = DIR{1};
    %   Takes the Folder Path specified and makes it a String Variable
if ~isdir(DIR)
  errorMessage = sprintf( ...
      'Error: The following folder does not exist:\n%s', DIR);
  uiwait(warndlg(errorMessage));
  return;
end
    %   Error Handler that prints Error Message if the folder you
    %   specified does not exist

%%%%%%%%%%%%%%%%%%%%%%%%%%%%%%%%%%%%%%%%%%%%%%%%%%%%%%%%%%%%%%%%%%%%%%%%%%%%%%%
%%%%%%%%%%%%%%%%%%%%%%%%%%%%%%%%%%%%%%%%%%%%%%%%%%%%%%%%%%%%%%%%%%%%%%%%%%%%%%%
%%      4b - Saves the Matrix files of all the variables
```

```
V01 = 'V01_Number_m.txt';
V02 = 'V02_Time_m.txt';
V03 = 'V03_ThetaL_m.txt';
V04 = 'V04_ThetaR_m.txt';
V05 = 'V05_ThetaMean_m.txt';
V06 = 'V06_ThetaDev_m.txt';
V07 = 'V07_Height_m.txt';
V08 = 'V08_Width_m.txt';
V09 = 'V09_Area_m.txt';
V10 = 'V10_Volume_m.txt';
    %   Variables as string names for saving the directory path + file
name

dlmwrite(fullfile(DIR,V01),  V01_Number_m,     'delimiter',      '\t');
dlmwrite(fullfile(DIR,V02),  V02_Time_m,       'delimiter',      '\t');
dlmwrite(fullfile(DIR,V03),  V03_ThetaL_m,     'delimiter',      '\t');
dlmwrite(fullfile(DIR,V04),  V04_ThetaR_m,     'delimiter',      '\t');
dlmwrite(fullfile(DIR,V05),  V05_ThetaMean_m,  'delimiter',      '\t');
dlmwrite(fullfile(DIR,V06),  V06_ThetaDev_m,   'delimiter',      '\t');
dlmwrite(fullfile(DIR,V07),  V07_Height_m,     'delimiter',      '\t');
dlmwrite(fullfile(DIR,V08),  V08_Width_m,      'delimiter',      '\t');
dlmwrite(fullfile(DIR,V09),  V09_Area_m,       'delimiter',      '\t');
dlmwrite(fullfile(DIR,V10),  V10_Volume_m,     'delimiter',      '\t');
    %   Writes all the VariableMatrix txt Files to the full file path
    %   where fullefile = directory + file name
    %   There are tab '\t' delimited

clearvars V01 V02 V03 V04 V05 V06 V07 V08 V09 V10;
    %   Clears the variables used as names to save

%%%%%%%%%%%%%%%%%%%%%%%%%%%%%%%%%%%%%%%%%%%%%%%%%%%%%%%%%%%%%%%%%%%%%%%%%%%
%%%%%%%%%%%%%%%%%%%%%%%%%%%%%%%%%%%%%%%%%%%%%%%%%%%%%%%%%%%%%%%%%%%%%%%%%%%
%%      4c - Saves the Matrix files of all the mean variables

V01 = 'V01_Number_m_mean.txt';
V02 = 'V02_Time_m_mean.txt';
V03 = 'V03_ThetaL_m_mean.txt';
V04 = 'V04_ThetaR_m_mean.txt';
V05 = 'V05_ThetaMean_m_mean.txt';
V06 = 'V06_ThetaDev_m_mean.txt';
V07 = 'V07_Height_m_mean.txt';
V08 = 'V08_Width_m_mean.txt';
V09 = 'V09_Area_m_mean.txt';
V10 = 'V10_Volume_m_mean.txt';
    %   Variables as string names for saving the directory path + file
    %   name

dlmwrite(fullfile(DIR,V01),   V01_Number_m_mean,   'delimiter', '\t');
dlmwrite(fullfile(DIR,V02),   V02_Time_m_mean,     'delimiter', '\t');
dlmwrite(fullfile(DIR,V03),   V03_ThetaL_m_mean,   'delimiter', '\t');
dlmwrite(fullfile(DIR,V04),   V04_ThetaR_m_mean,   'delimiter', '\t');
dlmwrite(fullfile(DIR,V05),   V05_ThetaMean_m_mean,'delimiter', '\t');
dlmwrite(fullfile(DIR,V06),   V06_ThetaDev_m_mean, 'delimiter', '\t');
dlmwrite(fullfile(DIR,V07),   V07_Height_m_mean,   'delimiter', '\t');
dlmwrite(fullfile(DIR,V08),   V08_Width_m_mean,    'delimiter', '\t');
```

```
dlmwrite(fullfile(DIR,V09),   V09_Area_m_mean,     'delimiter', '\t');
dlmwrite(fullfile(DIR,V10),   V10_Volume_m_mean,   'delimiter', '\t');
    %   Writes the MeanMatrix txt files to the full file path where
    %   fullefile = directory + file name
    %   There are tab '\t' delimited

clearvars V01 V02 V03 V04 V05 V06 V07 V08 V09 V10;
    %   Clears the variables used as names to save

%%%%%%%%%%%%%%%%%%%%%%%%%%%%%%%%%%%%%%%%%%%%%%%%%%%%%%%%%%%%%%%%%%%%%%%%%%%%
%%%%%%%%%%%%%%%%%%%%%%%%%%%%%%%%%%%%%%%%%%%%%%%%%%%%%%%%%%%%%%%%%%%%%%%%%%%%
%%      4d - Saves the Matrix files of all the std dev variables

V01 = 'V01_Number_m_std.txt';
V02 = 'V02_Time_m_std.txt';
V03 = 'V03_ThetaL_m_std.txt';
V04 = 'V04_ThetaR_m_std.txt';
V05 = 'V05_ThetaMean_m_std.txt';
V06 = 'V06_ThetaDev_m_std.txt';
V07 = 'V07_Height_m_std.txt';
V08 = 'V08_Width_m_std.txt';
V09 = 'V09_Area_m_std.txt';
V10 = 'V10_Volume_m_std.txt';
    %   Variables as string names for saving the directory path + file
    %   name

dlmwrite(fullfile(DIR,V01),   V01_Number_m_std,    'delimiter', '\t');
dlmwrite(fullfile(DIR,V02),   V02_Time_m_std,      'delimiter', '\t');
dlmwrite(fullfile(DIR,V03),   V03_ThetaL_m_std,    'delimiter', '\t');
dlmwrite(fullfile(DIR,V04),   V04_ThetaR_m_std,    'delimiter', '\t');
dlmwrite(fullfile(DIR,V05),   V05_ThetaMean_m_std, 'delimiter', '\t');
dlmwrite(fullfile(DIR,V06),   V06_ThetaDev_m_std,  'delimiter', '\t');
dlmwrite(fullfile(DIR,V07),   V07_Height_m_std,    'delimiter', '\t');
dlmwrite(fullfile(DIR,V08),   V08_Width_m_std,     'delimiter', '\t');
dlmwrite(fullfile(DIR,V09),   V09_Area_m_std,      'delimiter', '\t');
dlmwrite(fullfile(DIR,V10),   V10_Volume_m_std,    'delimiter', '\t');
    %   Writes the StdDevMatrix txt files to the full file path where
    %   fullefile = directory + file name
    %   There are tab '\t' delimited

clearvars V01 V02 V03 V04 V05 V06 V07 V08 V09 V10;
clearvars DIR;
    %   Clears the variables used as names to save and the directory

%%%%%%%%%%%%%%%%%%%%%%%%%%%%%%%%%%%%%%%%%%%%%%%%%%%%%%%%%%%%%%%%%%%%%%%%%%%%
%%%%%%%%%%%%%%%%%%%%%%%%%%%%%%%%%%%%%%%%%%%%%%%%%%%%%%%%%%%%%%%%%%%%%%%%%%%%
%%  5 - Plot Generation
%%      5a - Specify directory you want to save fig/jpg files in

DIR = inputdlg( ...
    'Specify directory you want to save fig/jpg files in with no "s: ',
    'FIG/JPG DATA EXPORT', [1 50]);
    %   Specify Folder Path, Use SHIFT + RIGHT-CLICK, Copy as Path,
    %   CTRL+V into the input pop up dialog box
```

```
DIR = DIR{1};
    %   Takes the Folder Path specified and makes it a String Variable

if ~isdir(DIR)
  errorMessage = sprintf( ...
      'Error: The following folder does not exist:\n%s', DIR);
  uiwait(warndlg(errorMessage));
  return;
end
    %   Error Handler that prints Error Message if the folder you
    %   specified does not exist

%%%%%%%%%%%%%%%%%%%%%%%%%%%%%%%%%%%%%%%%%%%%%%%%%%%%%%%%%%%%%%%%%%%%%%%%%%%%%%%
%%%%%%%%%%%%%%%%%%%%%%%%%%%%%%%%%%%%%%%%%%%%%%%%%%%%%%%%%%%%%%%%%%%%%%%%%%%%%%%
%%      5b - 4 x 1 Subplot of ThetaL, ThetaR, ThetaMean, ThetaDev

X1 = V02_Time_m_mean;
YMatrix1(:,1) = V03_ThetaL_m_mean;
YMatrix1(:,2) = V03_ThetaL_m_mean + 3*(V03_ThetaL_m_std);
YMatrix1(:,3) = V03_ThetaL_m_mean - 3*(V03_ThetaL_m_std);
YMatrix2(:,1) = V04_ThetaR_m_mean;
YMatrix2(:,2) = V04_ThetaR_m_mean + 3*(V04_ThetaR_m_std);
YMatrix2(:,3) = V04_ThetaR_m_mean - 3*(V04_ThetaR_m_std);
YMatrix3(:,1) = V05_ThetaMean_m_mean;
YMatrix3(:,2) = V05_ThetaMean_m_mean + 3*(V05_ThetaMean_m_std);
YMatrix3(:,3) = V05_ThetaMean_m_mean - 3*(V05_ThetaMean_m_std);
YMatrix4(:,1) = V06_ThetaDev_m_mean;
YMatrix4(:,2) = V06_ThetaDev_m_mean + 3*(V06_ThetaDev_m_std);
YMatrix4(:,3) = V06_ThetaDev_m_mean - 3*(V06_ThetaDev_m_std);

PlotFunction1_Subplot1_CA(X1, YMatrix1, YMatrix2, ...
    YMatrix3, YMatrix4, DIR);

clearvars X1 YMatrix1 YMatrix2 YMatrix3 YMatrix4

%%%%%%%%%%%%%%%%%%%%%%%%%%%%%%%%%%%%%%%%%%%%%%%%%%%%%%%%%%%%%%%%%%%%%%%%%%%%%%%
%%%%%%%%%%%%%%%%%%%%%%%%%%%%%%%%%%%%%%%%%%%%%%%%%%%%%%%%%%%%%%%%%%%%%%%%%%%%%%%
%%      5c - 4 x 1 Subplot of Height, Width, Area, Volume

X1 = V02_Time_m_mean;
YMatrix1(:,1) = V07_Height_m_mean;
YMatrix1(:,2) = V07_Height_m_mean + 3*(V07_Height_m_std);
YMatrix1(:,3) = V07_Height_m_mean - 3*(V07_Height_m_std);
YMatrix2(:,1) = V08_Width_m_mean;
YMatrix2(:,2) = V08_Width_m_mean + 3*(V08_Width_m_std);
YMatrix2(:,3) = V08_Width_m_mean - 3*(V08_Width_m_std);
YMatrix3(:,1) = V09_Area_m_mean;
YMatrix3(:,2) = V09_Area_m_mean + 3*(V09_Area_m_std);
YMatrix3(:,3) = V09_Area_m_mean - 3*(V09_Area_m_std);
YMatrix4(:,1) = V10_Volume_m_mean;
YMatrix4(:,2) = V10_Volume_m_mean + 3*(V10_Volume_m_std);
YMatrix4(:,3) = V10_Volume_m_mean - 3*(V10_Volume_m_std);

PlotFunction2_Subplot2_Dimensions(X1, YMatrix1, YMatrix2, ...
    YMatrix3, YMatrix4, DIR);
```

```
clearvars X1 YMatrix1 YMatrix2 YMatrix3 YMatrix4

%%%%%%%%%%%%%%%%%%%%%%%%%%%%%%%%%%%%%%%%%%%%%%%%%%%%%%%%%%%%%%%%%%%%%%%%%%%%%%%
%%%%%%%%%%%%%%%%%%%%%%%%%%%%%%%%%%%%%%%%%%%%%%%%%%%%%%%%%%%%%%%%%%%%%%%%%%%%%%%
%%      5d - Plot of ThetaL

X1 = V02_Time_m_mean;
YMatrix1(:,1) = V03_ThetaL_m_mean;
YMatrix1(:,2) = V03_ThetaL_m_mean + 3*(V03_ThetaL_m_std);
YMatrix1(:,3) = V03_ThetaL_m_mean - 3*(V03_ThetaL_m_std);

PlotFunction3_CAL(X1, YMatrix1, DIR);

clearvars X1 YMatrix1

%%%%%%%%%%%%%%%%%%%%%%%%%%%%%%%%%%%%%%%%%%%%%%%%%%%%%%%%%%%%%%%%%%%%%%%%%%%%%%%
%%%%%%%%%%%%%%%%%%%%%%%%%%%%%%%%%%%%%%%%%%%%%%%%%%%%%%%%%%%%%%%%%%%%%%%%%%%%%%%
%%      5e - Plot of ThetaR

X1 = V02_Time_m_mean;
YMatrix1(:,1) = V04_ThetaR_m_mean;
YMatrix1(:,2) = V04_ThetaR_m_mean + 3*(V04_ThetaR_m_std);
YMatrix1(:,3) = V04_ThetaR_m_mean - 3*(V04_ThetaR_m_std);

PlotFunction4_CAR(X1, YMatrix1, DIR);

clearvars X1 YMatrix1

%%%%%%%%%%%%%%%%%%%%%%%%%%%%%%%%%%%%%%%%%%%%%%%%%%%%%%%%%%%%%%%%%%%%%%%%%%%%%%%
%%%%%%%%%%%%%%%%%%%%%%%%%%%%%%%%%%%%%%%%%%%%%%%%%%%%%%%%%%%%%%%%%%%%%%%%%%%%%%%
%%      5f - Plot of ThetaMean & ThetaMean Normalized

X1 = V02_Time_m_mean;
YMatrix1(:,1) = V05_ThetaMean_m_mean;
YMatrix1(:,2) = V05_ThetaMean_m_mean + 3*(V05_ThetaMean_m_std);
YMatrix1(:,3) = V05_ThetaMean_m_mean - 3*(V05_ThetaMean_m_std);

NameX1='01_X1_Theta.txt';
NameY1='01_YMatrix1_Theta.txt';

dlmwrite(fullfile(DIR,NameX1),   X1,      'delimiter',   '\t');
dlmwrite(fullfile(DIR,NameY1),   YMatrix1,  'delimiter',   '\t');

PlotFunction5_CAM(X1, YMatrix1, DIR);

% Normalize Time
X1_N = V02_Time_m_mean - min(V02_Time_m_mean(:));

NormalizedTime = 'Insert Time Here';  %Teflon
NormalizedTime = 'Insert Time Here';   %SU-8 3005
NormalizedTime = 'Insert Time Here';   %Kapton HN
NormalizedTime = 'Insert Time Here';   %Glass
```

```
X1_N = X1_N ./ NormalizedTime;

NameX1='02_X1_N_Theta.txt';
NameY1='02_YMatrix1_N_Theta.txt';

dlmwrite(fullfile(DIR,NameX1),   X1_N,      'delimiter',   '\t');
dlmwrite(fullfile(DIR,NameY1),   YMatrix1,  'delimiter',   '\t');

PlotFunction5_CAM_Normalized(X1_N, YMatrix1, DIR);

clearvars X1 X1_N YMatrix1

%%%%%%%%%%%%%%%%%%%%%%%%%%%%%%%%%%%%%%%%%%%%%%%%%%%%%%%%%%%%%%%%%%%%%%%%%%%%%%%
%%%%%%%%%%%%%%%%%%%%%%%%%%%%%%%%%%%%%%%%%%%%%%%%%%%%%%%%%%%%%%%%%%%%%%%%%%%%%%%
%%      5g - Plot of ThetaDev

X1 = V02_Time_m_mean;
YMatrix1(:,1) = V06_ThetaDev_m_mean;
YMatrix1(:,2) = V06_ThetaDev_m_mean + 3*(V06_ThetaDev_m_std);
YMatrix1(:,3) = V06_ThetaDev_m_mean - 3*(V06_ThetaDev_m_std);

PlotFunction6_CASD(X1, YMatrix1, DIR);

clearvars X1 YMatrix1

%%%%%%%%%%%%%%%%%%%%%%%%%%%%%%%%%%%%%%%%%%%%%%%%%%%%%%%%%%%%%%%%%%%%%%%%%%%%%%%
%%%%%%%%%%%%%%%%%%%%%%%%%%%%%%%%%%%%%%%%%%%%%%%%%%%%%%%%%%%%%%%%%%%%%%%%%%%%%%%
%%      5h - Plot of Height

X1 = V02_Time_m_mean;
YMatrix1(:,1) = V07_Height_m_mean;
YMatrix1(:,2) = V07_Height_m_mean + 3*(V07_Height_m_std);
YMatrix1(:,3) = V07_Height_m_mean - 3*(V07_Height_m_std);

PlotFunction7_H(X1, YMatrix1, DIR);

clearvars X1 YMatrix1

%%%%%%%%%%%%%%%%%%%%%%%%%%%%%%%%%%%%%%%%%%%%%%%%%%%%%%%%%%%%%%%%%%%%%%%%%%%%%%%
%%%%%%%%%%%%%%%%%%%%%%%%%%%%%%%%%%%%%%%%%%%%%%%%%%%%%%%%%%%%%%%%%%%%%%%%%%%%%%%
%%      5i - Plot of Width

X1 = V02_Time_m_mean;
YMatrix1(:,1) = V08_Width_m_mean;
YMatrix1(:,2) = V08_Width_m_mean + 3*(V08_Width_m_std);
YMatrix1(:,3) = V08_Width_m_mean - 3*(V08_Width_m_std);

NameX1='03_X1_Diameter.txt';
NameY1='03_YMatrix1_Diameter.txt';

dlmwrite(fullfile(DIR,NameX1),   X1,      'delimiter',   '\t');
dlmwrite(fullfile(DIR,NameY1),   YMatrix1,  'delimiter',   '\t');
```

```
PlotFunction8_D(X1, YMatrix1, DIR);

% Normalize Time
X1_N = V02_Time_m_mean - min(V02_Time_m_mean(:));

NormalizedTime = 'Insert Time Here';  %Teflon
NormalizedTime = 'Insert Time Here';   %SU-8 3005
NormalizedTime = 'Insert Time Here';   %Kapton HN
NormalizedTime = 'Insert Time Here';   %Glass

X1_N = X1_N ./ NormalizedTime;

X = min(YMatrix1(:,1));

YMatrix1_N(:,1) = YMatrix1(:,1) - X;

Z = max(YMatrix1_N(:,1));

YMatrix1_N(:,2) = YMatrix1(:,2) - (YMatrix1_N(:,1) + X);
YMatrix1_N(:,2) = YMatrix1_N(:,2) ./ Z;

YMatrix1_N(:,3) = YMatrix1_N(:,1) + X - YMatrix1(:,3);
YMatrix1_N(:,3) = YMatrix1_N(:,3) ./ Z;

YMatrix1_N(:,1) = YMatrix1_N(:,1) ./ Z;
YMatrix1_N(:,2) = YMatrix1_N(:,1) + YMatrix1_N(:,2);
YMatrix1_N(:,3) = YMatrix1_N(:,1) - YMatrix1_N(:,3);

NameX1='04_X1_N_Diameter.txt';
NameY1='04_YMatrix1_N_Diameter.txt';

dlmwrite(fullfile(DIR,NameX1),   X1_N,          'delimiter',   '\t');
dlmwrite(fullfile(DIR,NameY1),   YMatrix1_N,    'delimiter',   '\t');

PlotFunction8_D_Normalized(X1_N, YMatrix1_N, DIR);

clearvars X1 X1_N YMatrix1

%%%%%%%%%%%%%%%%%%%%%%%%%%%%%%%%%%%%%%%%%%%%%%%%%%%%%%%%%%%%%%%%%%%%%%%%%%%%%%%
%%%%%%%%%%%%%%%%%%%%%%%%%%%%%%%%%%%%%%%%%%%%%%%%%%%%%%%%%%%%%%%%%%%%%%%%%%%%%%%
%%      5j - Plot of Area

X1 = V02_Time_m_mean;
YMatrix1(:,1) = V09_Area_m_mean;
YMatrix1(:,2) = V09_Area_m_mean + 3*(V09_Area_m_std);
YMatrix1(:,3) = V09_Area_m_mean - 3*(V09_Area_m_std);

PlotFunction9_A(X1, YMatrix1, DIR);

clearvars X1 YMatrix1

%%%%%%%%%%%%%%%%%%%%%%%%%%%%%%%%%%%%%%%%%%%%%%%%%%%%%%%%%%%%%%%%%%%%%%%%%%%%%%%
```

```
%%%%%%%%%%%%%%%%%%%%%%%%%%%%%%%%%%%%%%%%%%%%%%%%%%%%%%%%%%%%%%%%%%%%%%%%%%%%
%%      5k - Plot of Volume

X1 = V02_Time_m_mean;
YMatrix1(:,1) = V10_Volume_m_mean;
YMatrix1(:,2) = V10_Volume_m_mean + 3*(V10_Volume_m_std);
YMatrix1(:,3) = V10_Volume_m_mean - 3*(V10_Volume_m_std);

PlotFunction10_V(X1, YMatrix1, DIR);

clearvars X1 YMatrix1

%%%%%%%%%%%%%%%%%%%%%%%%%%%%%%%%%%%%%%%%%%%%%%%%%%%%%%%%%%%%%%%%%%%%%%%%%%%%
%%%%%%%%%%%%%%%%%%%%%%%%%%%%%%%%%%%%%%%%%%%%%%%%%%%%%%%%%%%%%%%%%%%%%%%%%%%%
```

- Matrix Creation Function -

```
function [ Number_length ] = Matrix_Creation( filename )

%% Initialize variables.
delimiter = '\t';
if nargin<=2
%     USE FOR OUR R-H SYSTEM
    startRow = 9;
% %     USE FOR OLD RH SYSTEM
%     startRow = 11;
    endRow = inf;
end

%% Read columns of data as strings:
formatSpec = '%*s%f%f%f%f%f%f%f%f%f%*s%[^\n\r]';

%% Open the text file.
fileID = fopen(filename,'r');

%% Read columns of data according to format string.
textscan(fileID, '%[^\n\r]', startRow-1, 'ReturnOnError', false);
dataArray = textscan(fileID, formatSpec, 'Delimiter', ...
    delimiter, 'ReturnOnError', false);

%% Close the text file.
fclose(fileID);

%% Allocate imported array to column variable names
Number = cell2mat(dataArray(:, 1));

Number_size = size( Number );
    %   Matrix of n x m Size of sub-array in cell array
Number_length = Number_size(1 , 1);
    %   Length of sub-array in cell array
    %   Will be put in matrix & the max length will be found

end
```

- Import File Function -

```
function [Number,Time,ThetaL,ThetaR,ThetaMean, ...
    ThetaDev,Height,Width,Area,Volume] = importfile(filename)

%% Initialize variables.
delimiter = '\t';
if nargin<=2
%     USE FOR OUR R-H SYSTEM
    startRow = 9;
% %     USE FOR OLD R-H SYSTEM
%     startRow = 11;
    endRow = inf;
end

%% Read columns of data as strings:
formatSpec = '%*s%f%f%f%f%f%f%f%f%f%*s%[^\n\r]';
%% Open the text file.
fileID = fopen(filename,'r');
%% Read columns of data according to format string.
textscan(fileID, '%[^\n\r]', startRow-1, 'ReturnOnError', false);
dataArray = textscan(fileID, formatSpec, 'Delimiter', ...
    delimiter, 'ReturnOnError', false);
%% Close the text file.
fclose(fileID);

%% Allocate imported array to column variable names
% %   USE FOR OLD RH SYSTEM
% Number = dataArray{:, 1};
% Time = dataArray{:, 2};
% ThetaL = dataArray{:, 4};
% ThetaR = dataArray{:, 5};
% ThetaMean = dataArray{:, 6};
% ThetaDev = dataArray{:, 7};
% Height = dataArray{:, 8};
% Width = dataArray{:, 9};
% Area = dataArray{:, 10};
% Volume = dataArray{:, 11};

%   USE FOR OUR RH SYSTEM
Number = dataArray{:, 1};
Time = dataArray{:, 2};
ThetaL = dataArray{:, 3};
ThetaR = dataArray{:, 4};
ThetaMean = dataArray{:, 5};
ThetaDev = dataArray{:, 6};
Height = dataArray{:, 7};
Width = dataArray{:, 8};
Area = dataArray{:, 9};
Volume = dataArray{:, 10};

%% Clear temporary variables
clearvars filename delimiter startRow formatSpec fileID dataArray ans;
```

- Fluorescence Image Analysis Script -

```
%%  PETER DUNNING
%%%%%%%%%%%%%%%%%%%%%%%%%%%%%%%%%%%%%%%%%%%%%%%%%%%%%%%%%%%%%%%%%%%%%%%%%%%%
%%%%%%%%%%%%%%%%%%%%%%%%%%%%%%%%%%%%%%%%%%%%%%%%%%%%%%%%%%%%%%%%%%%%%%%%%%%%
%   Image analysis script for fluorescent images

clear all;
close all;
clc;
format compact;

%%%%%%%%%%%%%%%%%%%%%%%%%%%%%%%%%%%%%%%%%%%%%%%%%%%%%%%%%%%%%%%%%%%%%%%%%%%%
%%%%%%%%%%%%%%%%%%%%%%%%%%%%%%%%%%%%%%%%%%%%%%%%%%%%%%%%%%%%%%%%%%%%%%%%%%%%
%%  1   - CONSTANTS
thetadiv=100; % number of angular divisions
raddiv=100; % number of radial divisions
gainratio=1/1; % ratio of gains between images for plot comparison

%   FOLDER WHERE SUPERSATURATED DATA IS LOCATED
myFolder = 'DIRECTORY 1'; % EDIT THIS LINE
filePattern=fullfile(myFolder, '*.jpg');
jpgFiles=dir(filePattern);

%   FOLDER WHERE INTENSITY DATA IS LOCATED
myFolder1 = 'DIRECTORY 2'; % EDIT THIS LINE
filePattern1=fullfile(myFolder1, '*.jpg');
jpgFiles1=dir(filePattern1);

%   WHERE DO YOU WANT TO SAVE DATA
myFolder2 = 'DIRECTORY 3';

%%%%%%%%%%%%%%%%%%%%%%%%%%%%%%%%%%%%%%%%%%%%%%%%%%%%%%%%%%%%%%%%%%%%%%%%%%%%
%%%%%%%%%%%%%%%%%%%%%%%%%%%%%%%%%%%%%%%%%%%%%%%%%%%%%%%%%%%%%%%%%%%%%%%%%%%%
%%  2   - IMAGE ANALYSIS
for P=1:length(jpgFiles)
%%  2.1 - Image import / RGB - Grayscale - BW
    baseFileName =jpgFiles(P).name;
    fullFileName=fullfile(myFolder, baseFileName);
    fprintf(1, 'Now reading %s\n', fullFileName);
    RGB=imread(fullFileName); % SUPERSATURATED IMAGE FOR MASK
    I=rgb2gray(RGB); % convert RGB to grayscale

    baseFileName1 =jpgFiles1(P).name;
    fullFileName1=fullfile(myFolder1, baseFileName1);
    FileName1=baseFileName1(1:end-4);
    fprintf(1, 'Now reading %s\n', fullFileName1);
    % convert RGB to grayscale
    RGBF=imread(fullFileName1); % IMAGE
    IF=rgb2gray(RGBF);
    BW=graythresh(IF); %Otsu greyscale threshold

    BWI = im2bw(I,BW); %Creates BW Image from I using BW as graythresh
    [B,L] = bwboundaries(BWI,'noholes');
```

```
%%%%%%%%%%%%%%%%%%%%%%%%%%%%%%%%%%%%%%%%%%%%%%%%%%%%%%%%%%%%%%%%%%%%%%%%%%%%%%%
%%%%%%%%%%%%%%%%%%%%%%%%%%%%%%%%%%%%%%%%%%%%%%%%%%%%%%%%%%%%%%%%%%%%%%%%%%%%%%%
%%  2.2 - 3D Plot of Intensity
    figure (1)
    [xxx,yyy]=size(IF);
    XXX=1:xxx;
    YYY=1:yyy;
    [xx,yy]=meshgrid(YYY,XXX);
    ii=im2double(IF);
    figure (1);
    mesh(xx,yy,ii);
    colorbar
    saveas(gcf, fullfile(myFolder2,[FileName1 '_1.fig']) );
    set(gcf, 'Position', get(0,'Screensize'));
    saveas(gcf, fullfile(myFolder2,[FileName1 '_1.jpg']) )
    close (figure (1))

%%%%%%%%%%%%%%%%%%%%%%%%%%%%%%%%%%%%%%%%%%%%%%%%%%%%%%%%%%%%%%%%%%%%%%%%%%%%%%%
%%%%%%%%%%%%%%%%%%%%%%%%%%%%%%%%%%%%%%%%%%%%%%%%%%%%%%%%%%%%%%%%%%%%%%%%%%%%%%%
%%  2.3 - DEBUG
    % FOR DEBUG Plots all Boundaries in BWI
    %imshow(IF)
    %hold on
    %for k = 1:length(B)
    %    boundary = B{k};
    %    %plot(boundary(:,2), boundary(:,1), 'r', 'LineWidth', 2)
    %end

    % %Finds the Boundary with the largest span in 'x'
    % S_max = 0;
    % for k = 1:length(B)
    %      boundary = B{k};
    %      diff = max(boundary) - min(boundary);
    %      S = diff(1);
    %      if S(1) > S_max
    %          S_max=S(1);
    %          S_bound='null';
    %          S_bound=boundary;
    %          S_i=k; % index reflects which boundary is the largest
    %      end
    % end

    % If the largest span is the border of the image,
    % set the largest vector to null and run again.
    % B{S_i}='null';
%%%%%%%%%%%%%%%%%%%%%%%%%%%%%%%%%%%%%%%%%%%%%%%%%%%%%%%%%%%%%%%%%%%%%%%%%%%%%%%
%%%%%%%%%%%%%%%%%%%%%%%%%%%%%%%%%%%%%%%%%%%%%%%%%%%%%%%%%%%%%%%%%%%%%%%%%%%%%%%
%%  2.4 - Boundary & Center Point
    S_max = 0;
    S = 'null';
    for k = 1:length(B)
        boundary = B{k};
        diff = max(boundary) - min(boundary);
        S = diff(1);
        if S(1) > S_max
            S_max=S(1);
```

```
            S_bound='null';
            S_bound=boundary;
            S_Diam = diff;
            Cent = (max(boundary)+min(boundary))/2;
            S_i=k; % index reflects which boundary is the largest
        end
    end

    %Plots GS image and selected boundary
    figure (2)
    imshow(IF)
    hold on;
    plot(S_bound(:,2), S_bound(:,1), 'r', 'LineWidth', 2)
    hold on;
    plot(Cent(2),Cent(1),'o')
    saveas(gcf, fullfile(myFolder2,[FileName1 '_2.fig']) );
    set(gcf, 'Position', get(0,'Screensize'));
    saveas(gcf, fullfile(myFolder2,[FileName1 '_2.jpg']) )
    close (figure (2))
%%%%%%%%%%%%%%%%%%%%%%%%%%%%%%%%%%%%%%%%%%%%%%%%%%%%%%%%%%%%%%%%%%%%%%%%%%%%%%%
%%%%%%%%%%%%%%%%%%%%%%%%%%%%%%%%%%%%%%%%%%%%%%%%%%%%%%%%%%%%%%%%%%%%%%%%%%%%%%%
%%  2.5 - Mask & Stats
    % Creating a polygon of the selected boundary to create a mask
    yv = S_bound(:,1);
    xv = S_bound(:,2);
    I_S = size(I);
    Y = I_S(2);
    X = I_S(1);
    mask=poly2mask(xv,yv,X,Y); % creates mask from the polygon.

    % Find Stats within the Region of Interest
    STATS = regionprops(mask, IF, 'Area','MeanIntensity','Perimeter');
    [AAA,BBB]=max(vertcat(STATS.Area));
    stats = [cat(1, STATS(BBB).Area) cat(1, STATS(BBB).MeanIntensity)];

    % Create a ROI that is some percentage of the radius.
    r = mean(S_Diam)/2;
    NUM=raddiv; % number of radial divisions
    inc=1/NUM;
    i_stats = zeros (NUM+1,2);
    i_stats(1,:) = stats; % first row is area&intensity of full region

    % Creates masks for all segments of interest
    i_sum = zeros(X,Y);
    for j=1:NUM
        for i = 1:360
            x(i) = Cent(2) + (NUM-j) * r / NUM * cos( i /180 * 3.1415);
            y(i) = Cent(1) + (NUM-j) * r / NUM * sin( i /180 * 3.1415);
        end
        if j==1;
            i_mask{j} = mask - poly2mask(x,y,X,Y);
        elseif j < NUM
            i_mask{j} = mask - poly2mask(x,y,X,Y) - i_sum;
        else
            i_mask{j} = mask - i_sum;
        end
```

```
        i_mask{j}(i_mask{j}<0)=0; % sets negative values to zero

        STATS = regionprops(i_mask{j}, IF,'Area','MeanIntensity');
        i_sum = i_sum + i_mask{j};
        i_stats(NUM+2-j,:) = [cat(1, STATS(1).Area) cat(1, ...
        STATS(1).MeanIntensity)];
        y_plot(NUM+1-j,:) = i_stats(NUM+2-j,:);
    end
%%%%%%%%%%%%%%%%%%%%%%%%%%%%%%%%%%%%%%%%%%%%%%%%%%%%%%%%%%%%%%%%%%%%%%%%%%%%%%%
%%%%%%%%%%%%%%%%%%%%%%%%%%%%%%%%%%%%%%%%%%%%%%%%%%%%%%%%%%%%%%%%%%%%%%%%%%%%%%%
%%  2.6 - Annular Divisions / Angular Sectors / Annular Sectors
    figure (3) % Concentric annuli masks
    for i=1:raddiv
        subplot(2,3,i); imshow(i_mask{i})
    end
    saveas(gcf, fullfile(myFolder2,[FileName1 '_3.fig']) );
    set(gcf, 'Position', get(0,'Screensize'));
    saveas(gcf, fullfile(myFolder2,[FileName1 '_3.jpg']) )
    close (figure (3))

    % azimuthal breakdown
    n=thetadiv; % number of increments
    Theta=2*pi/n; % angular increment
    Rho=1.1*max(S_Diam)/2;

    % First calculate local average radii for each sector
    figure (4) % Azimuthal masks
    azi_radii=zeros(n,1); % initialize for sector radii
    for i=1:n
        rho2=linspace(0,Rho)';
        rho1=flipud(rho2);
        rho3=ones(300,1)*Rho;
        theta1=ones(length(rho1),1)*(i-1)*Theta;
        theta2=ones(length(rho1),1)*i*Theta;
        theta3=linspace((i-1)*Theta+2*pi,i*Theta,300)';
        rho=cat(1,rho1,rho2,rho3);
        theta=cat(1,theta1,theta2,theta3);
        xazi=rho.*cos(theta)+Cent(2);
        yazi=-rho.*sin(theta)+Cent(1);
        azi{i}=poly2mask(xazi,yazi,X,Y); % droplet area minus sectors
        aziprime{i}=mask-azi{i}; % sectors only
        aziprime{i}(aziprime{i}<0)=0; % sets negative values to zero
        subplot(4,5,i); imshow(aziprime{i}) % show different sectors
        azimuthal(i)=radtodeg(i*Theta-Theta/2); % center of each sector
        STATS=regionprops(aziprime{i}, IF,'Area'); % area of sector
        azi_radii(i)=cat(1, STATS(1).Area);
        azi_radii(i)=sqrt(azi_radii(i)*2/Theta); % average radius
    end
    saveas(gcf, fullfile(myFolder2,[FileName1 '_4.fig']) );
    set(gcf, 'Position', get(0,'Screensize'));
    saveas(gcf, fullfile(myFolder2,[FileName1 '_4.jpg']) )
    close (figure (4))

    % Then calculate intensity in each annular sector
    figure (5) % Annular sector masks
    azirad_intens=ones(NUM,n)*NaN; % initialize for annular sector
```

```
for i=1:n % angular position
    rinc=azi_radii(i)/NUM; % radial segments of each annular sector
    theta1=ones(50,1)*(i-1)*Theta;
    theta2=linspace((i-1)*Theta,i*Theta,50)';
    theta3=ones(length(theta1),1)*i*Theta;
    theta4=flipud(theta2);
    theta=cat(1,theta1,theta2,theta3,theta4);
    for j=1:NUM % radial position
        rho1=linspace((j-1)*rinc,j*rinc,50)';
        rho2=ones(length(rho1),1)*rinc*j;
        rho3=flipud(rho1);
        rho4=ones(length(rho1),1)*rinc*(j-1);
        rho=cat(1,rho1,rho2,rho3,rho4);
        xazi=rho.*cos(theta)+Cent(2);
        yazi=-rho.*sin(theta)+Cent(1);
        azi2{1}=poly2mask(xazi,yazi,X,Y);
        % droplet area minus sectors
        subplot(NUM,n,j+n*(i-1)); imshow(azi2{1})
        % show different annular sectors

        if max(azi2{1})==0 % skips error for empty annular sectors
            azirad_intens(j,i)=NaN;
        else
            STATS=regionprops(azi2{1}, IF,'MeanIntensity');
            % intensity of each annular sector
            azirad_intens(j,i)=cat(1, STATS(1).MeanIntensity);
        end
    end
end
saveas(gcf, fullfile(myFolder2,[FileName1 '_5.fig']) );
set(gcf, 'Position', get(0,'Screensize'));
saveas(gcf, fullfile(myFolder2,[FileName1 '_5.jpg']) )
close (figure (5))

azirad_intens_stats=zeros(NUM,1);
for j=1:NUM
    x_plot(j)=100*(j*inc-inc/2);
    % midline radius percentage of each annulus
    azirad_intens_stats(j,1)=nanmean(azirad_intens(j,:));
    azirad_intens_stats(j,2)=nanstd(azirad_intens(j,:));
end

azi_intens=zeros(n,NUM);
% initialize for annular sector intensities
for j=1:NUM
    for k=1:n
        azirad{1}=i_mask{j}-azi{k};
        azirad{1}(azirad{1}<0)=0; % sets negative values to zero
        if max(azirad{1})==0 % skips error for empty annular sector
            azi_intens(k,j)=0;
        else
        STATS = regionprops(azirad{1}, IF,'MeanIntensity');
        azi_intens(k,j)=cat(1, STATS(1).MeanIntensity);
        end
    end
end
```

```
%%%%%%%%%%%%%%%%%%%%%%%%%%%%%%%%%%%%%%%%%%%%%%%%%%%%%%%%%%%%%%%%%%%%%%%%%%%%
%%%%%%%%%%%%%%%%%%%%%%%%%%%%%%%%%%%%%%%%%%%%%%%%%%%%%%%%%%%%%%%%%%%%%%%%%%%%
%%  2.7 - Intensity Plots
%   Plot radial position vs. intensity
    FS = 20; MS = 12;
    figure (6) % Intensity vs. radial position
    axes('FontSize',FS-5);
    hold on
    plot(x_plot, y_plot(:,2),'ok','MarkerSize',MS);
    plot([0 100], [i_stats(1,2) i_stats(1,2)],'-k'); % Mean intensity
    xlabel('Radial Position (%)', 'FontSize',FS);
    ylabel('Avg. Image Intensity (bit)', 'FontSize',FS);
    grid on
    saveas(gcf, fullfile(myFolder2,[FileName1 '_6.fig']) );
    set(gcf, 'Position', get(0,'Screensize'));
    saveas(gcf, fullfile(myFolder2,[FileName1 '_6.jpg']) )
    close (figure (6))

    figure (7) % Dimensionless intensity vs. radial position
    axes('FontSize',FS-5);
    hold on
    plot(x_plot,
y_plot(:,2)/i_stats(1,2)*gainratio,'ok','MarkerSize',MS);
    xlabel('Radial Position (%)', 'FontSize',15);
    ylabel('Dimensionless Image Intensity (-)', 'FontSize',FS);
    grid on
    saveas(gcf, fullfile(myFolder2,[FileName1 '_7.fig']) );
    set(gcf, 'Position', get(0,'Screensize'));
    saveas(gcf, fullfile(myFolder2,[FileName1 '_7.jpg']) )
    close (figure (7))

    figure (8) % Intensity vs. radial position by azimuthal position
    axes('FontSize',FS-5);
    plot([0 100], [i_stats(1,2) i_stats(1,2)],'-k'); % Mean intensity
    xlabel('Radial Position (%)', 'FontSize',FS);
    ylabel('Avg. Image Intensity (bit)', 'FontSize',FS);
    grid on
    hold on
    for i=1:n % Removes leading zeros due to empty annular sectors
        azione=azi_intens(i,:);
        ind1=find(azione,1);
        ind2=length(azione);
        plot(fliplr(x_plot(ind1:ind2)),
azione(ind1:ind2),'MarkerSize',MS);
    end
    legend ('1','2','3','4','5','6','7','Location','NorthWest'
    saveas(gcf, fullfile(myFolder2,[FileName1 '_8.fig']) );
    set(gcf, 'Position', get(0,'Screensize'));
    saveas(gcf, fullfile(myFolder2,[FileName1 '_8.jpg']) )
    close (figure (8))

    figure (9) % Dimensionless intensity vs. radial position by azimuth
    axes('FontSize',FS-5);
    xlabel('Radial Position (%)', 'FontSize',FS);
    ylabel('Avg. Image Intensity (bit)', 'FontSize',FS);
    grid on
```

```
hold on
for i=1:n % removes leading zeros due to empty annular sectors
    azione=azi_intens(i,:);
    ind1=find(azione,1);
    ind2=length(azione);
    plot(fliplr(x_plot(ind1:ind2)), ...
        azione(ind1:ind2)/i_stats(1,2),'MarkerSize',MS);
end
legend ('1','2','3','4','5','6','7','Location','NorthWest')
saveas(gcf, fullfile(myFolder2,[FileName1 '_9.fig']) );
set(gcf, 'Position', get(0,'Screensize'));
saveas(gcf, fullfile(myFolder2,[FileName1 '_9.jpg']) )
close (figure (9))

% Azimuthally averaged plots
azirad_intens_stats(:,3) = azirad_intens_stats(:,1) + ...
    azirad_intens_stats(:,2)*3; % +3 std. dev.
azirad_intens_stats(:,4) = azirad_intens_stats(:,1) - ...
    azirad_intens_stats(:,2)*3; % -3 std. dev.
azirad_intens_stats(:,5) = azirad_intens_stats(:,1) + ...
    azirad_intens_stats(:,2)*2; % +2 std. dev.
azirad_intens_stats(:,6) = azirad_intens_stats(:,1) - ...
    azirad_intens_stats(:,2)*2; % -2 std. dev.
azirad_intens_stats(:,7) = azirad_intens_stats(:,1) + ...
    azirad_intens_stats(:,2)*1; % +1 std. dev.
azirad_intens_stats(:,8) = azirad_intens_stats(:,1) - ...
    azirad_intens_stats(:,2)*1; % -1 std. dev.

figure (10) % Intensity vs. radial position
axes('FontSize',FS-5);
plot([0 100], [i_stats(1,2) i_stats(1,2)],'-k'); % Mean intensity
xlabel('Radial Position (%)', 'FontSize',FS);
ylabel('Avg. Image Intensity (bit)', 'FontSize',FS);
grid on
hold on
plot(x_plot,azirad_intens_stats(:,1),'k-','MarkerSize',MS)
plot(x_plot,azirad_intens_stats(:,3),'r--','MarkerSize',MS)
plot(x_plot,azirad_intens_stats(:,4),'r--','MarkerSize',MS)
plot(x_plot,azirad_intens_stats(:,5),'b--','MarkerSize',MS)
plot(x_plot,azirad_intens_stats(:,6),'b--','MarkerSize',MS)
plot(x_plot,azirad_intens_stats(:,7),'g--','MarkerSize',MS)
plot(x_plot,azirad_intens_stats(:,8),'g--','MarkerSize',MS)
saveas(gcf, fullfile(myFolder2,[FileName1 '_10.fig']) );
set(gcf, 'Position', get(0,'Screensize'));
saveas(gcf, fullfile(myFolder2,[FileName1 '_10.jpg']) )
close (figure (10))

FS      =   24;
MS      =   30;

figure (11) % Dimensionless intensity vs. radial position
axes('FontSize',FS-5);
xlabel('Radial Position (%)', 'FontSize',FS);
ylabel('Avg. Dimensionless Image Intensity', 'FontSize',FS);
grid on
hold on
```

```
    plot(x_plot,azirad_intens_stats(:,1)/i_stats(1,2), ...
        'k-','MarkerSize',MS)
    plot(x_plot,azirad_intens_stats(:,3)/i_stats(1,2), ...
        'r--','MarkerSize',MS)
    plot(x_plot,azirad_intens_stats(:,4)/i_stats(1,2), ...
        'r--','MarkerSize',MS)
    plot(x_plot,azirad_intens_stats(:,5)/i_stats(1,2), ...
        'b--','MarkerSize',MS)
    plot(x_plot,azirad_intens_stats(:,6)/i_stats(1,2), ...
        'b--','MarkerSize',MS)
    plot(x_plot,azirad_intens_stats(:,7)/i_stats(1,2), ...
        'g--','MarkerSize',MS)
    plot(x_plot,azirad_intens_stats(:,8)/i_stats(1,2), ...
        'g--','MarkerSize',MS)
    saveas(gcf, fullfile(myFolder2,[FileName1 '_11.fig']) )
    set(gcf, 'Position', get(0,'Screensize'));
    saveas(gcf, fullfile(myFolder2,[FileName1 '_11.jpg']) )
    close (figure (11))
%%%%%%%%%%%%%%%%%%%%%%%%%%%%%%%%%%%%%%%%%%%%%%%%%%%%%%%%%%%%%%%%%%%%%%%%%%%%%%%
%%%%%%%%%%%%%%%%%%%%%%%%%%%%%%%%%%%%%%%%%%%%%%%%%%%%%%%%%%%%%%%%%%%%%%%%%%%%%%%
%%  2.8 - Intensity Data

%   RADIUS DATA
    Area(:,P)=i_stats(1,1);
        %   Area of mask
    A_Rad(:,P)=sqrt(i_stats(1,1)/pi());
        %   Radius of mask based on area of mask
        Mean_Rad=mean(A_Rad); %Mean of Radius
        Std_Rad=std(A_Rad);   %Std Dev of Radius
        Rad(:,P)=azi_radii;
        %   Radius for each annular section for an Image
        %   Iterated for each image
        %   Plot each ith column (Average radius for one image for each
        %   annular section) vs annular sections

%   INTENSITY DATA
    Int(:,P)=azirad_intens_stats(:,1); % plot vs. x_plot
        %   Non-Normalized Intensity of Each Plot
        %   Iterated for each image
        %   Plot each ith column (Normalized intensity for one image)
        %   vs x_plot (Radial Positions)
    Avg_Int(:,P)=i_stats(1,2);
        %   Average Intensity of each Image
        %   Iterated for each image
    Int_N(:,P)=azirad_intens_stats(:,1)/i_stats(1,2); % plot vs. x_plot
        %   Normalized Intensity of Each Plot by Intensity of Image
        %   Iterated for each image
        %   Plot each ith column (Normalized intensity for one image)
        %   vs x_plot (Radial Positions)
end
%%%%%%%%%%%%%%%%%%%%%%%%%%%%%%%%%%%%%%%%%%%%%%%%%%%%%%%%%%%%%%%%%%%%%%%%%%%%%%%
%%%%%%%%%%%%%%%%%%%%%%%%%%%%%%%%%%%%%%%%%%%%%%%%%%%%%%%%%%%%%%%%%%%%%%%%%%%%%%%
%%  3 - Data Export
OUT1=Rad;               % RADIUS OF ANNULAR SECTION (VS RADIAL POSITION)
OUT2=Int;               % INTENSITY (VS RADIAL POSITIONS)
OUT3=Int_N;             % NORMALIZED INTENSITY (VS RADIAL POSITIONS)
```

```
OUT4=transpose(A_Rad);  % RADIUS OF MASK
OUT5=transpose(Avg_Int);% AVERAGE INTENSITY
OUT6=thetadiv;          % NUMBER OF ANGULAR DIVISIONS
OUT7=raddiv;            % NUMBER OF RADIAL DIVISIONS

dlmwrite(fullfile(myFolder2,'O1_RAD.txt'),          OUT1,       '\t');
dlmwrite(fullfile(myFolder2,'O2_INT.txt'),          OUT2,       '\t');
dlmwrite(fullfile(myFolder2,'O3_INT_N.txt'),        OUT3,       '\t');
dlmwrite(fullfile(myFolder2,'O4_A_RAD.txt'),        OUT4,       '\t');
dlmwrite(fullfile(myFolder2,'O5_A_INT.txt'),        OUT5,       '\t');
dlmwrite(fullfile(myFolder2,'O6_THETA_DIV.txt'),    OUT6,       '\t');
dlmwrite(fullfile(myFolder2,'O7_RAD_DIV.txt'),      OUT7,       '\t');
%%%%%%%%%%%%%%%%%%%%%%%%%%%%%%%%%%%%%%%%%%%%%%%%%%%%%%%%%%%%%%%%%%%%%%%
%%%%%%%%%%%%%%%%%%%%%%%%%%%%%%%%%%%%%%%%%%%%%%%%%%%%%%%%%%%%%%%%%%%%%%%
```

- Modified Young - Lippmann Equation for Coplanar Electrodes Script-

```
clc; close all;

% Read images
Drop=imread('Matlab Capacitance - Droplet 80-40.bmp');
Drop2=imread('Matlab Capacitance - Droplet2 80-40.bmp');
Right=imread('Matlab Capacitance - Right 80-40.bmp');
Left=imread('Matlab Capacitance - Left 80-40.bmp');
Border=imread('Matlab Capacitance - Border 80-40.bmp');

% Delete extra row and column
Drop(4021,:)=[]; Drop(:,4001)=[];
Drop2(4021,:)=[]; Drop2(:,4001)=[];
Right(4021,:)=[]; Right(:,4001)=[];
Left(4021,:)=[]; % Left(:,4001)=[];
Border(4021,:)=[]; Border(:,4001)=[];

% Calculate electrode overlap
A=(Drop+Left-2*Border)-1; A(A<0)=0; areaA=sum(sum(A))*10^-12; % m^2
B=(Drop+Left-2*Border)-1; B(B<0)=0; areaB=sum(sum(B))*10^-12; % m^2
A2=(Drop2+Left-2*Border)-1; A2(A2<0)=0; areaA2=sum(sum(A2))*10^-12;
% m^2
B2=(Drop2+Left-2*Border)-1; B2(B2<0)=0; areaB2=sum(sum(B2))*10^-12;
% m^2

% Calculate interdigitated capacitance
e0=8.854*10^-12; % F/m, fundamental constant
ed=3.28; % dielectric constant of SU8
d=3.6*10^-6; % m, thickness of SU8
C=e0*ed*areaA*areaB/d/(areaA+areaB); % F
C2=e0*ed*areaA2*areaB2/d/(areaA2+areaB2); % F
D1=1.6*10^-3; % m, diameter of IDE droplet
areaD=pi*D1^2/4; % m^2, contact area of droplet
Cdigit=C/areaD; % F/m^2, droplet centered between electrodes
Cdigit2=C2/areaD; % F/m^2, droplet centered on an electrode
Cdigitavg=(Cdigit+Cdigit2)/2; % F/m^2, average of two IDE cases
Csimple=e0*ed/d; % F/m^2, simple calculation initially used

% Calculate "hamburger" capacitance
w=80*10^-6; % m, width of electrode
s=40*10^-6; % m, spacing between electrodes
D2=1.6*10^-3; % m, diameter of hamburger droplet
areaH=pi*D2^2/4; % m^2, contact area of droplet
A3=pi*D2^2/4-D2*(w+2*s); % m^2, area of circular electrode
A4=w*D2; % m^2, area of rectangular electrode
% A3=pi*D2^2/4-.001146*(w+2*s)-w*s; % m^2, area of circular electrode
% A4=w*.001146+.05*10^-3*w; % m^2, area of rectangular electrode
Cburger=e0*ed*A3*A4/d/(A3+A4)/areaH; % F/m^2

% Apply the BLY equation
gammaLG=.072; % N/m, surface tension of water at 25C
theta0=88.68; % resting CA for water on SU8
Vrms=(0:1:500)'; % applied voltages up to 500 V
```

```
figure (1) % Theoretical
grid on; hold on;
set(gca,'FontSize',28)
theta(:,2)=acosd(cosd(theta0)+Csimple*Vrms.^2/2/gammaLG);
plot(Vrms,real(theta(:,2)),'k') % inserted ground wire
theta(:,1)=acosd(cosd(theta0)+Cdigitavg*Vrms.^2/2/gammaLG);
plot(Vrms,real(theta(:,1)),'r') % interdigitated electrodes
theta(:,3)=acosd(cosd(theta0)+Cburger*Vrms.^2/2/gammaLG);
plot(Vrms,real(theta(:,3)),'g') % hamburger electrodes
legend ('Inserted Ground Wire','Coplanar IDE', ...
    'Simple Coplanar Electrode','Location','SouthWest')
set(findobj(gca,'type','line'),'LineWidth', 5);
axis([0 500 20 100])

% After running, copy the Excel data into the test variable
% and then copy from "then" until "end" into the command window

% test=0;
if test==1
    then

    % IDE
    hold on
    plot(test(:,8),test(:,7),'ro')

    % Hamburger
    hold on
    plot(test(:,6),test(:,5),'go')

    % Inserted Wire
    hold on
    plot(test1(:,4),test1(:,3),'bo')
    %plot(test(:,2),test(:,1),'c>')

end
```